Combining Multitemporal Microwave and Optical Remote Sensing Data

-

Mapping of Land Use / Land Cover, Crop Type, and Crop Traits

Inaugural-Dissertation

zur

Erlangung des Doktorgrades

der Mathematisch-Naturwissenschaftlichen Fakultät

der Universität zu Köln

vorgelegt von

Christoph Hütt

aus Ludwigshafen

Köln

2019

Berichterstatter: **Prof. Dr. Georg Bareth**

Prof. Dr. Karl Schneider

Tag der letzten mündlichen Prüfung: 8. Mai 2019

Abstract

Humanity has changed the earth's surface to a dramatic extent. This is especially true for the area used for agricultural production. Against the background of a growing world population and the associated increased demand for food, it is precisely this area that will become even more important in the future. In order not to have to allocate even more land to agricultural use, optimization and intensification is the only way out of the dilemma. In this context, precise Geoinformation of the agriculturally used area is of central importance. It is utilized for improving land use, producing yield forecasts for more stable food security, and optimizing agricultural management. Rapid developments in the field of satellite-based remote sensing sensors make it possible to monitor agricultural areas with increased spatial, spectral and temporal resolution. However, to retrieve the needed information from this data, new methods are needed. Furthermore, the quality of the data has to be verified. Only then can the presented geodata help to grow crops more sustainably and more efficiently.

This thesis develops new approaches for monitoring agricultural areas using the technology of microwave remote sensing in combination with optical remote sensing and existing geodata. It is framed by the overall objective to obtain knowledge on how this combination of data can provide the necessary geoinformation for land use studies, precision farming, and agricultural monitoring systems. Hundreds of remote sensing images from more than eight different satellites were analyzed in six research studies from two different Areas of Interest (AOIs). The studies guide through various spatial scales. First, the general Land Use / Land Cover (LULC) on a regional level in a multi-sensor scenario is derived, evaluating different sensor combinations of varying

resolutions. Next, an innovative method is proposed, through which the high geometric accuracy of radar-imaging satellite sensors is exploited to update the spatial accuracy of any external geodata of lower spatial accuracy. Such external data is then used in the next two studies, which focus on cost-effective crop type mapping using Synthetic Aperture Radar (SAR) images. The resulting enhanced LULC maps present the annually changing crop types of the region alongside external, official geoinformation that is not retrievable from remote sensing sensors. The last two research studies deal with a single maize field, on which high resolution optical WorldView-2 images and experimental bistatic SAR observations from TanDEM-X are assessed and combined with ground measurements.

As a result, this thesis shows that, depending on the AOI and the application, different resolution demands need to be fulfilled before LULC, crop type, and crop traits mapping can be performed with adequate accuracy. The spatial resolution needs to be adapted to the particularities of the AOI. Evaluation of the sensors showed that SAR sensors proved beneficial for the study objective. Processing the SAR images is complicated, and the images are unintuitive at first sight. However, the advantage of SAR sensors is that they work even in cloudy conditions. This results in an increased temporal resolution, which is particularly important for monitoring the highly dynamic agricultural area. Furthermore, the high geometric accuracy of the SAR images proved ideal for implementing the Multi-Data Approach (MDA). Thus information-rich external geodata could be used to lower the remote sensing resolution needs, improve the accuracy of the LULC-maps, and to provide enhanced LULC-maps. The first study of the maize field demonstrates the potential of the WorldView-2 data in predicting in-field biomass variations, and its increased accuracy when fused with plant height measurements. The second study shows the potential of the TanDEM-X Constellation (TDM) to retrieve plant height from space.

LULC, crop type and information on the spatial distribution of biomass can thus be derived efficiently and with high accuracy from the combination of SAR, optical satellites and external geodata. The

shown analyses for acquiring such geoinformation represent a high potential for helping to solve the future challenges of agricultural production.

Zusammenfassung

Die Menschheit hat die Erdoberfläche in dramatischem Maße verändert. Dies gilt insbesondere für die durch landwirtschaftliche Produktion genutzte Fläche. Vor dem Hintergrund einer wachsenden Weltbevölkerung und dem damit verbundenen erhöhten Bedarf nach Nahrungsmitteln werden gerade diese Gebiete in Zukunft weiter an Bedeutung zunehmen. Um nicht noch mehr Flächen für die landwirtschaftliche Nutzung bereitstellen zu müssen, ist Optimierung und Intensivierung der einzige Ausweg aus dem Dilemma. Von zentraler Bedeutung sind dabei Geoinformationen der landwirtschaftlich genutzten Fläche. Sie werden eingesetzt zur Verbesserung der Landnutzung, zur Erstellung von Ertragsprognosen für eine stabilere Ernährungssicherheit und zur Optimierung des Agrarmanagements. Rasante Entwicklungen auf dem Gebiet der satellitengestützten Fernerkundungssensoren ermöglichen es, landwirtschaftliche Flächen mit erhöhter spektraler, räumlicher und zeitlicher Auflösung abzubilden. Um jedoch die benötigten Informationen aus den Daten zu gewinnen, bedarf es neuer Methoden. Zusätzlich muss die Qualität der Daten verifiziert werden, nur dann können die präsentierten Geodaten dazu beitragen, den Nutzpflanzenanbau nachhaltiger und effizienter zu gestalten.

In dieser Arbeit werden neue Ansätze für die Beobachtung landwirtschaftlicher Flächen entwickelt. Dazu wird die Technologie der satellitengestützten Synthetic Aperture Radar (SAR) Mikrowellenfernerkundung mit optischer Satelittenfernerkundung und bestehenden Geodaten kombiniert. Das übergeordnete Ziel der Arbeit ist es, Erkenntnisse darüber zu gewinnen, wie diese Datenkombination die notwendigen Geoinformationen für Landnutzungsstudien, Präzisionslandwirtschaft und landwirtschaftliche Überwachungssysteme liefern

kann. Hunderte Fernerkundungsbilder von mehr als acht unterschiedlichen Satellitensystemen wurden in sechs Forschungsstudien aus zwei verschiedenen Untersuchungsgebieten analysiert. Die Studien leiten durch die verschiedenen berücksichtigten räumlichen Skalen. Zu Beginn wird die allgemeine Landnutzung auf regionaler Ebene in einem Multisensor-Szenario abgeleitet, dabei werden verschiedene Sensorkombinationen mit unterschiedlichen Auflösungen bewertet. Als nächstes wird ein innovatives Verfahren vorgestellt, durch das die hohe geometrische Genauigkeit der SAR-Satelliten genutzt wird, um die räumliche Lagegenauigkeit externer Geodaten mit geringerer Genauigkeit zu verbessern. Solche externen Geodaten sind ein Fokus der nächsten beiden Studien, die kosteneffiziente Feldfruchtkartierung mithilfe von SAR-Bildern demonstrieren. Die daraus resultierenden verbesserten Landnutzungskarten zeigen die jährlich wechselnden Feldfrüchte der Region in Kombination mit externen, offiziellen Geoinformationen, die normalerweise nicht von Fernerkundungssensoren ermittelt werden können. Die letzten beiden Forschungsarbeiten befassen sich mit einem Maisfeld, auf dem hochauflösende optische WorldView-2-Bilder und experimentelle bistatische SAR Beobachtungen von TanDEM-X, mit Bodenmessungen bewertet und kombiniert werden.

Die Ergebnisse der Arbeit zeigen, dass je nach Untersuchungsgebiet unterschiedliche Auflösungsanforderungen erfüllt sein müssen, bevor Landnutzung, Feldfrüchte und Pflanzeneigenschaften mit ausreichender Genauigkeit kartiert werden können. Es zeigte sich, dass die räumliche Auflösung an die Besonderheiten der Untersuchungsregion angepasst werden muss. In einer weiteren Sensorbewertung erwiesen sich die eingesetzten SAR Sensoren als vorteilhaft für das Studienziel. Obwohl die Bearbeitung der SAR Bilder kompliziert ist, und die Bilder auf den ersten Blick ungewohnt wirken, wurde der Vorteil der SAR Sensoren deutlich: auch bei bewölktem Himmel werden Daten geliefert. Diese Eigenschaft führt zu einer erhöhten zeitlichen Auflösung, die sich als essentiell für die Überwachung der hochdynamischen landwirtschaftlichen Flächen herausstellte. Darüber hinaus erwies sich die hohe geometrische Genauigkeit der SAR Bilder als ideal für die Implementierung des Multi-Data Approach (MDA).

Somit konnten informationsreiche externe Geodaten verwendet werden, um die Auflösungsanforderungen an die Fernerkundungsdaten zu senken, die Genauigkeit der Landnutzungskarten zu verbessern und um verbesserte, mit externen Geoinformationen angereicherte Landnutzungskarten zu erstellen. Die erste der beiden Maisfeldstudien zeigte das Potenzial des optischen Satellitensystems WorldView-2 für die Detektion von Biomassevariationen innerhalb eines Feldes und eine erhöhte Genauigkeit der Biomasseschätzung bei der Hinzunahme von Pflanzenhöhenmessungen. Die zweite Maisfeldstudie demonstrierte das Potenzial der TanDEM-X Konstellation, die Pflanzenhöhe auch aus dem Weltraum zu messen.

Landnutzung, Feldfruchtkartierungen und Informationen über die räumliche Verteilung von Biomasse lassen sich also aus der Kombination von SAR und optischen Satelliten und externen Geodaten effizient und mit hoher Genauigkeit ableiten. Die gezeigten Analysen zur Gewinnung der Geoinformation stellen ein großes Potential dar und können helfen, die zukünftigen Herausforderungen landwirtschaftlicher Produktion zu meistern.

Acknowledgements

I owe my sincere gratitude to Prof. Dr. Bareth, who supervised this dissertation. He introduced me to the wonderful field of remote sensing & GIS, and made this dissertation possible. His inspiring thoughts and ideas, and his ability to understand, sort, and promote my ideas were second to none. Thank you!

I also want to thank Prof. Dr. Karl Schneider for acting as second supervisor of this dissertation. Furthermore, I want to thank him for many fruitful discussions, thoughts, and support.

I am most grateful to all the members of the working group GIS & Remote Sensing, in particular, Dr. Andreas Bolten, Dr. Nora Tilly, Sebastian Brocks, and Dr. Guido Waldhoff. It was and is a pleasure working with you. I want to thank Thomas Busche from DLR TanDEM-X science team, for the great support during the TanDEM-X acquisition planning.

Thanks also go to the various anonymous peer reviewers for their open, and motivating comments.

Finally, my daughter Emilia, my son Anton, and of course my wife Nina mean everything to me. This work is dedicated to you.

Contents

List of Figures

List of Tables

Abbreviations

AOI	Area of Interest ... 10
ALKIS	German Authoritative Real Estate Cadastre Information System ... 125
ATKIS	German Authoritative Topographic-Cartographic Information System ... 21
AW	Acquisition Window ... 87
CSM	Crop Surface Model ... 146
DEM	Digital Elevation Model ... 12
DLM	Digital Landscape Model ... 91
DLR	German Aerospace Center ... 167
DTM	Digital Terrain Model ... 164
EU	European Union ... 19
ESA	European Space Agency ... 36
FOSS	Free and Open-Source Software ... 118
GCP	Ground Control Point ... 60
GIS	Geographic Information System ... 12
GPS	Global Positioning System ... 152
GRD	Ground Range Detected ... 123
HRWS	High Resolution Wide Swath ... 18
ICASD	International Center for Agro-Informatics and Sustainable Development ... 24
LULC	Land Use / Land Cover ... 1

LULCC	Land Use / Land Cover Change 1
LPIS	Land Parcel Identification System 21
MDA	Multi-Data Approach 19
NEST	Next ESA SAR Toolbox 36
NRW	North Rhine-Westphalia 27
NDVI	Normalized Difference Vegetation Index 146
NNI	Nitrogen Nutrition Index 147
OA	Overall Accuracy 33
PB	Physical Blocks 86
RF	Random Forest 18
SAR	Synthetic Aperture Radar 4
SNAP	Sentinel Application Toolbox 118
SI	Sustainable Intensification 1
SRTM	Shuttle Radar Topography Mission 13
TDM	TanDEM-X Constellation 8
TLS	Terrestrial Laser Scanning 8
TR32	Transregional Collaborative Research Centre 32 24
USGS	United States Geological Survey 10

1 Introduction

After almost a decade of declining world hunger, the number of undernourished people has been on the rise since 2014, reaching an estimated 821 million in 2017 (FAO et al. 2017). Additionally, more and wealthier people on planet earth are demanding more food and a more resource-intensive diet such as dairy products and meat (Godfray et al. 2018). This chapter provides an introduction into the challenges associated with agricultural production, Land Use / Land Cover Change (LULCC), discusses the need for Sustainable Intensification (SI) in agriculture, and identifies the role of remote sensing for LULCC, precision agriculture, and agricultural monitoring systems. Based on the data needs of those sectors, the overall objective of the study and the research questions are presented. Furthermore, an outline guides through the thesis.

1.1 Preface

There is immense pressure on global agricultural production to provide sufficient food (Tilman et al. 2002). Agriculture already is and will be threatened further by the implications of climate change (Wiebe et al. 2015) and the scarcity of land (Lambin & Meyfroidt 2011), the latter indicating the strong link of agricultural production to Land Use / Land Cover (LULC) and LULCC. Global agriculture is responsible for significant environmental issues as it directly accounts for 14 % of global greenhouse gas emissions (IPCC 2014: 88), 70 % of global freshwater usage (Rost et al. 2008), soil degradation (Parr et al. 1992), and altering the global nitrogen cycle with many global negative impacts (Vitousek et al. 1997). The latter being connected

to the release of heavy metals into the environment, pesticides, and fungicide abuse.

Not included in the statistics mentioned above is an indirect consequence that more land has been attributed to agricultural production over the last decades (Alexander et al. 2015). This increase is alarming as the global LULCC is the second highest contributor to the rising CO_2-concentration levels in the atmosphere, after the combustion of fossil fuels. Furthermore, current LULCC intensifies the conflict over land (Lambin & Meyfroidt 2011), leaving less space for nature (Tilman et al. 2002).

Rockström et al. (2017) claim for a SI in agriculture (Garnett et al. 2013), which aims to achieve future food security and solve the environmental issues of agriculture. SI is a complex challenge that can only be solved by a multitude of objectives and actions (McCarthy et al. 2018). One favorable principle is land sparing, which means increasing production through higher yields on already farmed land. The alternative way of increasing production by using new land for farming would worsen the environmental impacts (Phalan et al. 2011).

Solving such social and environmental problems is strongly connected to land change science, which tackles environmental and societal problems by understanding the dynamics of LULC as a coupled human-environment system (Turner et al. 2007). The initial crucial step to performing any land change science is observation and monitoring (Turner et al. 2007). However, global LULC- and LULCC-maps of adequate resolution in high quality are not available (Prestele et al. 2016), yet urgently needed, especially in the context of global food production (See et al. 2015).

Precision agriculture suits the described aims of SI, being described as an information technology used to improve production management and minimize environmental impacts (Whelan & Taylor 2013: 1). This technology helps to fulfill SI by higher yields per area and also improves the environmental quality (Gebbers & Adamchuk 2010). Most commonly, and especially when considering cropping systems, the term precision agriculture is used synonymously for site-specific

crop management (Whelan & Taylor 2013: 2). That term, however, refers more specifically to adopting the agronomic practices to the specific resource needs depending on the location. Those needs vary considerably not only from one field to another but also within fields. Hence, through knowledge about the growing conditions at each location within the field, farming machines can apply site-specific management, such as fertilizer applications (Carr et al. 1991) or plant protection actions (Mahlein et al. 2012).

In addition to precision agriculture techniques, agricultural monitoring systems provide information about food production (Fritz et al. 2018). Such systems allow forecasting of commodity prices enabling preparation for food-market variations. Risks in the food supply chain can thereby be identified, resulting in greater food security (Wu et al. 2014).

Land change science, precision farming and agricultural monitoring Systems depend on the quality and availability of the input data to provide reliable results (Jones et al. 2017). Furthermore, Jones et al. (2017) conclude that the limitations of current systems are due to a lack of available and usable data. The most prominent tool to acquire the needed data is remote sensing (Zhang et al. 2002; Pinter Jr et al. 2003). It can provide information about the environment, LULC, crop type, and the status of crops (Vinciková et al. 2010), which could not be generated with other methods because traditional methods, such as field surveys, are too time-consuming and expensive (Xie et al. 2008). Summaries of applications of remote sensing can be found in McNairn & Shang (2016) for crop tpe mapping, in Atzberger (2013) for agricultural monitoring systems, and in Mulla (2013) for precision farming.

The ongoing development of optical and especially of radar remote sensing systems have created new potentials for dealing with the future challenges described above. The development of new sensors mainly provides increased resolution over larger areas. Advanced information processing is, however, needed to fully exploit the potential of such systems (Benediktsson et al. 2012).

One such actively researched remote sensing sensor category consists

of radar or microwave remote sensors. They have the advantage of providing images even at night, and can penetrate through clouds (Curlander & McDonough 1991a). Surprisingly, Whelan & Taylor (2013) and Atzberger (2013) omit Synthetic Aperture Radar (SAR) remote sensing for precision farming and agricultural monitoring, respectively. Furthermore, as shown by Fritz et al. (2018), only three out the eight most important global agricultural monitoring systems use active radar data. The reasons for that lack of tapping the full potential of SAR could lie in the complexity of the radar signal, limited radar sensor capabilities (Schmullius et al. 2015), and limited knowledge of how microwaves interact with surfaces (Woodhouse 2015: 28).

1.2 Overall Objective and Research Questions

This study is based on the need for high-quality, frequently updated LULC maps, including information about crop type, and on a general lack of available and usable geoinformation about agricultural production. Furthermore, it is framed by the opportunities of sensor developments, especially in the domain of microwave remote sensing, where case studies are urgently needed to demonstrate and evaluate the potential of the technology. Hence, this research's objective is to obtain knowledge on how the combination of radar remote sensing, optical remote sensing, and other geodata can provide such necessary geoinformation for land use studies, precision farming, and agricultural monitoring systems.

This overall objective is subdivided into the following smaller objectives, which are sorted according to the principle of increasing temporal and spatial resolution. Furthermore, the second and third objectives presuppose the objectives one and two, respectively. All objectives are under the assumption of using satellite remote sensing data.

1. Determining of LULC in agricultural landscapes.
2. Mapping crop types, especially the annually changing cultivated crops.
3. Detecting the in-field variability of crop traits such as plant vitality, height, and biomass.

For all of the objectives, the research interest is to acquire the geoinformation itself, but the fundamental research goal is to find, and if necessary to develop, the most opportune method to achieve the desired output. Based on these objectives described above, the following research questions are derived:

- Which methods are best suited to achieving the objectives 1–3 from different remote-sensing image products in appropriate quality?
- How can existing external geodata be incorporated in the process? What is its benefit?
- Can the results be improved by incorporating existing geographic data, such as existing cadastral data about the agricultural land?
- How can radar remote sensing be used alone and in combination with optical remote sensing and external geodata to obtain LULC, crop type and crop traits?
- What are the most crucial remote sensing data characteristics for those objectives and what is their effect on the quality of the output?
- What are the essential characteristics of radar remote sensing images for those objectives?
- Which data characteristics are useful for evaluating the results?
- How can the desired outputs be generated cost-effectively and efficiently?

1.3 Outline

After the Introduction (1), the chapter Basics (2) focuses on the main concept of remote sensing for introducing the different kinds of data and their characteristics. A short introduction to the study sites is given next. Following that, the research papers are given in the chapters 3 to 8. They are organized based on the concept of increasing temporal and spatial resolution for selected applications from coarse to high, as shown in Figure 1.1. Table 1.1 demonstrates the different sensors and other datasets used in the chapters, including the research objective that is primarily pursued.

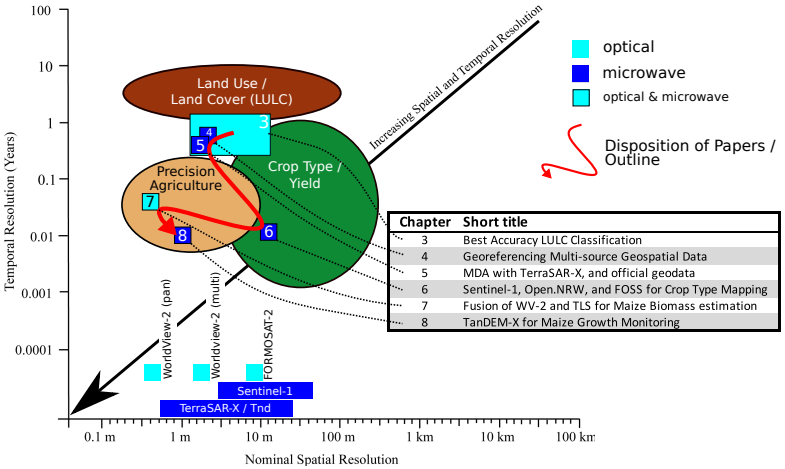

Figure 1.1: Concept of increasing spatial and temporal resolution, modified according to the relevant applications of this study. Modified after Jensen (2007).

The first research study, presented in chapter 3, introduces an innovative method to obtain general LULC, including crop type, from

			Satellite Images							Diverse Geodata						
			X-band SAR		C-band SAR			Optical		Elevation Models			In Situ Data			
Chapter	Short title	Study site	TerraSAR-X	TanDEM-X	Envisat ASAR	Radarsat-2	Sentinel-1	FORMOSAT-2	WorldView-2	S.R.T.M.	DGM-1	Official Geodata	Crop Distribution	TLS	Biomass	Research Objective
3	Best Accuracy LULC Classification	Qixing China	⋆		⋆	⋆		⋆		⋆			⋆			1+2
4	Georeferencing Multi-source Geospatial Data	Qixing China	⋆					⋆		⋆		⋆				2
5	MDA with TerraSAR-X and official geodata	Subset of the TR32	⋆							⋆		⋆	⋆			1+2
6	Sentinel-1, Open.NRW, and FOSS for Crop Type Mapping	Whole TR32 area					⋆				⋆	⋆	⋆			1+2
7	Fusion of WV-2 and TLS for Maize Biomass Estimation	Selhausen TR32							⋆		⋆			⋆	⋆	3
8	TanDEM-X for Maize Growth Monitoring	Selhausen TR32	⋆	⋆							⋆			⋆		3

Table 1.1: Overview of the different sensors and datasets that were combined, evaluated or analyzed in the different chapters

SAR and optical data in the study site Qixing farm, Heilongjiang, China. Chapter 4 introduces the novel idea of using the high geometric accuracy of the SAR satellite TerraSAR-X to produce a high-resolution geometric reference image for the diverse geospatial data of different scales and resolutions, thus making it possible to include any externally available data into the classification process, especially such data with a non-ideal geometric accuracy. Chapter 5 demonstrates the fusion of SAR remote sensing with such external data. The result is an enriched LULC map, containing the annual crop distribution obtained from the SAR data, as well as the LULC classes from the external data. In chapter 6, this idea is extended by relying on open data and open software only, making the approach much more low-cost. Once the annual crop distribution is available, additional analysis of the field crop status can be performed. Innovative examples of crop status monitoring are demonstrated in chapters 7 and 8. As can be seen in Figure 1.1, the resolution needs are greatly increased for such applications. Chapter 7 is based on high-resolution optical images from WorldView-2, which have a spatial resolution and accuracy high

enough to allow monitoring of within-field crop variances. Chapter 8 introduces the new innovative method of how to determine the plant height parameter from multitemporal satellite acquisitions from the TanDEM-X Constellation (TDM). The images had to be gained in the experimental, high-resolution, spotlight mode. Validation is performed using highly precise field measurement from Terrestrial Laser Scanning (TLS). In chapter 9, an overall discussion across the chapters and a discussion about putting the conclusions gained from the research in a scientific context are pursued. A conclusion is given in chapter 10.

2 Basics

2.1 Remote Sensing

Remote sensing is defined as "the art and the science of obtaining information about an object without being in direct physical contact with an object" (Jensen 2007: Preface). Typically the sensors are mounted onto aircrafts, satellites (Emery & Camps 2017) and nowadays also drones (Bendig et al. 2012). Also, ground-based sensors are possible, sometimes called proximal remote sensing. The present work focuses mainly on sensors mounted on board satellites flying in low earth orbit (LEO). Depending on the underlying principle, the sensors used can be divided into passive, optical, and active, mostly microwave, sensors (compare Figure 2.1. The concept of resolution – spatial, temporal, and spectral – guides the reader deeper into the topic of satellite-based remote sensing.

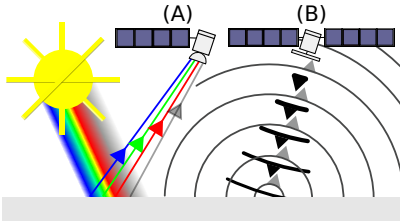

Figure 2.1: Schematics of passive (A) and active (B) satellite remote sensing, own representation, inspired by Albertz (2009: 10)

2.1.1 Optical Remote Sensing

The basic measurement principle of optical remote sensing is the detection of sunlight reflected from the earth's surface to create images (Emery & Camps 2017: 85). Depending on the sensor type, the intensity of electromagnetic waves in the visible and infrared part of the spectrum is measured. As depicted in Figure 2.1 (A), the radiation travels through the atmosphere before interacting with the earth's surface and again on the way towards the sensor. Consequently, such systems rely on an undisturbed path of the radiation through the atmosphere, which can be blocked by clouds (Emery & Camps 2017: 86). Additionally, the radiation interacts with the atmosphere while traveling through it. Atmospheric corrections are hence mandatory when accounting for such atmospheric effects in the imagery (Liang 2005: 197).

Under a clear sky, optical systems can retrieve spectral signals from the earth's surface. This spectral signature depends mainly on the chemical properties of an imaged land surface, and many characteristics can be retrieved.

The numerous deployed optical satellite systems differ quite considerable concerning their different scanning principles (Heipke 2017: 12-13). They either scan a long strip along their travel path or are tasked to acquired images over a specific Areas of Interest (AOIs). Among the ones that provide a long strip, the Landsat system, operated by the United States Geological Survey (USGS), is by far the most prominent. It provides the longest temporal record of satellite images. Most locations on earth were successfully imaged at least annually for the last 40 years (Roy et al. 2014). Although the current Landsat-8 system is technically superior to the first Landsat-1, its flight path is still the same, allowing time series analysis over the last four decades. Other satellite systems being tasked to take images are often company-owned, and monitoring of an AOI is usually done per request, which can be expensive. Such systems can be usually be turned towards the AOI once it is in sight. They generally allow a higher resolution (temporal, spectral and spatial) (Benediktsson

et al. 2012). A complete introduction into optical remote sensing is given by Heipke (2017), Campbell & Wynne (2011), Albertz (2009), Jensen (2007), and Lillesand et al. (2004).

2.1.2 Microwave Remote Sensing

The fundamental basis of microwave or radar remote sensing is the send and receive principle. An impulse of electromagnetic radiation is sent and received. The time delay between sending and receiving the signal is measured along with the intensity of the returned signal. The measured intensity of the signal depends on a complex electromagnetic interaction between the radar waves and the scene, and scattering depends on morphological and dielectric properties of the investigated medium (Emery & Camps 2017: 298). By combining multiple measurements of the intensity of the backscattered signal, it is possible to create a radar image of the observed surface. The modern, most widespread imaging radar technique is the Synthetic Aperture Radar (SAR) (Ulaby & Long 2014: 3).

Radar wavelengths used for remote sensing are divided into bands (Jutzi et al. 2017: 87). The shortest wavelength used by satellites is the X-band with a wavelength of about 3 cm. It is characterized by a small to no penetration depth into the examined medium; this is then characterized as surface remote sensing. The waves of the C-band are approximately 5 cm large and show a higher penetration depth. Penetration is further maximized with longer waves such as the ones from L-band (7.5 – 15 cm). Under the conditions of complete penetration into the medium, the process is described as volume scattering. The waves shorter than the X-band and longer than the L-band do not play a significant role for satellite remote sensing because they are significantly influenced by the atmosphere. However, the most important rule of thumb when choosing the wavelength for an application is that the dimensions of the structures under investigation should be roughly the same size as the wavelength (Emery & Camps 2017: 299).

Using polarimetric methods, the primary scattering processes within

a resolution cell can be determined (Lee & Pottier 2009). A first distinction can be made between surface and volume scattering. In the case of surface scattering, it can also be determined whether the number of scattering processes is odd or even. Double, i.e., an even number of reflections, is typical for urban areas. Typical for urban environments is also the occurrence of singular strong backscatterers, which manifest themselves as bright points in the radar image. The backscatter from rural areas is usually characterized by several so-called distributed scatterers per dissolution cell. Such distributed scatterers within one resolution cell are the cause of one major drawback of microwave images: – the grainy "salt and pepper"-like noise in all SAR images, which is called speckle. It makes visual interpretation more difficult and adds additional difficulty for image processing. Different techniques exist to deal with speckle:

- Multilooking: Neighbouring pixels are treated as individual radar measurements, and a new image that has a lower spatial resolution but contains less speckle is computed.

- Temporal Averaging: Images from SAR time-series are particularly well suited to temporal averaging. In a time series, all images are made from almost the same satellite position. That means that the geometric distortions induced by relief are the same in all images.

- Speckle Filters: Mostly focal filters with moving windows are developed to preprocess the SAR images specifically for different applications. In general, they seek to obtain the image characteristics with bright scatterers and spatially average homogeneous areas.

A central processing of the images captured by radar sensors is the conversion into a map projection. It is a prerequisite of further analysis, e.g., using a Geographic Information System (GIS). A common methodology for the projection is the range-doppler terrain correction and involves using a Digital Elevation Model (DEM) (Curlander

& McDonough 1991a). During this process, the height error of the DEM translates into a horizontal error of the processed radar image. Inaccurate elevation data can therefore be a source of error for the correct georeferencing of radar data. In addition to this correctable error, SAR images also exhibit relief-induced distortions due to their sideways viewing direction. While foreshortening is mainly corrected during the projection process, areas with radar shadow and layover contain no usable information (Richards 2009: 111).

Interestingly, elevation data is not only used to process SAR data but can also be generated by SAR sensors. The acquisition of SAR images from several acquisition positions allows interferometric analyses (Richards 2009: 183). Single pass and repeat-pass interferometry are the two alternative here. Single-pass interferometry is particularly well-suited to large-area topographic mapping. Famous examples are the global elevation models created by the Shuttle Radar Topography Mission (SRTM) (Rodriguez et al. 2006) and the TDM (Krieger et al. 2007). Repeat-pass interferometry is mainly used for detecting changes of the surface elevation between the acquisitions, such as in the mapping of earthquakes (Massonnet et al. 1993).

An extension to interferometry is tomography, in which SAR images from several positions are combined to obtain the vertical structure of the features in a scene. SAR sensor development is actively researched with awaited improvement from multifrequency SAR (Rosen et al. 2015), digital beamforming (Younis et al. 2003), multistatic sensor constellations (Kraus et al. 2017), and improved orbit constellations (Moreira et al. 2013) such as High Orbit SAR.

For a more complete description of radar remote sensing, its varied applications, and the historical development of the discipline, the interested reader is referred to the excellent textbooks by Woodhouse (2015), Ulaby & Long (2014), and Richards (2009).

2.1.3 Spectral Resolution

The spectral resolution is the number of different bands captured by remote sensing systems. In optical imaging systems, a distinction is

made between multispectral and hyperspectral systems, depending on the number of used bands. Multispectral systems sense the amount of energy in approximately 3–15 bands in particularly suitable areas of the optical, infrared, and thermal range. Hyperspectral systems scan the spectrum in specific areas with a continuous sequence of bands. Depending on sensor performance, several hundred bands can be scanned simultaneously.

With radar sensors, the concept of spectral resolution has to be widened. Due to technical limitations on satellites, only systems with one wavelength are currently in use (Ulaby & Long 2014). However, additional information about the examined surface is acquired by measuring the single frequency radar signal in different polarizations (Cloude 2010). Four different polarization combinations can be obtained by sending and measuring the radar signal horizontally and vertically. Polarimetric decompositions, such as the Pauli analysis, allow determination of the dominant scattering process on the ground. Odd (mostly single), even (mostly double) bounces and volume scattering can be distinguished. The polarimetric capabilities of SAR sensors increase the information content of the measurement, as different bands do in the optical domain. Hence, in the context of this work, not only the different radar wavelengths but also the amount of measured polarizations are considered when assessing the spectral resolution of the SAR images.

2.1.4 Spatial Resolution

The spatial resolution is the ability of a sensor system to separate signals from two adjacent objects (Emery & Camps 2017: 295). In most remote sensing scenarios, the size of a pixel of the analyzed images is understood as the spatial resolution. For most analyses based on optical data, this principle is sufficient. The optical sensors are often designed in such a way that one resolution cell of the sensor (Instantaneous Field of View) covers one pixel in the produced image. The size of a pixel, in reality, is then given as the spatial resolution of the sensor. To a certain extent, it depends on the viewing angle, with a

better resolution below the center of the sensors. However, the spatial resolution is mainly determined by the sensor design. Typical spatial resolution of space-borne imaging systems are MODIS (250–500 m) (Chen, Fedosejevs, et al. 2006), Landsat (15–30 m) (Roy et al. 2014), Sentinel-2 (10–60 m) (Drusch et al. 2012), or WorldView-2 (0.5–2 m) (Updike & Comp 2010).

For SAR sensors, it is important to keep the original definition of spatial resolution as the ability to separate two objects. The side-looking geometry of SAR imaging makes determining the resolution more complex. First, a distinction must be made between azimuth (along-track) and range (cross-track) resolution. The range resolution depends on the available bandwidth of the system and the incidence angle (θ). Contrary to optical systems, the range resolution is better, the steeper the angle. In consequence, SAR images have an increasing resolution the further away the sensor is (Woodhouse 2015: 269). Even more surprising is the determination of the azimuthal resolution of SAR images: The maximum possible resolution is equal to half of the length of the antenna (Woodhouse 2015: 274). Neither the wavelength nor the distance of the sensor from the target plays a role here (Emery & Camps 2017: 295).

SAR sensors offer the possibility to operate in different modes. During Spotlight operation, the antenna is steered during the overflight in such a way that the target is sensed for a longer time. This has the advantage of an increased azimuthal resolution, but the disadvantage of a reduced swath width (Woodhouse 2015: 287). To cover vast areas, the spatial resolution can also be reduced for the benefit of a very wide swath using the ScanSAR mode. This mode is suited for regional to global scale monitoring as it provides the necessary coverage (Woodhouse 2015: 287).

2.1.5 Temporal Resolution

Temporal resolution is the time it takes a sensor system to monitor the same area again. It is an essential consideration in all remote sensing applications (Campbell & Wynne 2011: 286). The temporal

resolution required depends on the specific application (Jensen 2014). Apparently, in the case of a disaster such as a flood, it is most important to gain information about the AOI as quickly as possible while, for planning purposes, an acquisition dating a couple of months back might be sufficient.

For satellite remote sensors, the available temporal resolution depends on the orbit and the scanning pattern of the satellite (Njoku 2013: 146). Continuous optical monitoring systems usually have a limited temporal resolution as it depends on the revisit time, which is the time until the satellite reaches the same position in orbit. Landsat-8, for example, has a revisit time of 16 days (Roy et al. 2014). Only in these precisely scheduled time windows is it possible for these sensors to take images. If clouds obscure a clear view on the earth's surface during these time windows, no information can be gained from the surfaces. The optical systems with steering capabilities potentially have a much higher temporal resolution. WorldView-2 [1], for example, is equipped with extreme steering capabilities, giving the satellite an almost daily chance to acquire an image (Updike & Comp 2010). However, to get an analyzable image, the AOI has to be cloud-free, and the image is only taken per request. As each acquisition has a high price, a high temporal resolution is expensive. Furthermore, the steerable satellite scan the earth's surface at varying off-nadir angles. Analyzing these images needs consideration of the bidirectional reflectance distribution function (Leroy & Roujean 1994), resulting in increased analysis complexity.

In the case of clouds, SAR imaging is the only alternative, as the microwaves can penetrate clouds (Ulaby & Long 2014; Woodhouse 2015). There is less difference between the potential and the actual imaging capabilities of SAR sensors, giving them an increased temporal resolution. The recently deployed Sentinel-1 constellation (Torres et al. 2012), for example, has a continuous monitoring principle with a revisit time, from the same satellite orbit, of 6 days. As the swaths of

[1] Images of the WorldView-2 Satellite system are used in the study described in chapter 7

the orbits overlap, an average revisit once every two days is achieved.

2.1.6 Dilemma of Swath Width/Extent, Spatial Resolution and Temporal Resolution

The resources on board a satellite are limited. The imaging system usually determines the spatial, the spectral, and sometimes even the temporal resolution. Notably, doubling the spatial resolution means four times as much data that has to be captured, stored, and transmitted to the ground. Regarding the extent of the images, there is a general conflict between a wide swatch and a high geometric resolution. Usually, higher spatial and spectral resolution systems have a smaller area they can image simultaneously. This limits the temporal resolution. The high spatial resolution of WorldView-2, for example, is only available at maximum swatch width of only 16.4 km (Updike & Comp 2010). The other extremes are sensors that can potentially cover the whole world daily, such as MODIS (Chen, Fedosejevs, et al. 2006). However, the maximum available spatial resolution is then 250 m, which is too coarse for many applications.

While optical sensors have to be chosen to match the application's resolution need, SAR sensors can be programmed according to the application's need for coverage and spatial resolution (Ulaby & Long 2014). However, the conflict persists. The higher resolution spotlight mode always has reduced swath, and the ScanSAR modes covering larger areas are of lower spatial resolution. The currently implemented strategy to deal with the problem is the installation of satellite constellations, where more than one satellite is installed on the same path with a time delay.

In the optical domain, the RapidEye system of five satellites was a significant milestone (Mulla 2013), as it provides daily coverage with 6.5 m spatial resolution. One other recent example is the Sentinel-2 constellation (Drusch et al. 2012). Another approach tries to maximize the temporal resolution of high spatial resolution imaging systems by deploying a fleet of CubeSats. CubeSats are smaller, less expensive satellites using automotive grade electronics. The satellite

constellation of the private company Planet has spatial resolutions between about 3 and 5 m. The constellation currently comprises more than 200 optical satellites. They aim to cover the whole earth's surface daily (Zimmerman et al. 2017).

For microwave sensors, examples are the TanDEM-X / TerraSAR-X / PAZ constellation (Gantert et al. 2013), Radarsat constellation (Thompson 2015), and the Sentinel-1 constellation (Torres et al. 2012). Another way out of the dilemma comes from the current SAR sensor development. The concept of High Resolution Wide Swath (HRWS) promises providing a high coverage and a high spatial resolution simultaneously (Cerutti-Maori et al. 2014).

2.1.7 Remote Sensing Image Classification

Through digital image classification, pixel values are assigned to classes (Campbell & Wynne 2011: 335). Supervised approaches rely on reference areas, which are mapped in field surveys. Those reference areas are then used to train the classifier and to validate the accuracy of the derived map (Congalton & Green 2008). Numerous classifiers and different classification approaches have been evaluated (Lu & Weng 2007). One such method is Maximum Likelihood, which is based on average class statistics to obtain the parameter that is most plausible (Jones & Vaughan 2010: 189). In the context of this work, the Random Forest (RF) classifier played a significant role. It was introduced to remote sensing Pal (2005) and used for LULC determination (Rodriguez-Galiano et al. 2012). Other algorithms of LULC classification are artificial neural networks (Atkinson & Tatnall 1997) or support vector machines (Pal & Mather 2005). The choice of the classification unit leads to a further differentiation of the previous methods. Mostly, pixel-based methods are used (Lu & Weng 2007). However, it is also possible to segment and classify spatial objects from the image data or to use objects from external databases for classification. These methods are considered as object-based methods (Blaschke 2010).

2.2 Application of Remote Sensing

2.2.1 Land Use / Land Cover Mapping

The answer to the geographic question of *what is where?* results in land cover – the actual type of features present on the ground (Lillesand et al. 2004: 215). The human activity associated with the features determines the land use (Fisher et al. 2005: 86), which is of central importance in economic geography studies, such as the famous *theory of land use* by Von Thünen (1875). Although there is a difference in meaning, land use is closely connected with land cover and hence in the present study considered together as LULC. Knowledge of LULC is of central importance for land planning and land management (Lillesand et al. 2004: 215). Comparing LULC at different points in time reveals the LULCC, which is of central importance to environmental change and sustainable development (Xiubin 1996).

Remote sensing is acknowledged as an excellent method to determine LULC through image classification (Campbell & Wynne 2011: 585). The basic classification scheme for such applications dates back to Anderson et al. (1976), who lay out the principles for mapping schemes. There are efforts to provide geodata of general LULC for large areas. The European Corine Land Cover initiative, for example, provides LULC information for most European Union (EU) countries and describes types of cover in 44 different classes, such as settlement, vegetation, and water bodies. The maps are based on remote sensing data and have a scale of about 1:100,000 (Büttner et al. 2004).

Additionally, incorporating any external geodata has been shown to improve general LULC-classifications (Albertz 2009: 165). The concept of the Multi-Data Approach (MDA) has been proposed to both include multitemporal remote sensing acquisitions, if needed from multiple sensors, and existing external geodata (Bareth 2008). It is achieved by combining all information in a GIS.

2.2.2 Crop Type Mapping

LULC is of particular significance when analyzing production characteristics of agricultural landscapes (Spielmann 1989: 16), as agriculture is the predominant land use activity on the planet (Liang et al. 2012). Crop type mapping or crop distribution estimation is a special kind of LULC-mapping and reveals the spatiotemporal pattern of agricultural crops (Albertz 2009: 199). Crop type maps enable agro-ecosystem-modeling (Reichenau et al. 2016), deploying agricultural monitoring systems (Machwitz et al. 2018), and yield forecasting (McNairn et al. 2014). They play a crucial role in agricultural monitoring systems (Fritz et al. 2018). However, agriculture is the economic sector with the highest spatial-structural diversity (Spielmann 1989: 16). Hence, crop type mapping is challenging for three reasons:

- In regions with an temperate climate, the grown crops usually follow seasonal patterns connected to the phenology. In such regions, some crops are only distinguishable at a certain period of the year.
- Regions with no seasons have varying growing patterns, sometimes with several harvests throughout the year.
- The grown crops vary considerably depending on the physical properties of the landscape such as climate, relief, and soil type. Each region has its own specialties, which need to be understood by the creator of the maps (Albertz 2009: 199).

To overcome these challenges, remote sensing image classification has to take these factors into account. In practice, it has been shown that only multitemporal acquisitions are suitable for differentiation between field crops. Therefore, the temporal resolution is of critical importance (Van Niel & McVicar 2004b). Its precise determination depends on the agricultural practices and growing patterns of the AOI. The spatial resolution also needs to vary with the AOI, as it depends

on the field size (Foerster et al. 2012; Duveiller & Defourny 2010).

Spectrally, optical remote sensing using the visible and near-infrared domain has long been used for crop type mapping (Foerster et al. 2012; Vinciková et al. 2010). However, optical sensors have the apparent disadvantage of not working in cloudy conditions, which could significantly lower the temporal resolution (Whitcraft et al. 2015; Waldhoff et al. 2017). As a solution, microwaves have been acknowledged to have a high potential for differentiating crops (Bush & Ulaby 1978). Especially the spatiotemporal difference of polarimetric SAR observations over crops (Koppe et al. 2013) enable crop type mapping from polarimetric SAR (Sun et al. 2018; McNairn et al. 2014). A combination of optical and radar sensors can improve the accuracy and make the classification robust over clouds (Blaes et al. 2005).

The concept of MDA introduced above has also been used in the context of crop classifications. Waldhoff et al. (2012) demonstrated the successful application of the MDA by combining optical remote sensing data with external data from the Land Parcel Identification System (LPIS) and German Authoritative Topographic-Cartographic Information System (ATKIS).

2.2.3 Mapping of Crop Traits

For assessing ecosystems services, remote sensing has been extensively used to assess plant traits such as plant height, plant nitrogen, phosphorus content/ concentration, and leaf mass per area (Liang et al. 2012). When optical remote sensing is used, the photosynthetic activity can generally be predicted from the proxies fraction of absorbed photosynthetic radiation and light-use efficiency (Houborg et al. 2015). Especially hyperspectral remote sensing has proved beneficial in detecting crop traits (Thenkabail et al. 2000). However, all interpretations of remote sensing signals into the traits mentioned above are ambiguous, and large uncertainties exist (Carlson & Ripley 1997; Homolova et al. 2013).

Recently, non-spectral measurements of plants were found to lower such uncertainties. Multitemporal plant height measurements, either acquired through a TLS (Tilly, Hoffmeister, Cao, et al. 2014) or from unmanned aerial vehicles (Bendig et al. 2015) were successfully combined with optical measurements for improved biomass predictions. Structural plant parameters are also captured by SAR-system, which has long been acknowledged for being sensitive to plant traits (Bush & Ulaby 1978; Foody et al. 1994; Brisco & Brown 1995; Skriver et al. 1999; McNairn & Shang 2016). Multitemporal SAR data from TerraSAR-X acquisitions were found to be sensitive to the growing stage and biomass of rice (Koppe et al. 2013). For height mapping of rice, a promising method has recently been developed using the TDM (Erten et al. 2016).

2.3 Data Demand for Agricultural Systems

2.3.1 Agricultural Monitoring Systems

As stated above, agricultural monitoring systems play a key role in addressing the problems agricultural production is and will be facing (Wu et al. 2014). The available input data is central in getting sound information from the systems, and remote sensing plays a significant role in the creation of such input data (Atzberger 2013). It was no coincidence that the first nationwide system of this kind was based on information generated by remote sensing (Idso et al. 1977). Furthermore, remote sensing has been heavily researched as a methodology to support the systems (Davis & Tarpley 1983; Atzberger 2013).

However, Fritz et al. (2018) compared the global systems already deployed and identified significant input data gaps. The quality of global cropland maps, crop type, and crop yield data was identified as unsatisfactory, yet as extremely critical for the systems. One of the reasons at least for global applications is that sufficient cloud-free data acquired in the same season with a high temporal resolution is

rarely available (Ban et al. 2015).

2.3.2 Precision Agriculture

Zecha et al. (2013) describe satellite remote sensing as ideal for precision farming but mention the coarse spatial resolution and the limited availability with clouds making it unusable for precision farming applications. Exact numbers for the minimally required spatial resolution depend on the intended applications, the capabilities of the machines, and the farm characteristics. Mulla (2013) reports typical spatial resolutions for the following applications:

- Variable rate application of fertilizer: 5–10 m
- Variable rate irrigation: 5–10 m
- Estimation of spatial patterns in crop biomass or yield: 1–3 m
- Variable rate spraying of herbicides for spot weed control: 0.5–1 m

Besides the lack of sufficient spatial resolution, the other main historical limitation of remote sensing for site-specific management is the limited temporal resolution (Whelan & Taylor 2013). In the case of optical imaging, clouds [2] throughout the vegetation period heighten the problem (Whitcraft et al. 2015; Waldhoff et al. 2017). However, timing is crucial for precision farming, as the geo-information needs to be available before the management is applied. This timing depends on the specific application. A couple of days delay between sensing and application might be acceptable for applications such as variable rate fertilization (Goense 1997: e.g.). In the case of irrigation management, precipitation can change the water requirements within hours (Ozdogan et al. 2010). This timing issue can be overcome by using SAR; the above-described sensitivity of SAR-systems for

[2] Note the only small cloud in the third scene depicted in the Figures 7.1 and 7.2 is positioned exactly over our AOI.

plant traits makes them potentially valuable for precision farming (Moreira et al. 2013). Yang et al. (2018), for example, use SAR to determine rape biomass within season for improved site-specific crop management.

2.4 Study Sites

Chapters 3 and 4 have the area of Qixing farm as their study site. The author had an extended field visit for the whole of the growing period of 2009. During that time, besides collecting much rice-monitoring-related field data, a mapping campaign with emphasis on crop type was performed. The mapping results of that campaign were later used as ground truth for the case study described in chapter 3. The field stay was organized by the International Center for Agro-Informatics and Sustainable Development (ICASD), a cooperation between the China Agricultural University, Beijing (China) and the University of Cologne.

The studies presented in the chapters 5–8 were carried out within the region of the Transregional Collaborative Research Centre 32 (TR32). The proximity of this area to the living and working place of the author made it possible to easily visit the studied fields. Numerous field visits were made to gain a better understanding not only of the particularity of the landscape (Pocock 1983: 1) but also of its image in different remote sensing products. Both the Chinese and the German study sites are shortly portrayed below.

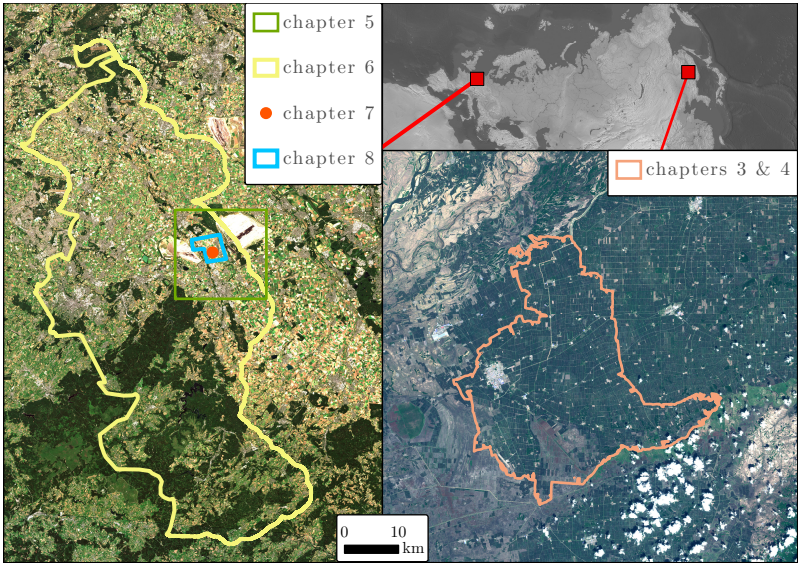

Figure 2.2: Overview of the study sites. Image Background: Sentinel-2 images, acquired on 2018-07-02 (left) and 2018-08-23 (right), Copernicus Sentinel data (2018)

2.4.1 Qixing Farm, Sanjiang Plain, China

Qixing farm has an area of about 1000 km^2 and is situated in the Sanjiang plain, which lies in China's most-northern province Heilongjiang. Jiansanjiang, with 230,000 inhabitants, is the principal city on the farmland and was also the basis of the research station of the ICASD. Maps of the area can be found in Figures 3.1 and 4.1. Sanjiang means "three rivers". These three rivers are the Songhua, Heilong, and Wusuli, which formed the alluvial plain between them. As an alluvial plain, the area is characterized by deficient relief energy, with most parts being completely flat. Once an inaccessible wetland, cultivation of the area began from 1949 onwards (Staiger et al. 2003: 298) (Gao

& Liu 2011). While the Sanjiang plain is still important as a wetland for the ecosystem of China (Wang et al. 2006), significant parts of it have been transformed to arable land, building a vital food production location for China (Song et al. 2014).

The climate is continental and influenced by monsoonal effects. Consequently, as can be seen in Figure 2.3, both precipitation and temperature have their distinct maximum in the summer months. The continentality results in a high seasonal variability of the temperature, which is one of the world's highest for this latitude (Zhao 1986: 105). Following the Köppen-Geiger climate classification, the area is classified as DWA (Cold (Continental), Dry winter, hot summer), with DWB (warm summer) starting nearby. The frost-free period lasts for about 120 to 145 days, and average yearly precipitation is between 500–600 mm (Zhao 1986: 105).

The warm summer in combination with sufficient precipitation allows intensive farming with one single, yet high, yield per year. The most significant crop regarding area is paddy rice, but summer wheat, maize, soybeans, and pumpkin are also grown here. A detailed crop classification of the Qixing farm can be found in chapter 3.

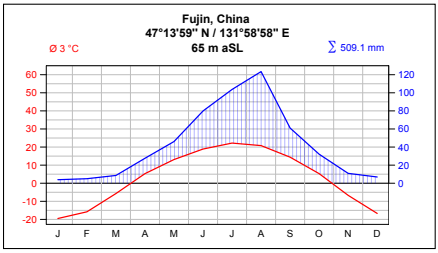

Figure 2.3: Walter Lieth climate diagram for Fujin, China, with is about 40 km away from the chinese AOI. Own creation with data acquired through (NOAA 2018).

2.4.2 Rur Catchment, Germany

The TR32 is located in the west of Germany and mainly situated within the federal state North Rhine-Westphalia (NRW). The area is a north-south oriented, up to 36 km wide strip of approximately 90 km length. In the west, it is framed by the borders to The Netherlands and Belgium, exceeding beyond the border in some areas. It was chosen to cover the whole catchment of the river Rur, which flows in a south-north direction through the TR32. As can be seen in Figure 2.2, four chapters of the present work are situated here. In chapter 6, a crop classification of the whole German part of the TR32 is described, an area covering about 2400 km^2.

From a geological point of view, the area can be divided into two major parts. While the northern part lies in the Lower Rhine Bay, the southern one covers the mid-range mountains, Eifel, as a part of the Rhenish Massif. Those mid-range mountains have higher relief energy, and the soils are less fertile (Ribbert 2010). Consequently, pasturable land is more common than arable land. The northern part is characterized by Pleistocene loess deposits which formed fertile soils, such as Brown Earth and Luvisol. They provide good growing conditions and the area is intensively used for agricultural production.

Figure 2.4 illustrates a Walter-Lieth diagram of the nearby Jülich research center climate station. As can be seen, the climate is temperate, fully humid with a warm summer, which is Cfb according to the Köppen-Geiger climate classification. The mean temperature is 10 °C, and the annual average rainfall is a little less than 700 mm. As a result many crops such as cereals, are grown over winter. Other important crops are potatoes, maize and sugar beet, which are usually grown in summer.

The studies presented in chapters 5, 7, and 8 were carried out in the northern, more fertile part, more precisely on the eastern edge of the TR32 research area, on the strip of land between the two open-pit mines Hambach and Inden. The intensely monitored maize field is situated at the transition between the lower and upper terrace of the Rur river (Geologischer Dienst NRW 2018). As

this border transects the field, it is characterized by inhomogeneous field conditions.

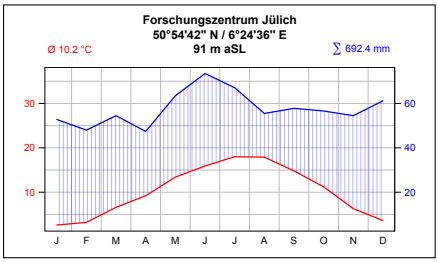

Figure 2.4: Walter-Lieth climate diagram for Jülich, Germany. Own creation with data acquired through (NOAA 2018).

3 Best Accuracy Land Use / Land Cover (LULC) Classification to Derive Crop Types Using Multitemporal, Multisensor, and Multi-Polarization SAR Satellite Images

Christoph Hütt[1], Wolfgang Koppe[2], Yuxin Miao[3], Georg Bareth[1]

Published in: Remote Sensing, 2016 / 8, 8.
Original manuscript is embedded in dissertation format.

1. Institute of Geography, GIS & Remote Sensing Group, University of Cologne, 50923 Cologne, Germany,
e-mail: {christoph.huett} {g.bareth}@uni-koeln.de

2. Airbus Defence and Space, 88039 Friedrichshafen, Germany,
e-mail: wolfgang.koppe@astrium.eads.net

3. Department of Plant Nutrition, China Agricultural University, Yuanmingyuan West Road No. 2, 100193 Beijing China,
e-mail: ymiao@cau.edu.cn

3.1 Abstract

When using microwave remote sensing for LULC classifications, there are a wide variety of imaging parameters to choose from, such as wavelength, imaging mode, incidence angle, spatial resolution, and coverage. There is still a need for further study of the combination, comparison, and quantification of the potential of multiple diverse radar images for LULC classifications. Our study site, the Qixing farm in Heilongjiang province, China, is especially suitable to demonstrate this. As in most rice growing regions, there is a high cloud cover during the growing season, making LULC from optical images unreliable. From the study year 2009, we obtained nine TerraSAR-X, two Radarsat-2, one Envisat-ASAR, and an optical FORMOSAT-2 image, which is mainly used for comparison, but also for a combination. To evaluate the potential of the input images and derive LULC with the highest possible precision, two classifiers were used: the well-established Maximum Likelihood classifier, which was optimized to find those input bands, yielding the highest precision, and the RF classifier. The resulting highly accurate LULC-maps for the whole farm with a spatial resolution as high as 8 m demonstrate the beneficial use of a combination of x- and c-band microwave data, the potential of multitemporal very high resolution multi-polarization TerraSAR-X data, and the profitable integration and comparison of microwave and optical remote sensing images for LULC classifications.

3.2 Introduction

Satellite remote sensing is used as a powerful tool to monitor the Earth's surface, particularly in producing LULC classifications (Foody 2002; Green et al. 1994). In general, creating LULC classifications builds upon two imaging methods: optical and microwave remote sensing. Both sensing approaches imply distinct advantages and disadvantages. While optical sensors rely on reflectance and cloud free conditions, microwave sensors only capture the backscatter in a given

wavelength (Gomez-Chova et al. 2015). Examples of optical LULC analysis on a global scale are given by Chen et al. (2015), for example, and for a regional scale by Lo & Fung (1986), and Immitzer et al. (2016). Microwave imaging using synthetic aperture radar (SAR) images for LULC emerged in the 1980s, and examples are described by Bryan (1983) and Dobson et al. (1995). The combined analysis of optical and microwave imagery to use the advantages of both systems for LULC classifications was investigated by Solberg et al. (1994), McNairn, Champagne, et al. (2009), Forkuor et al. (2014), and Blaes et al. (2005).

A common information gap in LULC classifications and products are detailed crop classes within the arable land use class (Atzberger 2013). For numerous agricultural applications, the spatial information of arable land is not sufficient. This is true for agro ecosystem modeling (Lenz-Wiedemann et al. 2010), yield estimation (Vibhute & Gawali 2013), subsidy control (Schmedtmann & Campagnolo 2015), and retrieval of biophysical plant parameters on regional scales (Zhao, Hütt, et al. 2015). However, using satellite remote sensing to differentiate crops is a demanding task, as different crop types have similar reflection properties in remote sensing images for some periods of the year (Waldhoff et al. 2012). Those crops can only be separated from each other by a multitemporal analysis, which considers the phenology of the investigated crops (Gomez-Chova et al. 2015). Multitemporal and multispectral optical and infrared remote sensing has proved to be an effective approach to discriminate different crops (Pinter Jr et al. 2003). However, as mentioned above, the availability of optical satellite-borne imagery is sometimes limited due to cloud cover in the region of interest. Therefore, for many agricultural regions it is a coincidence whether optical images from the right time are available or not, which makes crop classifications based on optical imagery unreliable.

The key advantage of satellite-borne SAR imaging is the independence from cloud cover, and as it is an active sensing system, also from sun-induced reflection. Consequently, SAR imagery has become an important tool to distinguish agricultural crops (Bush & Ulaby

1978; Hoogeboom 1983; Blaes et al. 2005; Bargiel & Herrmann 2011; McNairn et al. 2014). Sophisticated SAR systems provide a temporal resolution that lies within a few days, with a spatial resolution as high as 20 cm (Prats-Iraola et al. 2012). Such systems are already in application to deliver annual crop inventories on regional levels (McNairn, Champagne, et al. 2009). Recently, polarimetric SAR images have been analysed using decomposition theorems such as the alpha/entropy decomposition (Cloude & Pottier 1996), which increases the accuracy of LULC analysis from microwave data. Especially in rice-growing regions (which usually have a very high cloud cover during the growing season), polarimetric SAR has been intensively used as a monitoring tool (Tennakoon et al. 1992; Chakraborty et al. 1997; Ribbes 2010; Wu et al. 2011; Koppe et al. 2013; Brisco et al. 2013).

However, there is a wide choice of different remote sensing satellites, radar, and optical. While optical satellites usually operate in one imaging mode, radar satellites can be programmed to work in different configurations. The user has to choose the polarization configuration, the incidence angle, and the spatial resolution as a result of the chosen imaging mode (Breit et al. 2010). Interestingly, only a few studies such as McNairn et al. (2014) deal with multisensor data (i.e., the combination and comparison of SAR images from more than one satellite). Furthermore, to the knowledge of the authors, no other studies investigate the comparison of different imaging modes from the same sensor in the context of crop classification. In addition, the image information gained from optical and microwave sensing methods contains different LULC properties. Consequently, combined approaches of using optical and microwave images can improve the LULC analysis (Solberg et al. 1994; Blaes et al. 2005; McNairn, Champagne, et al. 2009; Forkuor et al. 2014).

For a LULC analysis, an extensive set of ground truth is typically mapped and separated into two datasets. One dataset is used to train the classifier for the automated classification of the entire image. The second dataset is used to evaluate the classification's accuracy. Results of the evaluation are summarized in a confusion matrix (Foody 2002).

Based on the confusion matrix, statistical accuracy parameters are calculated. One is the Overall Accuracy (OA) (Congalton & Green 2008), which counts pixels that are correctly classified in the reference divided by all pixels that are taken for reference. This procedure applies for both optical and microwave image classification.

Considering the need for multitemporal and multisensor radar image classification in a combined approach with optical image analysis for crop classification, this study is framed by three objectives. (i) To investigate how to derive LULC classifications from multitemporal, multisensor, and multi-polarisation SAR satellite images with the best possible accuracy; (ii) to evaluate the potential of those images and the combinations to obtain a crop type map with a spatial resolution as high as 8 m; (iii) to identify the best combination of available input images that yields the best classification accuracy for each respective part of the study area.

3.3 Study Area and Data

The study area is the Qixing farm, situated in northeast China, in the Sanjiang Plain (Figure 3.1). The climate is continental and influenced by monsoonal effects. As a result, the area is characterized by a cold and dry winter and a relatively warm summer with sufficient precipitation for high-yield agriculture (Zhao 1986). The growing season is short and lasts for about five months. Thus, only one yield per year is possible. Main crops include: paddy-rice, summer-wheat, soya-beans, pumpkins, and maize. Additionally, the terrain of the whole farm is virtually flat.

During the 2009 growing season, between June and October, we collected ground data of field crop distribution. A total of 22 agricultural fields, 3 areas of rural villages, and one lake, covering an area of about 5 km^2 were investigated several times. Based on the observations, their spatial extents were transferred to a Geographic Information System (GIS). Table 3.1 shows the spatial statistics of the dataset. The collection of fields was equally divided into a training dataset and

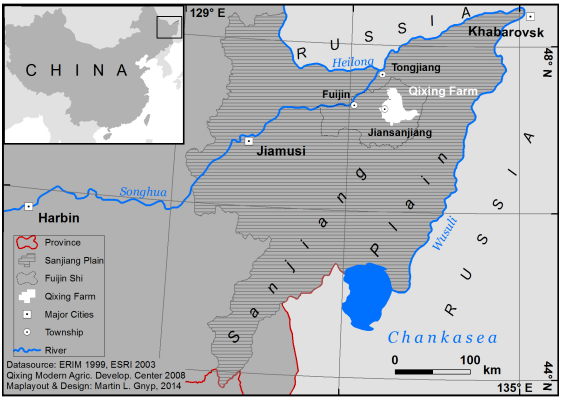

Figure 3.1: Location of study site, modified after Gnyp et al. (2014).

an independent validation dataset. Different fields were either used for training or validation. Unfortunately, only one pumpkin field, one lake, and one deciduous forest were situated in the area of interest. In those cases, we divided single areas into two parts and used one part for training and the other for validation. All observed fields lie in an area covered by all remote sensing images. Furthermore, the area of the validation was roughly matched to be representative of the study area.

As described in Section 3.2, optical satellite images can be used exclusively under cloud-free conditions in the area of interest. In the year of investigation, we observed unusually long periods of rainy and cloudy weather. The consequence was that only the FORMOSAT-2 image from the beginning of August had a low enough cloud cover over the area where the training and validation field data were collected. Various other optical images could not be used because of too many clouds in the images.

Since SAR imaging is not influenced by clouds and haze in the atmosphere, all 12 microwave images obtained during the growing season of 2009 could be used for this study. Acquisition numbers 1–4

Land Use/Land Cover	Number of Polygons	Extent (km^2)	Area Used for Classification (%)	Area Used for Validation (%)
Coniferous Forest	3	0.065	27	73
Decideous Forest	2	0.120	43	57
Maize	2	0.169	76	24
Pumpkin	1	0.173	50	50
Rice	6	1.576	26	74
Soya	8	1.858	57	43
Urban	3	0.958	30	70
Concrete	1	0.002	100	-*
Water	1	0.004	52	48

* dissolved into the class "urban".

Table 3.1: Field data collected during the 2009 growing season that is covered by all remote sensing images.

No.	Date	Sensor	Mode	Ground Res. Az × Rg (m)	Polarisation	Pass	Extent (km)	Rice Growth Stage
1	5 July 2009	TerraSAR-X	Spotlight HS	1.76 × 1.43	HH, VV	Asc.	7 × 11	Stem elong.
2	16 July 2009	TerraSAR-X	Spotlight HS	1.76 × 1.43	HH, VV	Asc.	7 × 11	Booting
3	27 July 2009	TerraSAR-X	Spotlight HS	1.76 × 1.43	HH, VV	Asc.	7 × 11	Heading
4	7 August 2009	TerraSAR-X	Spotlight HS	1.76 × 1.43	HH, VV	Asc.	7 × 11	Flowering
5	26 June 2009	TerraSAR-X	Stripmap	1.89 × 1.57	VV	Desc.	30 × 50	Tillering
6	7 July2009	TerraSAR-X	Stripmap	1.89 × 1.57	VV	Desc.	30 × 50	Stem elong.
7	18 July 2009	TerraSAR-X	Stripmap	1.89 × 1.57	VV	Desc.	30 × 50	Booting
8	29 July 2009	TerraSAR-X	Stripmap	1.89 × 1.57	VV	Desc.	30 × 50	Heading
9	9 August 2009	TerraSAR-X	Stripmap	1.89 × 1.57	VV	Desc.	30 × 50	Flowering
10	25 June 2009	Radarsat-2	Fine	4.8 × 8.93	HH, HV	Asc.	54 × 53	Tillering
11	29 July 2009	Radarsat-2	Fine	4.8 × 6.96	HH, HV	Desc.	54 × 53	Heading
12	26 June 2009	Envisat	ASAR APS	3.88 × 11.85	VV, VH	Asc.	60 × 107	Tillering
13	9 August 2009	FORMOSAT-2	multispectral	8	(4 Bands)	-	28 × 34	Flowering

Table 3.2: Remote Sensing acquisitions that were used in this study.

(Table 3.2) are a time series of very high resolution TerraSAR-X images in dual polarization. A second time series consists of images 5–8 (Table 3.2), which were taken in stripmap mode with only one polarization and have a lower spatial resolution. While the data density of this time-series is generally lower, the covered area is about 20 times larger, but still does not cover the whole area of the farm. Dataset 10–13 (Table 3.2) are from the Radarsat-2 and Envisat satellites. They operate in c-band, which means increased wavelength and therefore sensitivity to other properties of the ground. While they have a

lower spatial resolution, more area is imaged at once. Indeed, the Envisat image is the only one covering the whole area of the farm. The polarizations of the Radarsat-2 acquisitions are horizontal-send–horizontal-receive (HH) and horizontal-send—vertical receive (HV). For the Envisat acquisition, the polarization configuration is the same, but the directions of the polarizations are inverted (VV and VH).

3.4 Methods

As described in Section 3.3, the remote sensing data differ from each other in one basic aspect: The TerraSAR-X Spotlight data (dataset no. 1–4, Table 3.2) and the cloud-free part of the FORMOSAT-2 image only cover the area where the ground data are taken. The TerraSAR-X stripmap data (datasets no. 5–9,Table 3.2), the Radarsat-2, and Envisat data cover a much wider area, but with a decreased spatial resolution. Therefore, we divided our data into two subsets. One contains the data that cover a small area at a very high resolution (dataset no. 1–4, 13). The other subset contains images no. 5–12 (Table 3.2), and is used to provide land use information for the whole Qixing farm, which covers an area of about 1070 km^2.

To process the remote sensing images, the following software packages were used: The polarimetric radar images were processed with Polsarpro. The European Space Agency (ESA) provided the Next ESA SAR Toolbox (NEST) (new name: SNAP/ Sentinel-1 Toolbox), which was used for speckle filtering and range doppler terrain correction. For the co-registration of the FORMOSAT-2 image, we used ENVI 5.0. The Maximum Likelihood classification and its optimization (Section 3.4.4) and the error assessment was done using ArcGIS 10.1 and the python scripting extension. The python script can be downloaded freely using the associated enrichments. The implementation of the RF Classifier (Section 3.4.5) was done using the statistics software R (R Core Team 2016) (Version 3.2.5) and the randomForest package (Liaw & Wiener 2002) (Version 4.6.12), with a script published by (Horning 2013).

3.4.1 Retrieval of Polarimetric Features

The measured signal from coherent polarimetric SAR systems can be analysed by determining the covariance matrix C and the coherency matrix T from the measured signal. The elements of those matrices can be directly used as input parameters in LULC classifications. As both matrices are related to each other, and Alberga et al. (2008) found out that the two matrices lead to similar classification results, we concentrated on the elements of the covariance matrix C. Furthermore, by eigenvector analysis of T it is possible to calculate entropy and alpha, which can be related to backscatter mechanisms on the ground. This is an advantage to single polarization systems and significantly improves the results of LULC classifications (Qi et al. 2012).

In this study, we obtained the possible parts of C from the dual polarimetric data from Radarsat-2 (datasets 9 and 10, Table 3.2) and TerraSAR-X (datasets 1–4, Table 3.2). In the case of the Radarsat-2 images, the cross elements of C (c12i, c12r) were excluded, because visual inspection revealed poor quality and unsuitability for LULC mapping. Additionally, based on the spatially averaged (5×5 window) coherency matrix T, we calculated the dual-pol entropy, alpha angle, and the degree of polarization (Cloude et al. 2012). In total, we derived seven individual rasters for each coherent TerraSAR-X polarimetric radar scene, and five for each Radarsat-2 scene.

3.4.2 Preprocessing of the Remote Sensing Data

For the Envisat ASAR image (dataset 12, Table 3.2), polarimetric decompositions as described in Section 3.4.1 is impossible, as the signal is not recorded coherently (Raney & Hopkins 2011). In this case, only the amplitudes of the radar signal were computed and used for the LULC classification. The same applies for the TerraSAR-X scenes that only contain one polarization (datasets 5–9, Table 3.2).

For all radar data, the next step was a multilooking, which decreases the pixel size, but reduces the speckle effect. Range and azimuth multilooking windows were chosen to roughly match the 8 m pixel size

of the final classification.

The orthorectification of radar images is a transformation from slant range radar geometry to ground range, and involves the usage of a digital elevation model (DEM). We used data from the SRTM in 90 m resolution (Jarvis et al. 2008) to carry out a range-doppler terrain correction as described by Curlander & McDonough (1991a). During this process, the final pixel size of 8 m was determined. We chose 8 m for all products in order to be able to compare and combine the images with the optical FORMOSAT-2 image on the pixel level. Furthermore, 8 m is a good compromise between oversampling the Radarsat-2 and Envisat ASAR data and undersampling of the TerraSAR-X data. Additionally, 8 m per pixel seems to be a decent size to determine fields in this region, as our field investigations have shown that they are rarely smaller than 20 m in diameter.

The orthorectification described above has to be carried out with high spatial precision for the intended pixel-based analysis. Therefore, it is worth looking at the anticipated positional error of the orthorectified radar images. It mainly depends on the location error of the position of the sensor platform during image acquisition and the error of the used DEM (Curlander & McDonough 1991a). The first error is known to be low for TerraSAR-X (Nonaka et al. 2008), Radarsat-2 (Morena et al. 2004), and Envisat (Doornbos et al. 2002). Concerning the second error, Rodriguez et al. (2006) state the absolute error of the SRTM to be below 10 m. The resulting low positional error of the images is required for the combined pixel-based processing of the scenes. For a more detailed analysis of this aspect, see (Zhao, Hütt, et al. 2015), where a subset of the same dataset was used to create a spatial reference for various other datasets.

In the next step, two speckle filters were applied to all images in the ground range to decrease the speckle effect. First, the gamma map filter with a with a 5×5 kernel size, and second, a rather simple median-filter with a kernel size of 3×3. More radar-specific image filters resulted in residuals in the final classification and tend to have a negative impact on the results.

In contrast, the optical FORMOSAT-2 image does not need such

sophisticated preprocessing; it was co-registered to the orthorectified TerraSAR-X Spotlight images and thereby benefits from their high spatial accuracy. The RMSE (root mean square error) was 0.79 m, which is less than one pixel and allows a pixel-based combination of the image with the involved SAR images.

3.4.3 Supervised LULC Classification Using Remote Sensing Images

The training part of the ground reference data was used to carry out a supervised classification, during which a classifier assigns each pixel location to a certain land use class. The two different classifiers used in this study are the Maximum Likelihood classifier, in combination with a newly-developed optimization approach, further described in Section 3.4.4. The second is the Random Forest classifier, described in Section 3.4.5.

The different land use classes for forest and urban were not of interest for this study, and based on visual examination, it was clear that none of the remote sensing images would be able to discriminate between those classes. Consequently, after the classification, the deciduous and coniferous forest classes were merged into forest, while concrete was dissolved in urban.

The following validation process to quantify the accuracy of the LULC-classifications was based on independent ground reference. We chose OA as the most prominent measure of accuracy in this study. It is obtained by dividing all correctly classified pixels by all pixels that were used for validation (Congalton 1991; Congalton & Green 2008). Additionally, we calculated the confusion matrix (which allows more interpretation of the individual accuracy of the different land use classes) and the kappa-coefficient (κ), which illustrates accuracy compared to a random classification.

3.4.4 Maximum Likelihood Classification and Optimization

The supervised classification using the established Maximum Likelihood classifier was transformed to a python code using the scripting extension provided by ArcGIS. With this extension, it is possible to execute all software tools from a programming environment. Next, we implemented an innovative script logic to determine the raster band combination that results in the highest accuracy of the LULC classification, which likewise indicates that this band combination is suited best for the respective classification. Basically, the whole process was repetitively executed with stepwise addition of the input bands, until the highest accuracy was reached or all input bands were used. Figure 3.2 visually shows the workflow of the process. The script logic in pseudo-code is as follows:

1. Classify and validate all input raster bands individually.
2. Choose the one which results in the classification with the highest accuracy.
3. Combine this/these band(s) of the final stack successively with those bands that are not in the final stack. Add the band whose combination resulted in the highest accuracy-increase into the final stack.
4. Repeat step 3 until the accuracy does not increase any more or all bands are used.

In the end, this optimization process reveals those bands resulting in an increase of accuracy when added to the image stack of the classification. All other bands are neglected. Thereby, the optimum combination of input bands can be found, over-fitting is avoided, and erroneous information is dislodged. Furthermore, all input features are evaluated, whether they are able to increase the classification accuracy or not, which expresses the usefulness of this feature for the classification.

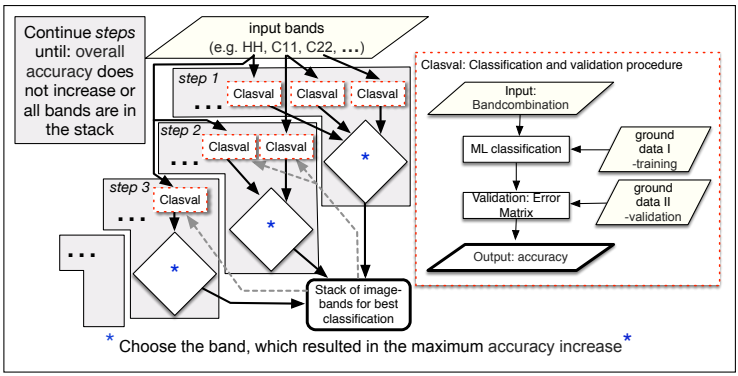

Figure 3.2: Workflow to optimize the Maximum Likelihood classification and find the input features resulting in the highest classification accuracy. In the example above, band C22 is the band which results in the highest accuracy in step1, and is therefore kept in the final image stack. In step2, the bands HH and C11 would each be combined with the C22, classified, and validated. In the example, it is assumed that the combination with C11 results in a higher accuracy of the classification and is therefore put in the final stack. In step3, only the HH band has not been used, and the classification and validation process is only done to evaluate if the classification accuracy increases, which would also mean that HH is kept in the final stack. The "..." indicate that the procedure can also be used to find the best band of more than three input bands.

3.4.5 Random Forest Classification

The second classifier implemented in this study is the RF classification algorithm, introduced by Breiman (2001) and adopted for the classification of remote sensing images by Pal (2005). RF is a ensemble learning technique, and builds upon multiple decision trees.

Each decision tree is built using a subset of the original training data and is evaluated by the remaining part of training features. New objects are classified as the class that is predicted by the most trees. According to Rodriguez-Galiano et al. (2012), the classifier has three main advantages for LULC classifications from remote sensing images: (i) It reaches higher accuracies than other machine learning classifiers; (ii) It has the ability to measure the importance level of the input images; (iii) It does not make any assumptions about the distributions assumptions of the input images. Therefore, RF classifications have been successfully applied to crop classification scenarios using remote sensing images, optical (Reynolds et al. 2016), and radar (Zhao et al. 2014; Sonobe et al. 2014). Ok et al. (2012) concluded an accuracy increase using the RF classifier over the Maximum Likelihood classifier of about eight percent to classify crops using one Spot5 satellite image.

3.5 Results

As described before, the input datasets were divided into spatial subsets. One consists of the scenes with a high resolution and the cloud-free part of the optical image. This area has a smaller extent of about 5 × 10 km. The resulting 31 combinations were each classified using the proposed optimized Maximum Likelihood approach and the RF classifier. An overview of those results is given in Figure 3.3, whereas individual classifications are presented in Figures 3.4, 3.5, and 3.6. The second spatial subset consists of the five stripmap images of TerraSAR-X, the two Radarsat2 scenes, and the Envisat ASAR image. The 15 meaningful combinations of this subset were also each classified with both classifiers; results are shown in Figure 3.7. Additionally, the processing time of each of the 92 classifications is stated.

As an illustration, Figure 3.4 shows the result of the the combination of the four TerraSAR-X Spotlight images (datasets 1–4, Table 3.2), which results in an accuracy as high as 93%. By adding the optical FORMOSAT-2 image, it was possible to reach a higher accuracy of

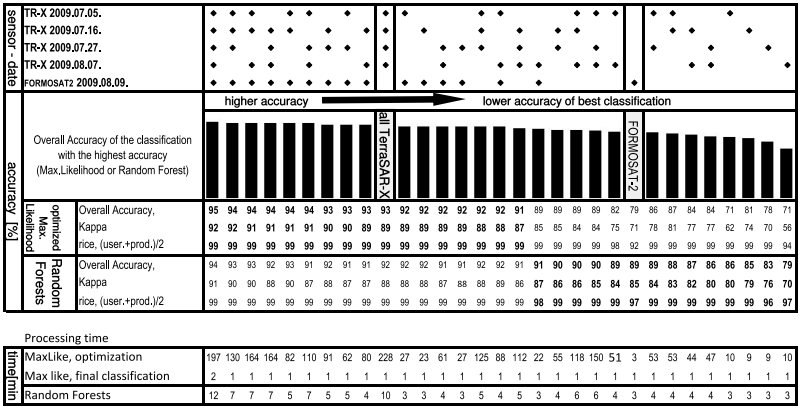

Figure 3.3: Comparison of the classifications of the smaller extent. Bold numbers indicate a higher accuracy.

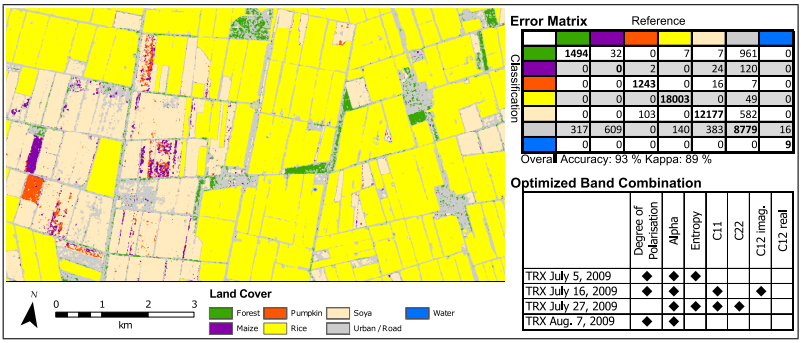

Figure 3.4: Optimized Maximum Likelihood Classification from all radar data covering the smaller subset (datasets no. 1–4, Table 3.2).

95%—the highest accuracy of the study—which is shown in Figure 3.5. When only two or three radar images are used, the accuracy declines. Notably, one Spotlight TerraSAR-X Radar acquisition alone still enables the determination of the rice cultivation area with minimum 97% when using Random Forest, and 94% with the Maximum Likelihood classifier. However, if two TerraSAR-X Spotlight acquisitions are combined, the OA reaches at least 86% (Random Forest). Especially of note, the rice accuracy becomes ideal (>99%). The rice accuracy of the classification of the optical image alone reaches 97%, whereas the accuracy of this classification is slightly higher than the classifications of each single radar acquisition. Interestingly, any combination of radar and optical images results in substantially increased accuracy indices. Nevertheless, the best combination of one single radar image (5 July 2009) and the optical FORMOSAT-2 image reaches an accuracy of 92% (κ-index of 0.89%), regardless of the classifier used, and is the one where the timespan between the acquisitions is longest. This result is shown in Figure 3.6. This smaller subset also demonstrates the benefit of the Optimization approach. On the one hand, once the optimum features are selected, the runtime is considerably reduced; on the other hand, an analysis of all selected features is possible, as shown in Table 3.3.

In comparison to the high accuracy values of the small subset, the classifications of the wider area exhibit lower classification accuracy. As can be seen, the area at the eastern end of the farm was classified with lower accuracy, as it was obtained from the Envisat image alone. Fortunately, only for about 8 km^2 of the farm is this the only available source. Westwards, successively adding the two Radarsat-2 scenes increases the OA and the accuracy of the rice class to 89% (85% for Random Forest) after adding the first, and 0.96% (Random Forest and Maximum Likelihood) after also adding the second one. Notably, the combination of the two c-band images that are only one day apart from each other (datasets 10 and 12, Table 3.2) is the worst combination of the study. The two Radarsat-2 scenes are from different angles, and when classified alone, their accuracy is slightly higher than the one obtained from the five TerraSAR-X stripmap images (datasets

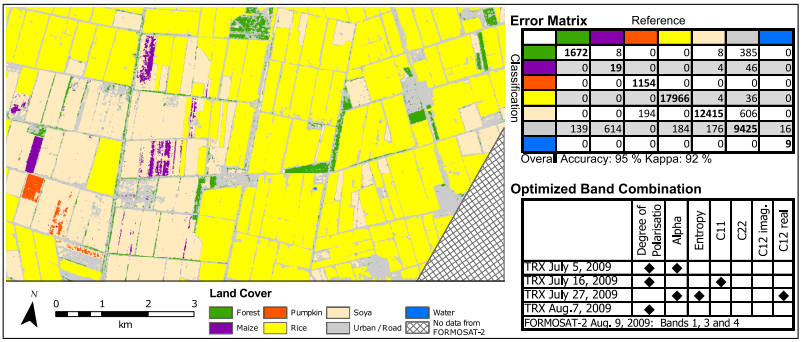

Figure 3.5: Optimized Maximum Likelihood Classification from all data covering the smaller subset (datasets no. 1–4 and 13, Table 3.2).

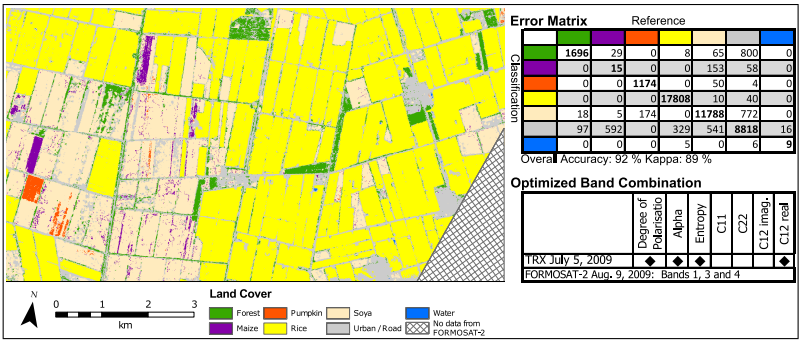

Figure 3.6: Best combination of one single radar acquisition (TerraSAR-X July 5) with the optical FORMOSAT2 image over the smaller area (datasets no. 1 and 13, Table 3.2). Classified using the Optimized Maximum Likelihood approach.

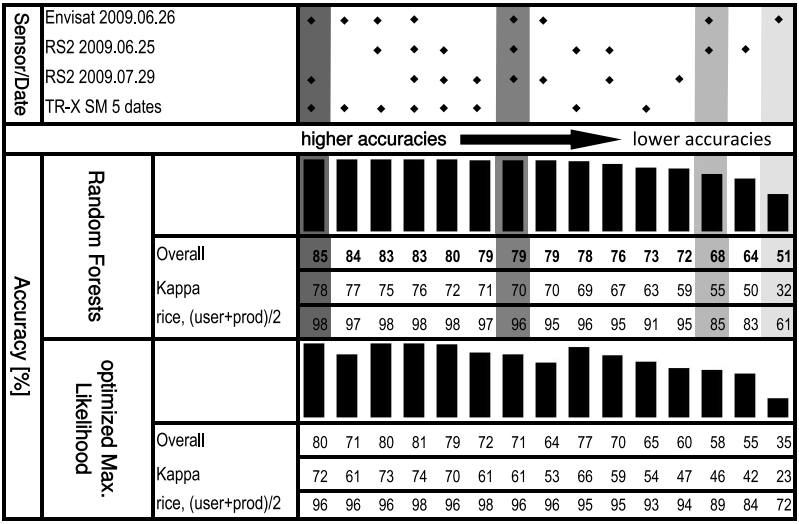

Processing time:

Time [min]																
Max. Likelihood	Optimization	173	41	174	307	245	106	132	52	116	98	21	27	49	24	8
	Final classification	3	2	3	3	2	2	2	1	2	1	1	1	1	1	2
Random Forests		124	59	92	162	136	43	115	78	75	97	45	81	60	70	185

Figure 3.7: Accuracy comparison of the classifications from acquisitions with a wider coverage; colours of the rows are the same as in Figure 3.8 and indicate usage of the combination for the creation of the final land use map.

5–9, Table 3.2), which all have the same viewing geometry but only VV-polarization. In contrast, all combinations of the x-band time series with each c-band image yields a considerably higher accuracy. However, the best combination of images reaches 85% accuracy, which is still lower than the 89% that was obtained from the optical image. When it comes to the accuracy of the rice class, the combination is just able to outperform the optical image (98% vs. 97%). This radar combination covers 80% of the Qixing farm, which equals about 872 km^2, and the major parts of Figure 3.8 contain this classification.

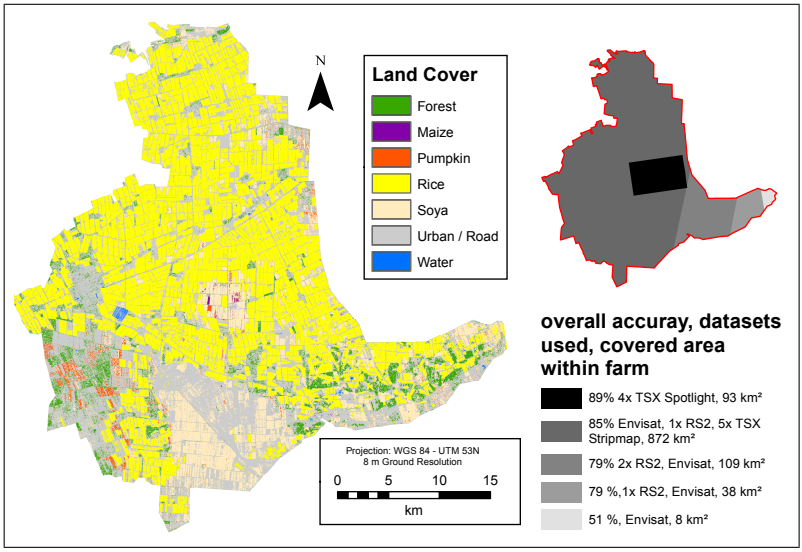

Figure 3.8: Combination of the best classifications from all microwave images involved in this study to classify the whole area of the farm with the best possible accuracy.

Feature	Times Chosen for the Final Stack
Alpha angle	56
Degree of Polarisation	45
Entropy	34
C12r	34
C11	24
C12i	20
C22	17

Table 3.3: Importance of input features for the smaller subset, following the Maximum Likelihood optimization; the maximum possible value is 64.

3.6 Discussion

Both the developed optimized Maximum Likelihood classification and the Random Forest classifier work well for LULC and crop analysis based on multitemporal, multisensor, and multi-polarization SAR satellite images. The analysis of four TerraSAR-X Spotlight images results in an accuracy of 93% and 92% for Maximum Likelihood and Random Forest, respectively, and of up to 99% for the rice crop class. The combined analysis of those four images with an optical FORMOSAT-2 image slightly improved the classification to a maximum of 95% OA (rice accuracy: 99%). Additionally, the monotemporal analysis of the four TerraSAR-X Spotlight acquisitions are each able to determine the area of rice with a very high accuracy of at least 94%. This is not a new discovery, and is a consequence of the special interaction of microwaves with inundated rice fields (Koppe et al. 2013; Inoue et al. 2002). By making use of this interaction, rice fields can be separated from the other land use classes with high accuracy (Chakraborty et al. 1997; Miyaoka et al. 2013; Brisco et al. 2013). Another known fact that can be justified by this study is that only multi-temporal radar acquisitions are adequate to dissolve different crops (Bush & Ulaby 1978; Hoogeboom 1983).

Bush & Ulaby (1978) also used dual polarimetric SAR data and recommended four target revisits at an interval of ten days to get 90% accuracy. We can almost exactly conclude the same from our study, as the four TerraSAR-X acquisitions—which are 11 days apart from each other—resulted in accuracy of 93% and 92%, depending on the classifier. This is also in accordance with the more recent study of Bargiel & Herrmann (2011), who reached about 90% accuracy using 14 TerraSAR-X images to separate different crops in two regions. However, in this study, the only way to further increase such high accuracies was the combination with the optical FORMOSAT-2 image, which delivered an accuracy of up to 95%. This justifies the studies of Blaes et al. (2005) and Forkuor et al. (2014). Notably, our study additionally quantifies the benefit of the optical image: Its availability substitutes about two TerraSAR-X Spotlight images, as combinations of two radar images and the optical image deliver accuracies about as high as the four radar images combined.

These results of the small subset show how the developed approach is well-suited to reproduce and validate existing knowledge and quantify accuracy improvements from added remote sensing datasets. In the same way, Figure 3.7 shows accuracy for the wider area, which is influenced by different aspects. Again, accuracy generally increases when more data is added. Additionally, we demonstrated the beneficial use of combined x- and c-band radar images for crop classification, which has been shown before McNairn et al. (2014). The wider area is also a good test-bed for the comparison of the two classifiers used in the study. The Random Forest classifier seems to be much more effective in data-poor situations; the worst classification from the single Envisat image alone is the extreme example—it has a 16% higher OA using Random Forest than the same classification using Maximum Likelihood. Interestingly, in data intensive environments of the study, the proposed optimization of the Maximum Likelihood is able to very slightly outperform the Random Forest classifier. Analysis of the processing time reveals the potential of the Maximum Likelihood classifier to be carried out much faster, once the optimal band combination is determined.

Although our findings offer some insights on crop classification using diverse SAR satellite images, the limitations of the study design and outcomes should be recognized. First of all, the crop types presented in this study are limited. It would be interesting to investigate the potential to classify other crops with even more diverse SAR images. Those could also be extended to fully polarimetric images, which offer much more possibilities to derive polarimetric features. Qi et al. (2012), for instance, derived as many as 80 different features from two fully polarimetric Radarsat-2 acquisitions for their pixel-based approach. Furthermore, Souyris et al. (2005) quantified the increase of accuracy from fully polarimetric versus dual polarimetric L-band images. Another issue with our study is that more possible SAR satellites and more SAR acquisition modes were not incorporated. Data from the L-band SAR sensor PalSAR onboard the ALOS satellite would extend our analysis to another wavelength, with an evaluation of its already-demonstrated crop classification potential (McNairn, Shang, et al. 2009) and the possibility to study the synergistic effects of l-, c- and x-band SAR data.

Another key point, especially for the small and more data-intense subset, is the question of whether or not that many radar datasets at such a high resolution are necessary. For instance, we described above that the accuracy of the rice class is always higher from SAR images. Notably, every high-resolution acquisition alone or any combination of two radar images is sufficient to differentiate the area of rice. Only when other classes are relevant and a high OA is needed, do more radar acquisitions actually make sense. The accuracy of the classification of the whole farm distinguishes the area of rice with more than 98% accuracy for 80% of the area of the farm, and the accuracy reaches 85 %. According to Anderson et al. (1976), this is suitable for application.

3.7 Conclusions

In this study, we determined LULC of a rice farm in north-eastern China. The main objective was to fill the information gap of detailed crop classes within the arable land use class using a combination of multitemporal, multisensor, and multi-polarisation microwave satellite acquisitions. Forty-six different combinations of acquisitions were evaluated, and their accuracy quantified. A supervised classification was carried out using two different classifiers. The state-of-the-art Random Forest classifier and the well-established Maximum Likelihood classifier, which was optimized using an innovative script to find the optimum input bands. Finally, the classifications were merged to reach an optimized classification of the whole farm with the best accuracy possible. This final classification covers more than 1000 km^2, in a spatial resolution as high as 8 m. Most of the area of the farm was classified with more than 85% accuracy, while the accuracy of the land cover class rice (which is the most important one) was almost perfect.

The results of the study concur with various studies on SAR-based crop classification. Furthermore, the potential of microwave and optical images to differentiate the area of rice is demonstrated and quantified on a regional scale with very high spatial resolution. It is shown that microwave and optical remote sensing is eminently suitable to discriminate the area of rice with high spatial resolution.

Data from c-band radar satellites such as Sentinel-1, Radarsat-2, and the future Radarsat constellation combined with operational x-band satellites such as TerraSAR-X, TanDEM-X, and PAZ make the presented approach ideal for even more data-intense study sites and years in the future. It is well suited to be adopted for other LULC crop distribution studies on regional scales. As the Maximum Likelihood optimization script is freely downloadable, all that is needed is therefore a ground truth set of crop distribution of the respective year and remote sensing images. The possibility to integrate multiple acquisitions from different sensors and automatically find the ideal combination of bands for land use classification is an important

improvement for future LULC mapping from satellite remote sensing observations.

3.8 Acknowledgments

This study was financially supported by National Basic Research Program (973-2015CB150405), International Bureau of the German Federal Ministry of Research and Technology BMBF (Project number CHN 08/051), Airbus Defence and Space, the GIS and RS group of the University of Cologne, the International Center for Agro-Informatics and Sustainable Development (ICASD), and the Sino-Norwegian Cooperative SINOGRAIN project (CHN-2152, 14-0039). Envisat ASAR Data were provided by the European Space Agency under proposal No. 16975 "Rice Monitoring China, Jiansanjiang".

3.9 References

Alberga, V., Satalino, G., Staykova, D., 2008. Comparison of polarimetric SAR observables in terms of classification performance. International Journal of Remote Sensing 29(14), 4129–4150.

Anderson, J., Hardy, E., Roach, J., Witmer, R., 1976. A land use and land cover classification system for use with remote sensor data. United States Government Printing Office, Washington D.C., USA.

Atzberger, C., 2013. Advances in remote sensing of agriculture: Context description, existing operational monitoring systems and major information needs. Remote Sensing 5(2), 949–981.

Bargiel, D., Herrmann, S., 2011. Multi-Temporal Land-Cover Classification of Agricultural Areas in Two European Regions with High Resolution Spotlight TerraSAR-X Data. Remote Sensing 3(12), 859–877. issn: 2072-4292.

Blaes, X., Vanhalle, L., Defourny, P., 2005. Efficiency of crop identification based on optical and SAR image time series. Remote Sensing of Environment 96(3-4), 352–365.

Breiman, L., 2001. Random forests. Machine learning 45(1), 5–32.

Breit, H., Fritz, T., Balss, U., Lachaise, M., Niedermeier, A., Vonavka, M., 2010. TerraSAR-X SAR processing and products. Geoscience and Remote Sensing, IEEE Transactions on 48(2), 727–740.

Brisco, B., Li, K., Tedford, B., Charbonneau, F., Yun, S., Murnaghan, K., 2013. Compact polarimetry assessment for rice and wetland mapping. International Journal of Remote Sensing 34(6), 1949–1964.

Bryan, L. M., 1983. Urban land use classification using synthetic aperture radar. International Journal of Remote Sensing 4(2), 215–233.

Bush, T., Ulaby, F., 1978. An evaluation of radar as a crop classifier. Remote Sensing of Environment 7(1), 15–36.

Chakraborty, M., Panigrahy, S., Sharma, S. A., 1997. Discrimination of rice crop grown under different cultural practices using temporal ERS-1 synthetic aperture radar data. ISPRS Journal of Photogrammetry and Remote Sensing 52(4), 183–191.

Chen, J., Chen, J., Liao, A., Cao, X., Chen, L., Chen, X., He, C., Han, G., Peng, S., Lu, M., Zhang, W., Tong, X., Mills, J., 2015. Global land cover mapping at 30 m resolution: A POK-based operational approach. ISPRS Journal of Photogrammetry and Remote Sensing 103, 7–27.

Cloude, S. R., Goodenough, D. G., Chen, H., 2012. Compact decomposition theory. IEEE Geoscience and Remote Sensing Letters 9(1), 28–32.

Cloude, S. R., Pottier, E., 1996. A review of target decomposition theorems in radar polarimetry. IEEE Transactions on Geoscience and Remote Sensing 34, 498–518.

Congalton, R. G. R., 1991. A review of assessing the accuracy of classifications of remotely sensed data. Remote sensing of environment 37(October 1990), 35–46.

Congalton, R. G., Green, K., 2008. Assessing the accuracy of remotely sensed data: principles and practices. CRC press, Taylor & Francis, Boca Raton, Florida, USA.

Curlander, J., McDonough, R., 1991a. Synthetic Aperture Radar: Systems and Signal Processing. JohnWiley& Sons, New York, USA.

Dobson, M. C., Ulaby, F. T., Pierce, L. E., 1995. Land-cover classification and estimation of terrain attributes using synthetic aperture radar. Remote Sensing of Environment 51(1), 199–214.

Doornbos, E., Scharroo, R., Klinkrad, H., Zandbergen, R., Fritsche, B., 2002. Improved modelling of surface forces in the orbit determination of ERS and ENVISAT. Canadian Journal of Remote Sensing 28, 535–543.

Foody, G. M., 2002. Status of land cover classification accuracy assessment. Remote Sensing of Environment 80(1), 185–201.

Forkuor, G., Conrad, C., Thiel, M., Ullmann, T., Zoungrana, E., 2014. Integration of optical and Synthetic Aperture Radar Imagery for Improving Crop Mapping in Northwestern Benin, West Africa. Remote Sensing 6(7), 6472–6499.

Gnyp, M. L., Miao, Y., Yuan, F., Ustin, S. L., Yu, K., Yao, Y., Huang, S., Bareth, G., 2014. Hyperspectral canopy sensing of paddy rice aboveground biomass at different growth stages. Field Crops Research 155, 42–55.

Gomez-Chova, L., Tuia, D., Moser, G., Camps-Valls, G., 2015. Multimodal Classification of Remote Sensing Images: A Review and Future Directions. Proceedings of the IEEE 103(9), 1560–1584.

Green, K., Kempka, D., Lackey, L., 1994. Using remote sensing to detect and monitor land-cover and land-use change. Photogrammetric Engineering & Remote Sensing 60(3), 331–337.

Hoogeboom, P., 1983. Classification of Agricultural Crops in Radar Images. IEEE Transactions on Geoscience and Remote Sensing GE-21(3), 329–336. ISSN: 0196-2892.

Horning, N., 2013. *RandomForestClassification*. https://www.bitbucket.org/rsbiodiv/randomforestclassification/commits/534bc2f, 2019-1-5.

Immitzer, M., Vuolo, F., Atzberger, C., 2016. First experience with Sentinel-2 data for crop and tree species classifications in central Europe. Remote Sensing 8(3, 166), 1–27.

Inoue, Y., Kurosu, T., Maeno, H., Uratsuka, S., Kozu, T., Dabrowska-Zielinska, K., Qi, J., 2002. Season-long daily measurements of multifrequency (Ka, Ku, X, C, and L) and full-polarization backscatter signatures over paddy rice field and their relationship with biological variables. Remote Sensing of Environment 81(2-3), 194–204.

Jarvis, A., Reuter, H. I., Nelson, A., Guevara, E., 2008. Hole-filled SRTM for the globe Version 4, available from the CGIAR-CSI SRTM 90m Database. http://srtm.csi.cgiar.org, 2018-10-22.

Koppe, W., Gnyp, M. L., Hütt, C., Yao, Y., Miao, Y., Chen, X., Bareth, G., 2013. Rice monitoring with multi-temporal and dual-polarimetric terrasar-X data. International Journal of Applied Earth Observation and Geoinformation 21(1), 568–576.

Lenz-Wiedemann, V. I. S., Klar, C. W., Schneider, K., 2010. Development and test of a crop growth model for application within a Global Change decision support system. Ecological Modelling 221, 314–329.

Liaw, A., Wiener, M., 2002. Classification and Regression by randomForest. R News 2(3), 18–22.

Lo, C. P., Fung, T., 1986. Production of land-use and land-cover maps of central Guangdong Province of China from LANDSAT MSS imagery†. International Journal of Remote Sensing 7(8), 1051–1074.

McNairn, H., Kross, A., Lapen, D., Caves, R., Shang, J., 2014. Early season monitoring of corn and soybeans with TerraSAR-X and RADARSAT-2. International Journal of Applied Earth Observation and Geoinformation 28, 252–259.

McNairn, H., Champagne, C., Shang, J., Holmstrom, D., Reichert, G., 2009. Integration of optical and Synthetic Aperture Radar (SAR) imagery for delivering operational annual crop inventories. ISPRS Journal of Photogrammetry and Remote Sensing 64, 434–449.

McNairn, H., Shang, J., Jiao, X., Champagne, C., 2009. The contribution of ALOS PALSAR multipolarization and polarimetric data to crop classification. IEEE Transactions on Geoscience and Remote Sensing 47(12), 3981–3992.

Miyaoka, K., Maki, M., Susaki, J., Homma, K., Noda, K., Oki, K., 2013. Rice-Planted Area Mapping Using Small Sets of Multi-Temporal SAR Data. IEEE Geoscience and Remote Sensing Letters 10(6), 1507–1511.

Morena, L. C., James, K. V., Beck, J., 2004. An introduction to the RADARSAT-2 mission. Canadian Journal of Remote Sensing 30, 221–234.

Nonaka, T., Ishizuka, Y., Yamane, N., Shibayama, T., Takagishi, S., Sasagawa, T., 2008. Evaluation of the geometric accuracy of TerraSAR-X. International Archives of the Photogrammetry, 135–140.

Ok, A. O., Akar, O., Gungor, O., 2012. Evaluation of random forest method for agricultural crop classification. European Journal of Remote Sensing 45(3), 421.

Pal, M., 2005. Random forest classifier for remote sensing classification. International Journal of Remote Sensing 26(1), 217–222.

Pinter Jr, P. J., Hatfield, J. L., Schepers, J. S., Barnes, E. M., Moran, M. S., Daughtry, C. S., Upchurch, D. R., 2003. Remote sensing for crop management. Photogrammetric Engineering & Remote Sensing 69(6), 647–664.

Prats-Iraola, P., Scheiber, R., Rodriguez-Cassola, M., Wollstadt, S., Mittermayer, J., Bräutigam, B., Schwerdt, M., Reigber, A., Moreira, A., 2012. High precision SAR focusing of TerraSAR-X experimental staring spotlight data. Geoscience and Remote Sensing Symposium (IGARSS), 2012 IEEE International, IEEE, 3576–3579.

Qi, Z., Yeh, A. G.-O., Li, X., Lin, Z., 2012. A novel algorithm for land use and land cover classification using RADARSAT-2 polarimetric SAR data. Remote Sensing of Environment 118, 21–39.

R Core Team, 2016. *R: A Language and Environment for Statistical Computing*. R Foundation for Statistical Computing. Vienna, Austria. http://www.R-project.org/,

Raney, R. K., Hopkins, J., 2011. A Perspective on compact Polarimetry. IEEE Geoscience and Remote Sensing Society Newsletter, 12–18.

Reynolds, J., Wesson, K., Desbiez, A. L., Ochoa-Quintero, J. M., Leimgruber, P., 2016. Using Remote Sensing and Random Forest to Assess the Conservation Status of Critical Cerrado Habitats in Mato Grosso do Sul, Brazil. Land 5(2), 12.

Ribbes, F., 2010. Rice field mapping and monitoring with RADARSAT data. International Journal of Remote Sensing 20(4), 745–765. issn: 0143-1161.

Rodriguez-Galiano, V. F., Ghimire, B., Rogan, J., Chica-Olmo, M., Rigol-Sanchez, J. P., 2012. An assessment of the effectiveness of a random forest classifier for land-cover classification. ISPRS Journal of Photogrammetry and Remote Sensing 67, 93–104.

Rodriguez, E., Morris, C., Belz, J., 2006. A global assessment of the SRTM performance. Photogrammetric Engineering & Remote Sensing 72, 249–260.

Schmedtmann, J., Campagnolo, M. L., 2015. Reliable Crop Identification with Satellite Imagery in the Context of Common Agriculture Policy Subsidy Control. Remote Sensing 7(7), 9325–9346.

Solberg, A. H. S., Jain, A. K., Taxt, T., 1994. Multisource classification of remotely sensed data: fusion of Landsat TM and SAR images. Geoscience and Remote Sensing, IEEE Transactions on 32(4), 768–778.

Sonobe, R., Tani, H., Wang, X., Kobayashi, N., Shimamura, H., 2014. Random forest classification of crop type using multi-temporal TerraSAR-X dual-polarimetric data. Remote Sensing Letters 5(2), 157–164.

Souyris, J.-C., Imbo, P., Fjortoft, R., Mingot, S., Lee, J.-S., 2005. Compact polarimetry based on symmetry properties of geophysical media: The $\pi/4$ mode. IEEE Transactions on Geoscience and Remote Sensing 43(3), 634–646.

Tennakoon, S. B., Murty, V. V. N., Eiumnoh, a., 1992. Estimation of cropped area and grain yield of rice using remote sensing data. International Journal of Remote Sensing 13(3), 427–439.

Vibhute, A. D., Gawali, B. W., 2013. Analysis and modeling of agricultural land use using remote sensing and geographic information system: A review. International Journal of Engineering Research and Applications (IJERA) 3(3), 81–91.

Waldhoff, G., Curdt, C., Hoffmeister, D., Bareth, G., 2012. Analysis of multitemporal and multisensor remote sensing data for crop rotation mapping. ISPRS International Archives of the Photogrammetry, Remote Sensing and Spatial Information Sciences, I-7, 177–182.

Wu, F., Wang, C., Zhang, H., Zhang, B., Tang, Y., 2011. Rice crop monitoring in South China with RADARSAT-2 quad-polarization SAR data. IEEE Geoscience and Remote Sensing Letters 8, 196–200.

Zhao, L., Yang, J., Li, P., Zhang, L., 2014. Characteristics analysis and classification of crop harvest patterns by exploiting high-frequency multipolarization SAR data. Selected Topics in Applied Earth Observations and Remote Sensing, IEEE Journal of 7(9), 3773–3783.

Zhao, Q., Hütt, C., Lenz-Wiedemann, V. I. S., Miao, Y., Yuan, F., Zhang, F., Bareth, G., 2015. Georeferencing Multi-source Geospatial Data Using Multi-temporal TerraSAR-X Imagery: a Case Study in Qixing Farm, Northeast China. Photogrammetrie - Fernerkundung - Geoinformation 2015(2), 173–185.

Zhao, S., 1986. Physical Geography of China. John Wiley & Sons, Science Press, Beijing, China and New York, USA.

4 Georeferencing Multi-source Geospatial Data Using Multi-temporal TerraSAR-X Imagery: a Case Study in Qixing Farm, Northeast China

Quanying Zhao[1], Christoph Hütt[1], Victoria I. S. Lenz-Wiedemann[1], Yuxin Miao[2], Fei Yuan[3], Fusuo Zhang[4], Georg Bareth[1]

Published in: Photogrammetrie, Fernerkundung, Geoinformation (PFG), 2015 / 2, 173-185.
Original manuscript is embedded in dissertation format.

1. International Center for Agro- Informatics and Sustainable Development (ICASD), Institute of Geography, GIS & Remote Sensing Group, University of Cologne, 50923 Cologne, Germany,
e-mail: zhaoquanying@gmail.com, {christoph.huett} {victoria.lenz} {g.bareth}@uni-koeln.de

2. ICASD, College of Resources and Environmental Sciences, China Agricultural University, Beijing China, 100193 Beijing,
e-mail: ymiao@cau.edu.cn

3. ICASD, Department of Geography, Minnesota State University, Minnesota, MN 56001, USA,
e-mail: fei.yuan@mnsu.edu

4. College of Resources and Environmental Sciences, China Agricultural University, Beijing China, 100193 Beijing,
e-mail: zhangfs@cau.edu.cn

4.1 Summary

Geodata, including optical remote sensing images and topographic vector data, can be collected from multiple sources such as surveying and mapping agencies, commercial data acquisition companies, and local research institutes. These multi-source data have been widely used in past remote sensing and GIS studies in various applications. However, spatial inconsistencies inherent in the multi-source data require accurate georeferencing to be applied. This is challenging for study sites with limited accessibility and few reference maps. To address this challenge, this paper proposes an approach for generating Ground Control Points (GCPs) using TerraSAR-X data. In a case study, TerraSAR-X images were used to georeference multi-source data covering the Qixing Farm in Northeast China. First, a stack of five multi-temporal TerraSAR-X images were processed into one reference image to retrieve GCPs. These were then used to georeference the other datasets including Huanjing-, Landsat-5, FORMOSAT-2, and RapidEye satellite images, as well as topographic vector datasets. Identifying tie points in the multi-source datasets and the corresponding GCPs in the TerraSAR-X reference image enables georeferencing without field measurements. Finally the georeferencing accuracies for the optical remote sensing images were assessed by using independent check points. Good results were obtained for the Huanjing, Landsat-5, FORMOSAT-2 and RapidEye images, with an absolute error of 7.15m, 6.97m, 8.94m and 10.52m, respectively. For the topographic vector datasets, ideal visual results were achieved, attributable to

the rubber sheeting algorithm. These results demonstrate that the TerraSAR-X reference image is suitable for georeferencing multi-source data accurately and cost-efficiently. The developed procedure can be applied in other study regions and is especially valuable for data-poor environments.

4.2 Zusammenfassung

Zusammenfassung: Georeferenzierung von Raster und Vektordaten aus unterschiedlichen Quellen mit Hilfe von multitemporalen TerraSAR-X Aufnahmen – eine Fallstudie der Qixing-Farm im Nordosten Chinas. Für räumliche Analysen kommen Geodaten wie Fernerkundungsdaten und topographische Vektordaten zum Einsatz, die von diversen Einrichtungen, u.a. Vermessungsämtern, kommerziellen Geoinformations-Dienstleistern und Forschungsinstituten bereitgestellt bzw. bezogen werden. Diese aus unterschiedlichen Quellen stammenden Daten (Multidaten) werden für zahlreiche Anwendungen in Fernerkundungs- und GISStudien genutzt. Jedoch beinhalten diese Daten räumliche Ungenauigkeiten, die zunächst eine präzise Georeferenzierung erforderlich machen. Dieses stellt vor allem für Untersuchungsgebiete mit eingeschränkter Zugänglichkeit und nicht verfügbaren Referenzdaten eine Herausforderung dar. Dieser Artikel erklärt, wie Passpunkte aus Daten des Radarsatelliten TerraSAR-X für die Georeferenzierung von Multidaten generiert werden können. In einer Fallstudie der Qixing-Farm im Nordosten Chinas wurden fünf multitemporale TerraSAR-X-Radarbilder zu einem Referenzbild zusammengefügt, um mit hoher Genauigkeit Passpunkte abzuleiten. Diese Passpunkte dienen der Georeferenzierung mehrerer Multidaten aus diversen Quellen, welche sowohl Huanjing-, Landsat-5-, FORMOSAT-2-, und RapidEye-Satellitenbilder als auch topographische Vektordaten umfassen. Die Identifizierung derselben Passpunkte in dem TerraSAR-X-Referenzbild und in den Multidaten diverser Quellen ermöglicht eine genaue Georeferenzierung ohne im Gelände aufgenommene Messdaten. Die Genauigkeit der Georeferenzierung für die optischen Satellitenbil-

der wurde durch unabhängige Kontrollpunkte bewertet. Es wurden gute Ergebnisse für die Huanjing-, Landsat-5-, FORMOSAT-2 und RapidEye-Satellitenbilder mit absoluten Fehlern von 7,15 m, 6,97 m, 8,94 m bzw. 10,52 m erzielt. Für die Georeferenzierung der topographischen Vektordaten wurden optimale visuelle Resultate erzielt, welches dem eingesetzten „Rubber Sheeting Algorithm“ zuzuschreiben ist. Diese Ergebnisse demonstrieren die Eignung der aus TerraSAR-X-Daten abgeleiteten Passpunkte, um Multidaten verschiedener Quellen genau und kosteneffizient zu georeferenzieren. Das entwickelte Verfahren kann auf andere Untersuchungsregionen übertragen werden und ist besonders wertvoll für Gegenden mit schlechter Verfügbarkeit von Referenzdaten.

4.3 Introduction

Data quality plays a critical role in geodata related research (Bareth 2009). To ensure data quality, georeferencing becomes a mandatory and crucial task. In this paper, datasets from different sources, each characterized by their unique attributes and properties, are referred to as multi-source data. Compared to single-source data, multi-source data can provide adequate information with different spatial and temporal resolutions, map scales, and spectral properties (Li 2010; Waldhoff et al. 2012). Multi-source data provided by various governmental bureaus or non-governmental organizations such as local research institutions or special research groups may vary in many interpretation aspects and in terms of (spatial) data quality. Both geographic information system (GIS) and remote sensing (RS) data carry plenty of geospatial information but with different nature and content and with different semantics (Weis et al. 2005). The integration of remote sensing and GIS is emerging as a new research field (Zhang 2010). Gómez-Candón et al. (2012) indicated that the locational errors in high resolution images, e.g. GeoEye-1 images, affect the delineation of the input prescription map which is a core problem for the implementation of site-specific agricultural management strategies.

Weber et al. (2008) confirmed that coregistration errors between imagery and field sites led to remarkable errors in landscape classification, particularly when the size of the target site was similar to the image pixel size. Moreover, in some cases, such as in China, detailed topographic data (1:5,000 - 1:25,000) with high spatial accuracy may not be accessible due to data sharing and management policies or lack of surveying and mapping activities (Bareth & Yu 2004). Because of heterogeneous qualities, the integration and georeferencing processes for multi-source data are indispensable, complex and highly dependent on the purpose of the study. A variety of methods for multi-source data integration and georeferencing have been developed in the past decades to eliminate spatial inconsistencies in multi-source datasets. For example, a Markov random field model was applied to merge images from multiple sensors for a land use (Solberg et al. 1996). A statistical approach to match relational features was introduced by Walter & Fritsch (1999). An iterative closest point algorithm was implemented to match features using a spatially precise map as the reference (Gösseln & Sester 2004). Empirical and theoretical methods were implemented by Usery et al. (2009) for integrating the national maps of the United States with different scales and resolutions in vector and raster datasets. In addition, several automatic approaches have been developed to compute the imagery-to-vector conversion (Wu et al. 2007), identify control point pairs from images using vector datasets as the glue layers (Chen, Knoblock, et al. 2006), conflate vector maps to high resolution imagery (Song et al. 2009), or georeference image sequences in real-time (Choi & Lee 2012).

In recent studies, SAR imagery has been used to quantify the spatial inconsistencies of geodata and to collect GCPs for georeferencing. SAR sensors are all-weather and day-night active microwave sensors that collect information of the targets according to the signal transport time between the sensor position and the terrain height. They have the potential to provide images with very high geometric accuracy (Ager & Bresnahan 2009; Rodriguez et al. 2006). In particular, the German TerraSAR-X satellite launched in 2007 is equipped with

a highly flexible phased array antenna for SAR Stripmap, ScanSAR, and Spotlight operations (Mittermayer & Runge 2003). An overall ground accuracy of less than 1m has been demonstrated when the images are projected to a precise terrain height (Ager & Bresnahan 2009; Koppe et al. 2010; Nonaka et al. 2008). Therefore, the TerraSAR-X products can be used to generate topographic maps and create accurate orthoimagery products (Badurska 2011; Reinartz et al. 2011; Schneider et al. 2009).

To further explore the potential capability of TerraSAR-X imagery as a source for locating GCPs and subsequently to georeference multisource data characterized by varying properties and accuracies over a large area, a feasible and robust method which takes the advantage of the high spatial resolution and high geometric accuracy of TerraSAR-X imagery is introduced. The main specific objectives are (i) to georeference topographic vector data from multiple sources; (ii) to improve the georeferencing results of Huanjing, Landsat-5, FORMOSAT-2, and RapidEye satellite images; and (iii) to assess the accuracy of georeferenced datasets and to evaluate if the results are highly dependent on the spatial accuracy of the TerraSAR-X imagery.

4.4 Study Area and Data

4.4.1 Study Area

The Sanjiang Plain, located in Northeast China, is an alluvial plain formed by the Songhua River, the Heilong River and the Wusuli River. The topography is fairly flat with a slope of $< 0.012\,°$. With an area of approximately 11 million ha, it is an important wetland area and ecosystem in China. Some wetland sites in this area have been designated for the list of wetlands of international importance (Wang et al. 2006). In addition, the Sanjiang Plain is the largest food base of China, where 52 national-owned farms are located. The climate is temperate sub-humid, with a mean annual precipitation of 500 mm - 600 mm (80 % of it occurring between May and September),

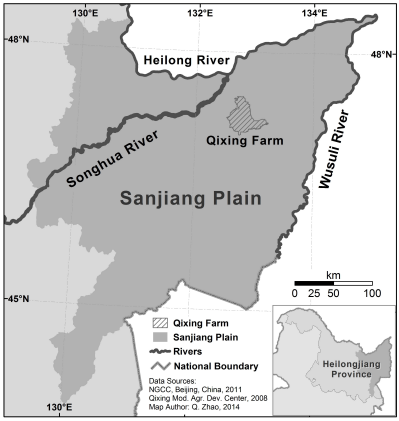

Figure 4.1: Location of the study area Qixing Farm in Northeast China.

and an average temperature of 21 °C - 22 °C in July and ≈18 °C in January. Nowadays, single season crops of paddy rice, soybean and maize are mainly planted in this area. The study site Qixing Farm (47.2 °N, 132.8 °E), which covers an area of approximately 120,000 ha, is located in the central part of the Sanjiang Plain (Figure 4.1). As of 2010, 62 % of the study site was arable, dominated by three quarters of paddy rice and one quarter of dryland (Zhang 2012). In the paddy rice fields, rainfed and irrigation systems simultaneously exist. To improve the growing conditions of agricultural crops, shelter forests were planted in the late 1980s, primarily to reduce the speed of ground wind (Liu & Zhao 1996).

4.4.2 Data Description

A time series of five TerraSAR-X images (stripmap, VV-polarisation, incidence angle ∼35°, relative orbit 88, descending) was taken within 44 days from June 24 to August 7 of 2009 (see Table 4.1). These

five stripmap images in the basic Single Look Slant Range Complex (SSC) form with intensity and phase information for each pixel in slant range geometry were used to create a TerraSAR-X reference image. The orbit precision was set to 'science', which means that the satellite position during image acquisition is calculated with an error of less than 20 cm in a post processing step (Fritz & Eineder 2013). This post processing dramatically increases the positional accuracy and thereby the image potential for generating GCPs (Koppe et al. 2010).

The Qixing Farm field boundary file was produced by the Qixing Modern Agriculture Development Center. This GIS layer was given in Universal Transverse Mercator (UTM) coordinate reference system, zone 53 N. It provides the information on crop field boundaries, irrigation wells, water drainages, and shelter forests edges at a fine field unit scale. However, this dataset did not line up with any of the other datasets in our project. The inconsistency was nonsystematic in distance or directions (Figure 4.3). An offset of more than 200 m between this dataset and the TerraSAR-X images was identified in the northwest part, whereas in the southeast part the shift was more than 300 m in the opposite direction.

The public version of the 1:250,000 topographic vector dataset was produced by the National Geomatics Center of China (NGCC). This dataset includes multiple layers of administration boundaries, settlements, railways, roads, hydrological information, and landscapes. However, as Bareth & Yu (2004) indicated, the spatial accuracy is not as high as expected. Therefore, a refined georeferencing of the public version is needed in this study.

The Huanjing, Landsat-5, FORMOSAT-2, and RapidEye satellite images were acquired from 2009 to 2012 in the growing season. The agricultural constructions, e.g. irrigation channels and raised ridges, for paddy rice in the study area are the same year by year and the field boundaries are mostly stable. Therefore, one TerraSAR-X reference image can be used in multiple years. The detailed information of the remote sensing data is listed in Table 4.1.

Satellite	Pixel Spacing (m)	Bands	Acquisition Date	Projection	Cloud Cover (%)	Processing Level
TerraSAR-X	1.89 (az) x 1.57 (rg)	-	June 24,July 5, 16, 27, Aug. 7, 2009	WGS 84 UTM 53 N	- -	SSC
Huanjing (CCD2)	30 x 30	4	June 29, 2012	WGS 84 UTM 53 N	0 (subset)	2
Landsat-5	30 x 30	7	Aug. 26, 2011	WGS 84 UTM 52 N	0 (subset)	1T
FORMOSAT-2	2 x 2 (PAN)	5	July 6, 2009	Geographic (Lat/Lon)	0	1A
RapidEye	5 x 5	5	May 19, 2012	WGS 84 UTM 53 N	0	3A

Table 4.1: Characteristics of the remote sensing images (az = azimuth, along track, rg = range, across track).

4.5 Methods

4.5.1 Workflow of Georeferencing Multi-source Datasets

The schematic workflow of multi-source data georeferencing is shown in Figure 4.2. There are mainly four steps involved: (1) pre-processing of the multi-temporal TerraSAR-X images to generate one single reference image; (2) selection of GCPs from the processed TerraSAR-X imagery and corresponding tie points from optical remote sensing images or topographic vector maps; (3) reducing locational errors by recursively reselecting GCPs and corresponding tie points until achieving low positional error (PE) values or satisfactory visual results; (4) generating georeferenced datasets by image resampling or GIS data matching. Steps 1 and 2 are the key steps of this approach, which highly affect the quality of the GCP interpretation and consequently the final results. We decided to use the PE because it is implemented in the software that we used and because the documentation of the individual error of every point proves best the efficiency of the proposed

method. The standard deviation (Std.) that characterizes the overall error is also given be as a comparison (Table 4.2).

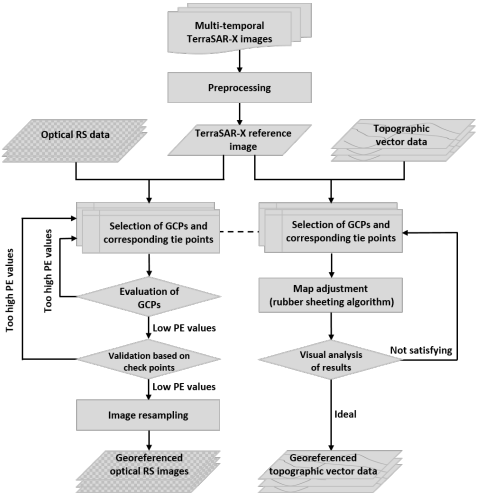

Figure 4.2: Georeferencing workflow of the multi-source geospatial data, PE = positional error.

4.5.2 Creation of the Reference Image from TerraSAR-X Stripmap Acquisitions

A stack of five TerraSAR-X stripmap images was used to create the reference image. Radar image processing was performed using the NEST distributed under the GNU General Public License. To meet the requirement of a geocoded image in which the precise outlines of objects are identifiable, certain pre-processing techniques were applied. First the 'complex pixel value 'were used to calculate an amplitude image representing the strength of radar backscatter for each radar pixel cell. During the following 'Range Doppler Terrain Correction ', the elevation data from the Space Shuttle Topography Mission

(SRTM) in a spatial resolution of 3 arc-seconds served to transform the radar images from slant range geometry into the UTM coordinate reference system. Pixel spacing of the resultant geocoded product was set to 2 m to minimize spatial information loss, and to meet the file requirements of a manageable product. The main drawback of the SAR image with regard to the visible interpretation is the speckle effectwhich is an inherent noise of all radar images, often called grainy salt and pepper noise. To reduce this effect, a mean image of the five geocoded images was calculated and a 3x3 mean speckle filter applied. The radiometric resolution was reduced from 16 bits to 8 bits. Therefore, the data size was considerably reduced. Likewise, the image representation speed was dramatically increased. In spite of a radiometric information loss during this procedure, the processed TerraSAR-X reference image provides sufficient information for human interpreters to clearly define unambiguous GCPs with a high spatial resolution. Absolute radiometric calibration was not needed in this process as all five images have the same calibration constants, and moreover, the quantitative analysis of the backscattered signal was not the focus of this study. The resultant greyscale radar image was almost specklefree and the shapes of all objects necessary in this research could be identified.

4.5.3 Georeferencing of TopographicVector Data

Georeferencing of the topographic vector data was based on a rubber sheeting algorithm. The rubber sheeting, alternatively called rubber sheet, algorithm is one of the earliest and the most common computer cartogram algorithms (Tobler 2004). This technique derives its name from the logical analogy of stretching a piece of rubber to fit over some objects (Cobb et al. 1998). During the process, map areas are subdivided into triangular-shaped regions and local adjustments are applied on each single region. After that, each triangle either enlarges or shrinks iteratively toward its ideal size without changing the topology of the map (Gillman 1985) (Dougenik et al. 1985). An iterative math-physical cartogram algorithmfor continuous area

was proposed by DOUGENIK et al. (1985). This algorithm was recently improved by implementing an auxiliary quadtree structure in the process (SUN 2013b) (SUN 2013a).

In this study, the rubber sheeting tool of ArcGIS 10.1 was used to transfer the topographic vector data. Approximately 600 reference points, evenly distributed over the entire area of Qixing Farm, were selected as georeferencing points from the TerraSAR-X reference image. As REINARTZ et al. (2009) proposed, the selection of reference points from the TerraSAR-X image is not always a straightforward procedure. Based on our experience, corresponding points were selected according to following rules: (i) Select points in the TerraSAR-X reference image that are located at the intersection of the paddy field ridges, rural road edges, canopy crossings of different crops, or corners of artificial waters, which are in all cases clearly identifiable and unchanged during the 3 year-period from 2009 to 2012. (ii) Avoid elevated objects such as forest edges or tall buildings due to their systematic locational errors such as foreshortening, layover, and shadowing, induced by the radar imagery acquisition procedure. (iii) Select only points that have a corresponding (tie) point in the vector dataset, e.g. the Qixing Farm boundary data with line intersections and corners. A similar process was applied to the topographic GIS data provided by the NGCC.

4.5.4 Georeferencing of Optical remote sensing Data

Multiple optical remote sensing aforementioned data were also selected to demonstrate the georeferencing process based on the TerraSAR-X reference image. In particular, image subsets covering the Qixing Farm were created for the Huanjing and Landsat-5 satellite data. All optical satellite images were georeferenced according to these main steps: First, all satellite images were reprojected into the UTM WGS 84 system to obtain an overview of the data inconsistencies. Second, a set of control points was selected from the TerraSAR-X reference image based on the aforementioned rules. Consequently, the corresponding points have to match the objects which can be clearly identified in the optical remote sensing imagery in this case. Third, in order to

improve the transformation model and to minimize the errors caused by the manual measurement, GCPs and corresponding tie points were updated iteratively by eliminating the points with highest PEs and selecting additional control points until the residual errors fell below the maximum allowed value. The decision if a PE value was too high depended on the spatial resolution of the image to be georeferenced. For every single GCP, the maximum allowed value was within the subpixel range. Finally, a certain number of independent points were defined as check points to evaluate the accuracy of the transformation. During the validation process, the GCPs were used to calculate the transformation model while the check points were used to evaluate the errors in the geometric transformation independently. In our case, the PE is the horizontal distance between the input location of a GCP and the transformed location of the same GCP. The PE was calculated according to Congalton & Green (2008).

$$PE = \sqrt{(\Delta X^2 + \Delta Y^2)}, \tag{4.1}$$

where ΔX and ΔY are the positional differences between the reference point and the corresponding image or map position in the X and Y directions, respectively.

4.6 Results

4.6.1 Georeferencing Results of Topographic Vector Data

After the georeferencing based on the rubber sheeting algorithm, the georeferenced vector data of the Qixing Farm field boundaries (cyan) sufficiently fit to the new field boundaries which are clearly detectable in the TerraSAR-X image. The problem of nonsystematic spatial inconsistency was well overcome and the shape of the vector graphics was preserved (Figure 4.3). Similar results were also obtained for the topographic data provided by the NGCC.

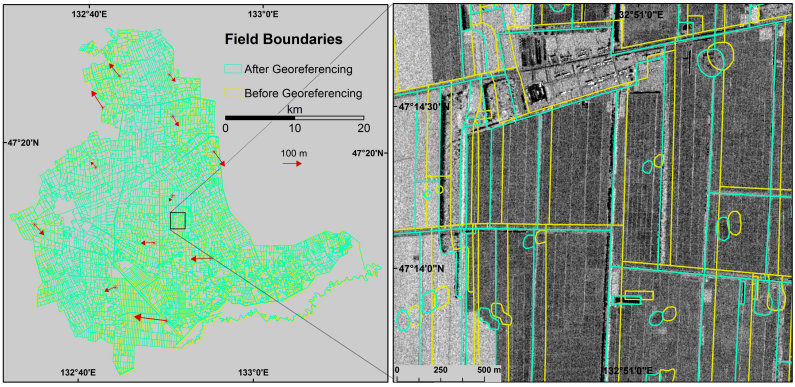

Figure 4.3: Field boundary data, before (yellow) and after (cyan) the georeferencing; red arrows in the left figure show the vector force of the rubber sheeting procedure. Background data in the right figure: TerraSAR-X reference image.

4.6.2 Georeferencing results of optical remote sensing data

Optical remote sensing data were georeferenced according to the method described in the previous sections. Table 4.1 shows the relevant information of the selected GCPs. After recursively selecting control points, the final PEs were less than half a pixel for both the Huanjing (CCD2) and Landsat-5 images, and nearly one pixel for the FORMOSAT-2 and RapidEye images. Figure 4.4 shows the georeferencing results visually. The ground features from each of the images fit well. The roads match properly in all images and the paddy field block boundaries are ideally aligned to each other in the higher resolution images (TerraSAR-X, FORMOSAT-2 and RapidEye).

Satellite	Pixel Size (resampled) (m)	Imagery/subset spatial extension (km)	Number of control points	PE (average) (m)	PE (max.) (m)	PE (min.) (m)	Std. (m)
Huanjing(CCD2)	30 x 30	55 x 55	100	12.66	27.39	1.87	6.70
Landsat-5	30 x 30	48 x 68	220	9.04	16.63	0.59	3.85
FORMOSAT-2	2 x 2 (PAN)	30 x 28	143	3.43	5.91	0.3	1.35
RapidEye	5 x 5	24 x 24	64	4.09	9.36	0.60	2.12

Table 4.2: Accuracy of the selected GCPs (PE = positional error, Std. = standard deviation).

4.6.3 Spatial accuracies of the georeferenced optical remote sensing data

To evaluate the spatial accuracies of the georeferenced optical remote sensing data, independent check points covering the whole scene were created and their spatial parameters were analyzed. To capture the maximum PE results, the check points were located in the areas where the GCP density was relatively low. The results were summarized in Table 4.3. The average PEs of the check points were at a sub-pixel value (slightlymore than 0.1 pixel) in the Huanjing (CCD2) and Landsat-5 images. Accuracies of 2.5 pixels and 1.3 pixels were achieved for the FORMOSAT-2 and RapidEye imagery, respectively. The average PE values for all four types of satellite images ranged from 3.11 m to 6.66 m.

4.7 Discussion

4.7.1 Analysis of the Anticipated Spatial Error in the Processed TerraSAR-X Reference Image

The geometric distortion of SAR imagery products can be caused by three components (Curlander & McDonough 1991a): (i) sensor/ platform instability and signal propagation effects, (ii) terrain height, and (iii) processor induced errors. The uncertainties embedded in the SSC products comprise only the first type of error, which is less than

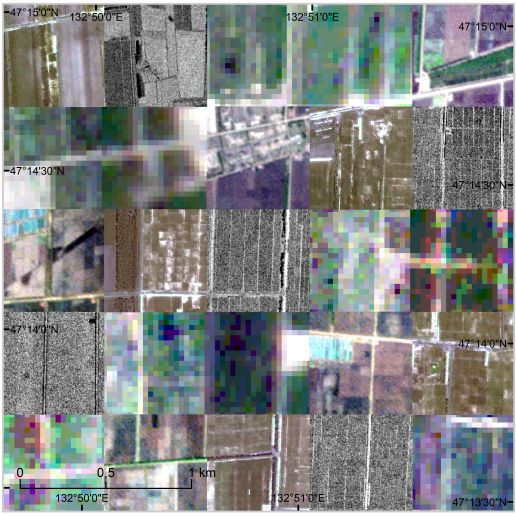

Figure 4.4: An example of georeferenced multi-source remote sensing images in comparison to the TerraSAR-X image. From left to right: 1st row: FORMOSAT-2, TerraSAR-X, Landsat-5, Huanjing, RapidEye; 2nd row: Landsat-5, Huanjing, RapidEye, FORMOSAT-2, TerraSAR-X; 3rd row: RapidEye, FORMOSAT-2, TerraSAR-X, Landsat-5, Huanjing; 4th row: TerraSAR-X, Landsat-5, Huanjing, RapidEye, FORMOSAT-2; 5th row: Huanjing, RapidEye, FORMOSAT-2, TerraSAR-X, Landsat-5.

1 m ((Nonaka et al. 2008),(Fritz & Eineder 2013)). The second type of errors comes from the SRTM DEM dataset. Rodriguez et al. (2006) found that the absolute height error of the SRTM in Eurasia was less than 6.2 m; whereas in the Sanjiang Plain study site, where the topography is fairly flat, the absolute error was less than 2 m according to the SRTM terrain height error data product. Hence, the target range location error (ΔR) determined by the terrain height

estimation can be calculated using (2) (Curlander & McDonough 1991a):

$$\Delta R = \Delta h / \tan \eta \tag{4.2}$$

where Δh is the height (DEM elevation) estimation error (2 m) and η is the location incidence angle (35 º in this study). Therefore, the ΔR for this study was calculated as 2.86 m. The processor induced error is process dependent and is denoted as $\Delta\delta_i$. The overall absolute spatial error of the projected TerraSAR-X imagery can therefore be calculated by these three components,with the result of (3.86 + $\Delta\delta_i$) m. Where the processor induced error $\Delta\delta_i$ during TerraSAR-X image processing can be assumed to be infinitely small.

Satellite	Pixel Size (resampled) (m)	Imagery/subset spatial extension (km)	Number of check points	PE (average) (m)	PE (max.) (m)	PE (min.) (m)	Std. (m)
Huanjing(CCD2)	30 x 30	55 x 55	20	3.29	8.05	1.81	1.55
Landsat-5	30 x 30	48 x 68	34	3.11	16.48	1.80	1.11
FORMOSAT-2	2 x 2	30 x 28	30	5.08	7.44	1.07	1.89
RapidEye	5 x 5	24 x 24	10	6.66	8.42	4.08	1.21

Table 4.3: Accuracy of the independent check points.

4.7.2 Quantified Spatial Accuracy of the Georeferenced Datasets

Considering all spatial inconsistent sources, the overall absolute error of the georeferenced datasets can be estimated. The overall errors of the georeferenced optical remote sensing data, which is equal to the sum of the PE in Table 4.3 and the geometric distortion of the TerraSAR-X image (3.86 m), were 7.15 m, 6.97 m, 8.94 m, and 10.52 m for Huanjing, Landsat-5, FORMOSAT-2, and RapidEye satellite images, respectively. Dai & Khorram (1998) found that a registration error of less than onefifth of a pixel should be achieved to detect 90% of the true changes. Hence, the registration results for the Huanjing (CCD2) and Landsat-5 images can support a change

detection analysis with a spatial error close to 10%. In surface area estimation, Ozdogan & Woodcock (2006) noted that spatial errors are dependent on both remote sensing image resolution and the field size because of 'the distribution of subpixel proportions ', especially when the field size is similar to or less than the remote sensing data resolution. In this study, the results of the FORMOSAT-2 and RapidEye images processing are sufficient for field-unit level analysis since the size of each field block unit is typically larger than 5,000 m^2. The field block is the smallest area of a farm management unit and is considered as the primary scale for management decisions. The high accuracies for the Huanjing and Landsat-5 image processing are also beneficial for studies at the farmer-unit level, as a farmer's crop field is generally larger than 20 ha. Figure 4.5 provides a visual result of datasets from multiple sources over the entire area of the Qixing Farm.

4.7.3 Feasibility of the Approach

In this study, topographic vector datasets and optical remote sensing images from multiple sources were georeferenced using GCPs derived from the TerraSAR-X reference image without the need for labour intensive field work. The creation of the TerraSAR-X reference image and its use to locate accurate GCPs is critical, because it not only determines the precision of the results but also the feasibility of this method.

Although many studies (Sowmya & Trinder 2000; Sohn & Dowman 2007; Reinartz et al. 2009) have attempted to extract geometric features, e.g. GCPs, automatically from satellite images, there is a lack of reports on automatic methods for georeferencing multi-source data. Automatic feature extraction methods have limited applicability due to their complex parameterization and strict condition requirements (Cobb et al. 1998). Moreover, automatic methods for integrating GIS data and satellite imagery are rare.

The strategy proposed in this study showed that for each dataset, different GCPs were required due to the diverse characteristics of the

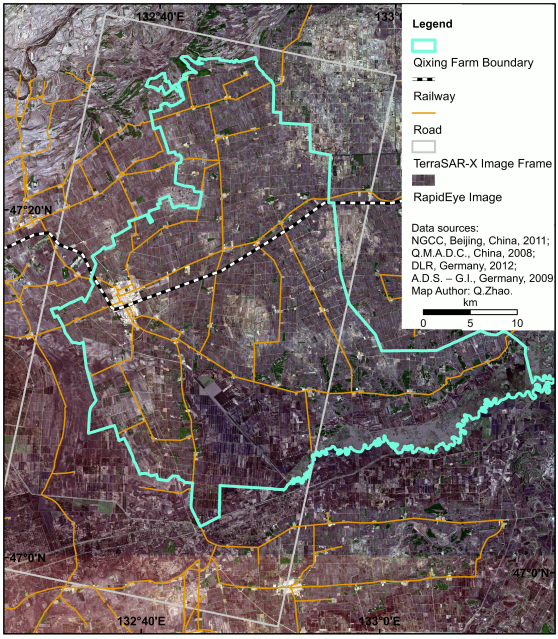

Figure 4.5: Georeferenced multi-source data for the study area of Qixing Farm.

multi-source data. Manual procedure meets this requirement and ensures the spatial accuracy. Although the high resolution TerraSAR-X imagery supplies a sufficient number of GCPs, the selection of the GCPs and their corresponding tie points is never straightforward. There is still a need to establish the criteria for selecting reference points systematically. Another drawback of this method is its inefficiency in processing a large number of datasets. However, the proposed method still is especially valuable for data-poor environments lacking reference data.

4.8 Conclusions

This study provides an applicable and costeffective approach for georeferencing multisource data with different characteristics and non-systematic spatial inconsistencies. It is an especially beneficial technique for large study sites with limited accessibility and reference maps. The results demonstrated the feasibility of using TerraSAR-X imagery to accurately georeference multi-source datasets without in-situ GCP data collection.By using the mean of five TerraSAR-X images and the mean filter, a speckle-free reference image was generated. This proved to be critical for locating sufficient GCPs successfully. The PEs of the check points were less than 0.2 pixel for the 30 m resolution images (Huanjing and Landsat-5), approximately 2.5 pixels for the FORMOSAT-2 images, and 1.3 pixels for the RapidEye images. The overall errors were nearly less than 10 m for all four types of images. The discrepancies among each pair of the TerraSAR-X and GIS data were only assessed visually, which demonstrates a need for further study.

4.9 Acknowledgements

This research was funded by the Natural Science Foundation of China (NSFC, project No. 31071859), the International Bureau of the German Federal Ministry of Education and Research (BMBF, project No. 01DO12013), and the German Research Foundation (DFG, project No. BA 2062/8-1). The TerraSAR-X images were provided by the Airbus Defence and Space Geo Intelligence. The GIS data layer of the Qixing Farm field boundary was provided by the Qixing Modern Agriculture Development Center in Heilongjiang, China. The 1:250,000 scale topographic dataset with multiple layers for the study area was provided by the National Geomatics Center of China (NGCC) (http://ngcc.sbsm.gov.cn/). The Huanjing satellite images were acquired from the China Centre for Resources Satellite Data and Application (CCRSDA) (http://www.cresda.com/n16/index.html). The

Landsat 5 TM images were downloaded from the website of the Earth Resources Observation and Science (EROS) Center of U.S. Geological Survey (USGS) (http://eros.usgs.gov/). The FORMOSAT-2 images were obtained from the National Space Organization (NSPO) of Taiwan. The RapidEye satellite images were kindly provided by the RapidEye Science Archive (RESA), German Aerospace Center (Deutsches Zentrum für Luft- und Raumfahrt, DLR). The leading author would also like to acknowledge the support of the China Scholarship Council (Nov. 2010 - Oct. 2014), Beijing, China.

4.10 References

Ager, T. P., Bresnahan, P. C., 2009. Geometric precision in space radar imaging: results from TerraSAR-X. Proc. ASPRS 2009 Annu. Conf, 9–13.

Badurska, M., 2011. Orthorectification and geometric verification of high resolution TerraSAR-X images. Geomatics and Environmental Engineering 5, 13–25.

Bareth, G., 2009. GIS-and RS-based spatial decision support: structure of a spatial environmental information system (SEIS). International Journal of Digital Earth 2(2), 134–154.

Bareth, G., Yu, Z., 2004. Verfügbarkeit von digitalen Geodaten in China. Petermanns Geographische Mitteilungen 148(5), 78–85.

Chen, C.-C., Knoblock, C. A., Shahabi, C., 2006. Automatically conflating road vector data with orthoimagery. GeoInformatica 10(4), 495–530.

Choi, K., Lee, I., 2012. A sequential aerial triangulation algorithm for real-time georeferencing of image sequences acquired by an airborne multi-sensor system. Remote sensing 5(1), 57–82.

Cobb, M. A., Chung, M. J., Foley III, H., Petry, F. E., Shaw, K. B., Miller, H. V., 1998. A rule-based approach for the conflation of attributed vector data. GeoInformatica 2(1), 7–35.

Congalton, R. G., Green, K., 2008. Assessing the accuracy of remotely sensed data: principles and practices. CRC press, Taylor & Francis, Boca Raton, Florida, USA.

Curlander, J., McDonough, R., 1991a. Synthetic Aperture Radar: Systems and Signal Processing. JohnWiley& Sons, New York, USA.

Dai, X., Khorram, S., 1998. The effects of image misregistration on the accuracy of remotely sensed change detection. Geoscience and Remote Sensing, IEEE Transactions on 36(5), 1566–1577.

Dougenik, J. A., Chrisman, N. R., Niemeyer, D. R., 1985. An algorithm to construct continuous area cartograms. The Professional Geographer 37(1), 75–81.

Fritz, T., Eineder, M., 2013. *TerraSAR-X Ground Segment Basic Product Specification Document*. 1.9. https://tandemx-science.dlr.de/pdfs/TXGS-%20DD-3302_Basic-Products-Specification-%20Document_V1.9.pdf, 2014-4-18.

Gillman, D., 1985. Triangulations for rubber sheeting. Proceedings of 7th International Symposium on Computer Assisted Cartography (AutoCarto 7), vol. 199.

Gómez-Candón, D., López-Granados, F., Caballero-Novella, J. J., Peña-Barragán, J. M., García-Torres, L., 2012. Understanding the errors in input prescription maps based on high spatial resolution remote sensing images. Precision agriculture 13(5), 581–593.

Gösseln, G., Sester, M., 2004. Integration of geoscientific data sets and the german digital map using a matching approach. International Archives of Photogrammetry, Remote Sensing and Spatial Information Sciences 35.

Koppe, W., Kiefl, N., Hennig, S. D., Janoth, J., 2010. Validation of pixel location accuracy of orthorectified TerraSAR-X products. Synthetic Aperture Radar (EUSAR), 2010 8th European Conference on, 1–3.

Li, D., 2010. Remotely sensed images and GIS data fusion for automatic change detection. International Journal of Image and Data Fusion 1(1), 99–108.

Liu, T., Zhao, Y., 1996. Ecological benefit analysis and estimation of the forest shelter in the Nongken area, Sanjiang Plain. Forest Science and Technology 5, 12–14.

Mittermayer, J., Runge, H., 2003. Conceptual studies for exploiting the TerraSAR-X dual receive antenna. International Geoscience and Remote Sensing Symposium, vol. 3, III–2140.

Nonaka, T., Ishizuka, Y., Yamane, N., Shibayama, T., Takagishi, S., Sasagawa, T., 2008. Evaluation of the geometric accuracy of TerraSAR-X. International Archives of the Photogrammetry, 135–140.

Ozdogan, M., Woodcock, C. E., 2006. Resolution dependent errors in remote sensing of cultivated areas. Remote Sensing of Environment 103(2), 203–217.

Reinartz, P., Müller, R., Schwind, P., Suri, S., Bamler, R., 2011. Orthorectification of VHR optical satellite data exploiting the geometric accuracy of TerraSAR-X data. ISPRS Journal of Photogrammetry and Remote Sensing 66(1), 124–132.

Reinartz, P., Müller, R., Suri, S., Schneider, M., Schwind, P., Bamler, R., 2009. Using geometric accuracy of TerraSAR-X data for improvement of direct sensor orientation and orthorectification of optical sattelite data. Geoscience and Remote Sensing Symposium, 2009 IEEE International, IGARSS 2009, vol. 5. IEEE, V–44.

Rodriguez, E., Morris, C., Belz, J., 2006. A global assessment of the SRTM performance. Photogrammetric Engineering & Remote Sensing 72, 249–260.

Schneider, M., Müller, R., Krauss, T., Reinartz, P., Hörsch, B., Schmuck, S., 2009. Urban Atlas–DLR Processing Chain for Orthorectification of PRISM and AVNIR-2 Images and TerraSAR-X as possible GCP source. Internet Proceedings. 3rd ALOS PI Symposium, vol. 9, 13.

Sohn, G., Dowman, I., 2007. Data fusion of high-resolution satellite imagery and LiDAR data for automatic building extraction. ISPRS Journal of Photogrammetry and Remote Sensing 62(1), 43–63.

Solberg, A. H. S., Taxt, T., Jain, A. K., 1996. A Markov random field model for classification of multisource satellite imagery. Geoscience and Remote Sensing, IEEE Transactions on 34(1), 100–113.

Song, W., Keller, J. M., Haithcoat, T. L., Davis, C. H., 2009. Automated geospatial conflation of vector road maps to high resolution imagery. Image Processing, IEEE Transactions on 18(2), 388–400.

Sowmya, A., Trinder, J., 2000. Modelling and representation issues in automated feature extraction from aerial and satellite images. ISPRS journal of photogrammetry and remote sensing 55(1), 34–47.

Sun, S., 2013a. A fast, free-form rubber-sheet algorithm for contiguous area cartograms. International Journal of Geographical Information Science 27(3), 567–593.

Sun, S., 2013b. An optimized rubber-sheet algorithm for continuous area cartograms. The Professional Geographer 65(1), 16–30.

Tobler, W., 2004. Thirty five years of computer cartograms. ANNALS of the Association of American Geographers 94(1), 58–73.

Usery, E. L., Finn, M. P., Starbuck, M., 2009. Data layer integration for the National map of the United States. Cartographic Perspectives (62), 28–41.

Waldhoff, G., Curdt, C., Hoffmeister, D., Bareth, G., 2012. Analysis of multitemporal and multisensor remote sensing data for crop rotation mapping. ISPRS International Archives of the Photogrammetry, Remote Sensing and Spatial Information Sciences, I-7, 177–182.

Walter, V., Fritsch, D., 1999. Matching spatial data sets: a statistical approach. International Journal of Geographical Information Science 13(5), 445–473.

Wang, Z., Zhang, B., Zhang, S., Li, X., Liu, D., Song, K., Li, J., Li, F., Duan, H., 2006. Changes of land use and of ecosystem service values in Sanjiang Plain, Northeast China. Environmental Monitoring and Assessment 112(1-3), 69–91.

Weber, K. T., Théau, J., Serr, K., 2008. Effect of coregistration error on patchy target detection using high-resolution imagery. Remote Sensing of Environment 112(3), 845–850.

Weis, M., Müller, S., Liedtke, C.-E., Pahl, M., 2005. A framework for GIS and imagery data fusion in support of cartographic updating. Information Fusion 6(4), 311–317.

Wu, X., Carceroni, R., Fang, H., Zelinka, S., Kirmse, A., 2007. Automatic alignment of large-scale aerial rasters to road-maps. Proceedings of the 15th annual ACM international symposium on Advances in geographic information systems, ACM, 17.

Zhang, J., 2010. Multi-source remote sensing data fusion: status and trends. International Journal of Image and Data Fusion 1(1), 5–24.

Zhang, W., 2012. *Personal communication, Qixing Farm, June 2012.*

5 Multi-data approach for crop classification using multitemporal, dual-polarimetric TerraSAR-X data, and official geodata

Christoph Hütt[1], Guido Waldhoff[1]
Published in European Journal of Remote Sensing, 2018 / 51, 1.
Pages 62-74
Original manuscript is embedded in dissertation format.

1. Institute of Geography, GIS & Remote Sensing Group, University of Cologne, 50923 Cologne, Germany,
e-mail: {christoph.huett} {guido.waldhoff}@uni-koeln.de

5.1 Abstract

Crop distribution information is essential for tackling some challenges associated with providing food for a growing global population. This information has been successfully compiled using the MDA. However, the current implementation of the approach is based on optical remote sensing, which fails to deliver the relevant information under

cloudy conditions. We therefore extend the MDA by using Land Use/Land Cover classifications derived from six multitemporal and dual-polarimetric TerraSAR-X stripmap images, which do not require cloud-free conditions. These classifications were then combined with auxiliary, official geodata (ATKIS and Physical Blocks (PB)) data to lower misclassification and provide an enhanced LULC map that includes further information about the annual crop classification. These final classifications showed an OA of 75 % for seven crop-classes (maize, sugar beet, barley, wheat, rye, rapeseed, and potato). For potatoes, however, classification does not appear to be as consistently accurate, as could be shown from repeated comparisons with variations of training and validation fields. When the rye, wheat, and barley classes were merged into a winter cereals class, the resultant five crop-class classifications had a high OA of about 90 %.

5.2 Introduction

Sustainable production of sufficient food for the growing earth population is a challenge (Godfray et al. 2010). Dealing with this challenge requires, among other data, timely information about the distribution of agricultural crops. Timely means that the information is at least provided annually, as crop production is usually linked to a yearly growing season. However, for harvest forecast estimation based on the acreage, the crop classification maps are already needed during the growing season (McNairn et al. 2014). Once this spatial crop information is available, regional agroecosystem models can be established (Reichenau et al. 2016; Simmer et al. 2015) and the crop status monitored (Zhao, Lenz-Wiedemann, et al. 2015). It is even possible to estimate a crop's yield before harvest (McNairn & Shang 2016), which permits better planning of the available resources. Yet, this essential crop information is rarely available in official geodata statistics.

Information about land LULC is widely obtained using remote sensing. Remote-sensing-based LULC and crop distribution mapping at a

regional scale is usually performed using optical remote sensing data of moderate spatial resolution (Atzberger 2013), synthetic aperture radar (SAR) data (McNairn & Shang 2016), or a combination of both (Blaes et al. 2005; Forkuor et al. 2014; McNairn, Champagne, et al. 2009). Prominent are the optical data from the Landsat mission, which have been extensively used for crop-type mapping (Bauer et al. 1978; Homer et al. 2004; Oetter et al. 2001; Tatsumi et al. 2015). Lately, the Sentinel constellation, consisting of optical and radar satellites has also been successfully used for this purpose (Bargiel 2017; Immitzer et al. 2016).

However, classifying the highly dynamic annually grown crops based on remote sensing images usually involves multitemporal acquisitions because obtaining the crop distribution from one single acquisition is not sufficient (Brisco et al. 2013; Bush & Ulaby 1978; Siachalou et al. 2015; Skriver 2012; Sonobe et al. 2014; Van Niel & McVicar 2004a). One reason is the spectral or radiometric limitation of contemporary sensor systems (Vinciková et al. 2010), but the biggest issue is the similarity in reflectance of the fields during most phenological stages. Some crop types are only distinguishable at specific times of the year and appear similar throughout the rest of the growing season. A proper planning of the dates of image acquisition and finding the optimal Acquisition Windows (AWs) for the region of interest are therefore crucial (Foerster et al. 2012; Van Niel & McVicar 2004a).

Besides the multitemporal approach, LULC mapping can also be performed using existing external geodata from mapping agencies (Homer et al. 2004; Lu & Weng 2007; Smith & Fuller 2001). Fusing crop classifications with such data has the advantage that the area that is not used for agricultural production can be excluded from the analysis, which lowers misclassification and allows a more disaggregated LULC analysis. One prominent example is grassland within urban areas: Solely based on the reflectance analysis, it is impossible to differentiate between an urban green area (for example for recreational purposes) and agricultural grassland. However, this is possible using data from the relevant authority.

LULC classifications enriched with missing information about annually grown crops is also the main focus of the MDA (Bareth 2008; Waldhoff et al. 2012; Lussem & Waldhoff 2014; Waldhoff 2014; Waldhoff & Bareth 2009; Waldhoff et al. 2017). It combines multitemporal remote sensing images and external geodata to produce LULC maps, including information about the crops grown each year. It was successfully developed and applied to the Rur catchment in the west of Germany (Waldhoff et al. 2017) and, interestingly, provided ideal points of time for optical image acquisition. However, the existing MDA has a drawback: it has only been implemented using optical data. Unfortunately, frequent cloud coverage means that, even when multiple optical data sources and external geodata are used, appropriate data coverage for optimal crop differentiation is rarely available (Blaes et al. 2005; Whitcraft et al. 2015). If no image can be acquired for a particular timeframe, the accuracy of the classes to be separated within that timeframe inevitably decreases.

To prevent clouds from lowering accuracy, microwave images produced by SAR have been used for crop classification in many scenarios (e.g. recently, Bargiel (2017), Hütt, Koppe, et al. (2016), and Sonobe et al. (2014)), or they have been combined with optical acquisitions (Blaes et al. 2005; Forkuor et al. 2014; McNairn, Champagne, et al. 2009). Radar-based crop identification goes back to Simonett (1967). Bush & Ulaby (1978) highlighted the significance of multitemporal radar measurements for successful crop classification. Hoogeboom (1983) successfully identified crops on the ground in experiments with airborne SAR images. Since then, crop classification capabilities of SAR systems have been demonstrated in many studies (e.g. Foody et al. (1994) and Skriver (2012), recently particularly on board satellites (McNairn & Shang 2016).

SAR sensors have the advantage of working regardless of the weather and illumination conditions on the ground. Consequently, capturing images during the crucial crop stages does not depend on cloud-free conditions. Additionally, SAR allows polarimetric analysis of the electromagnetic wave, which enables differentiation of scattering mechanisms on the ground (Cloude & Pottier 1997). In a crop

classification context, these mechanisms are related to crop phenology (Koppe et al. 2013; Lopez-Sanchez et al. 2012), but most importantly to crop type (Skriver et al. 1999), and hence are well suited to crop classification. However, most SAR-based crop classification studies usually neglect to fuse the classification with external official geodata (e.g. McNairn, Champagne, et al. (2009), Skriver (2012), and Sonobe et al. (2014). One exception to this lack was the study by Bargiel (2017). However, in that study the external data was merely used to mask out non-crop areas during the classification process and not to enhance existing geodata.

The previous research has therefore shown that the MDA is useful as it fuses remote sensing images with external geodata, but it uses optical remote sensing images for its implementation and thus requires cloud-free conditions. The MDA would be improved if it were to use SAR, which delivers images even under cloudy conditions. Enhancing the MDA framework by integrating SAR images is consequently a logical next step in improving timely information about crop distribution. This study therefore focuses on three objectives: (I) Examining whether those points in time that proved ideal for optical image classification are also valid for dual-polarimetric TerraSAR-X images. (II) Investigating the potential of using the images to differentiate crops. (III) Studying how to apply the concept of the MDA to fuse the SAR-based classifications with external geodata and thus to produce a crop type enriched LULC map.

5.3 Study Site and Data

5.3.1 Rur Catchment

The Rur catchment is located in Western Germany and partly in Belgium and the Netherlands. Figure 5.1 shows the study area, located in the northern part of the Rur catchment. Arable land dominates this area on a fertile loess plain. The fertile soil and the warm-temperate climate with sufficient precipitation make the area

ideal for intensive agriculture. The main crops are winter wheat, winter barley, winter rye, sugar beet, maize, rapeseed, and potato (IT.NRW 2016).

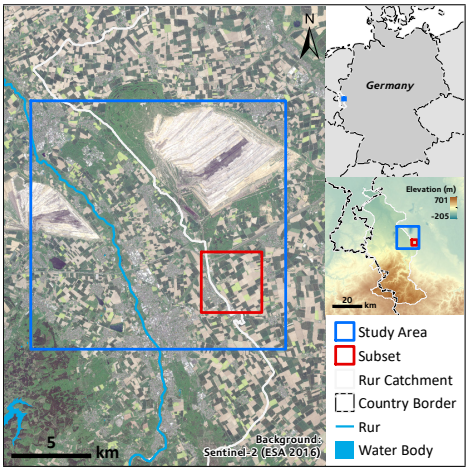

Figure 5.1: Location of the study site. Image Background: Sentinel-2 image acquired 08.05.2016, Band Combination 4-3-2.

5.3.2 TerraSAR-X radar data

The radar remote sensing satellite TerraSAR-X was successfully launched in 2007. It provides x-band microwave images in different imaging modes, resulting in various resolutions and different polarization combinations (Breit et al. 2010). For this study, we acquired six high-resolution TerraSAR-X dual-polarimetric (HH/VV) stripmap scenes between May and August 2013. These six SAR images are a time series taken from the same relative orbit; this means the satellite was at almost the same position during the image acquisitions. Consequently, all images have a similar viewing geometry, extent, and

resolution and similar geometric distortions. The individual image characteristics and exact imaging dates are specified in Table 5.1.

Sensor-related characteristics (the same for all acquisitions)	No.	Date	AW (acquisition window)
Satellite/sensor: TerraSAR-X	1	May 5, 2013	AW 1
Wavelength: X-band / 3.6 cm	2	June 5, 2013	AW 2
Imaging mode: stripmap	3	June 16, 2013	AW 2
Orbit: descending, Incidence angle: 35.5°	4	June 27, 2013	none
Time of acquisition: 5:51 (UTC)	5	July 30, 2013	AW 3
SLC resolution: 1.55 m (Rg.) × 2.39 m (Az.)	6	August 21, 2013	AW 4
Scene extent: 18.5 km (Rg.) × 56.5 km (Az.)			
Polarizations: HH & VV			

Table 5.1: Radar remote-sensing image statistics.

5.3.3 Field campaign and collection of ground data

During the growing season of 2013, the real ground situation was mapped by visiting selected agricultural areas of the region at times chosen according to the phenology and management practices of the selected crops. Table 5.2 presents an overview of the quantity and the size of the fields used for this study.

5.3.4 Ancillary and official geodata for the MDA

MDA generally aims to combine multitemporal remote sensing classifications and external geodata. In this study, the ATKIS, as the official Digital Landscape Model (DLM), and PB data were chosen.

ATKIS provides details of feature boundaries, and land cover information in vector format. The spatial accuracy is at least ±3 m (AdV 2006) for the ATKIS Basis DLM, which is sufficient for our investigation considering a spatial resolution of 15 m of the final classifications.

PB were used for the delineation of agricultural areas (Waldhoff et al. 2017), they consist of land parcels of the same land use type (e.g. arable land, Grassland or permanent crops), which are always

enclosed, e.g. by a road (Landwirtschaftskammer, NRW 2011). No individual parcels with a single crop type can be differentiated in this way, but at least, on an annual basis, agricultural areas can be separated from other land use types. For our study site, the PB data were provided by the LWK-NRW (2016). However, PB are part of the EU-wide LPIS and therefore similarly available for the whole of the EU.

Crop type	Number of fields	Min. field size (ha)	Max. field size (ha)	Mean field size (ha)	Total area (ha)	Number of Pixels (15x15m)
Maize	9	0.2	4.4	2.0	18.0	722
Sugar Beet	7	0.3	8.9	2.7	19.1	919
Barley	12	0.9	11.2	4.8	57.9	2,675
Wheat	8	0.8	6.7	2.2	17.4	714
Rye	12	0.6	13.5	4.9	58.7	2,575
Rapeseed	8	0.4	13.7	3.2	25.4	1,129
Potato	6	0.6	11.0	5.3	31.5	1,414
Total	62	0.2	13.7	3.7	228.0	10,148

Table 5.2: Overview of collected reference data.

5.4 Methods

5.4.1 Separation of crops using acquisition windows

For this region, Waldhoff et al. (2017) studied the optimal point in time (AWs) to separate the crops of the region using optical remote sensing images. AWs are time periods during the growing season during which crop separation is most favorable in this specific region. Based on the theory behind AWs, optimal crop separation is possible when at least one image for each of the AWs is available. As can be seen in Table 5.3, separation is based either on a different crop phenology or on different crop-specific management practices, which both lead to changes in reflectance when optical images are used. In the radar images utilized in this study, the changes led to different backscattering

mechanisms, which can be detected using radar polarimetry (Skriver et al. 1999). The TerraSAR-X acquisition dates match the AWs proposed by Waldhoff et al. (2017). As can be seen in Table 5.1, in our study at least one image exists for every AW, except for AW5, which has the same purpose as AW4 and normally serves as a backup window when no image can be acquired in AW4.

AW	Time period	Differentiation
1	End of April–End of May (ca. 25.04–25.05)	Winter cereals, rapeseed, early potatoes
2	Beg. – mid-June (ca. 01.06–15.06)	Winter wheat, barley, summer cereals, potatoes
3	Mid-July–beg. of Aug. (ca. 15.07–07.08)	Possibly potatoes, maize, sugar beet
4	Mid.–end of August (ca. 15.08–31.08)	Potatoes, maize, sugar beet
5	Beg.–mid-September (ca. 01.09–15.09)	Potatoes, maize, sugar beet

Table 5.3: Acquisition windows (AW) for optimal crop separation in the Rur area, adopted from Waldhoff et al. (2017).

5.4.2 Preprocessing of the TerraSAR-X images

For a successful crop classification, it was necessary to extract all relevant information contained in the TerraSAR-X microwave images. Figure 5.2 shows the processing chain for each acquisition, the multitemporal combination and the fusion with the external geodata. First, from each dual-polarimetric TerraSAR-X scene, we derived the absolute backscatter values in dB to analyze the amount energy received from the ground. Additionally, to include information about the scattering mechanism, the following polarimetric features were retrieved: dual-pol entropy, dual-pol alpha angle, the degree of polarization (Cloude et al. 2012), and the covariance matrix elements C11,

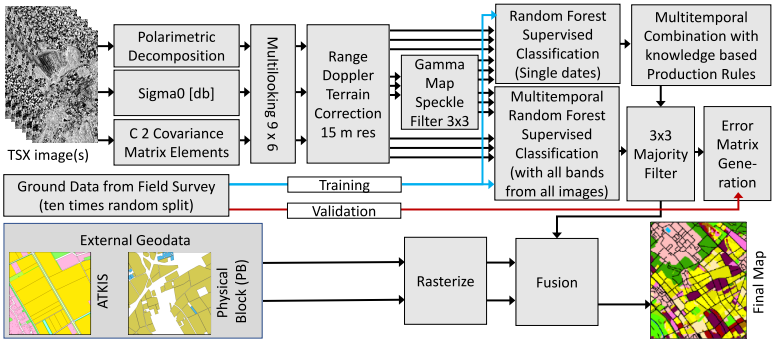

Figure 5.2: Workflow diagram to create the final LULC map from TerraSAR-X images, the ground survey, and the external geodata.

C12 (real and imagery), C22. Following this, a multilooking of nine pixels in range and six in azimuth was conducted, which, although it reduces the spatial resolution, minimizes the speckle effect. To project the images to the ground, a Range Doppler Terrain Correction as described by Curlander & McDonough (1991a) was performed using the digital elevation model (DEM) from the SRTM mission (Jarvis et al. 2016). The low error of the SRTM in the study region (Bhang et al. 2007) and the high geometric accuracy of TerraSAR-X (Nonaka et al. 2008) result in a high geometric accuracy of the final images and consequently also of the classifications. Hence, the classifications from TerraSAR-X are suited for fusion with other geodata and do not require manual orthorectification.

During the projection to the ground, the final pixel size was set to 15 m. This resolution was considered sufficient to differentiate single parcels and was chosen as a tradeoff between computation efficiency and accounting for the expansion of roads and accompanying non-agricultural vegetation, such as grass or shrubs that dissect agricultural landscapes. It is also the same spatial resolution as the annually

created MDA land use classifications, which are generated for the whole Rur catchment using optical images (Waldhoff et al. 2017).

Finally, all bands were filtered using a gamma map speckle filter with a moving window size of 3×3. The unfiltered and filtered image bands were stacked and utilized for the supervised classification.

5.4.3 Supervised single-date and multitemporal classification

For the supervised classification, the polygons representing the fields were randomly separated 10 times into a training dataset and an independent validation dataset. Subsequently, to minimize field border effects, a 15 m buffer was subtracted from the boundaries of the fields. All individual rasters derived from one single TerraSAR-X scene were used to create the single-date classifications. The RF classifier was used because it is superior to other algorithms (Ok et al. 2012) and well suited to crop classification scenarios using SAR data (Hütt, Koppe, et al. 2016; Sonobe et al. 2014). The parameters of the RF classifier were left to the default values of the used R-language library. The numbers of features randomly chosen at each node were determined by the square root of the available variables. The number of trees was set to 500. As the parameter node size was set to unlimited; the full tree was grown at each classification.

For the multitemporal classification, two approaches were investigated: First, all image bands that were used for the single-date classifications were stacked and classified using the RF classifier. The second method is inspired by optical image analysis and the MDA proposed by (Bareth 2008). That procedure combines remote-sensing land use classifications and uses expert knowledge-based production rules, which allow incorporation of multitemporal information on crop phenology and management practices (Waldhoff et al. 2017). The rules were applied to the stack of all single-date classifications and developed based on the error analysis, knowledge of plant phenology and logic. For example, if a pixel was identified as a summer crop, e.g. bare ground, in the first acquisition, this pixel will then not be

classified as a winter crop based on a later acquisition. This approach is more user-controlled than others, and valuable information for each crop can be extracted (Waldhoff et al. 2012).

A majority filter with a 3×3 window size was used to enhance the accuracy of all final classifications. The accuracy was assessed using the independent validation part of the ground reference data. Based on the resulting error matrix, accuracy statistics such as the OA, the user's and producer's accuracy (Congalton 1991), and the F1-score (Bargiel 2017) for each class were produced. These statistics are used to evaluate the accuracy of the classifications, both single-date and multitemporal, and helped to develop the production rules for the multitemporal classification.

5.4.4 Software packages used

Preprocessing of the TerraSAR-X radar data was done using the open source software SNAP provided by the European Space Agency. The RF classification was implemented in R using the RF library (Liaw & Wiener 2002) and a modified R script made available by Horning (2013). Expert knowledge rules were executed using the ArcGIS Python scripting extension. Error matrix generation, accuracy evaluation, and map generation were also performed using ArcGIS.

5.5 Results

5.5.1 Single-date classifications and optimal point in time to separate the crops

Using the time series of six TerraSAR-X acquisitions made it possible to identify points in time to separate the region's crops. Figure 5.3 presents the OA of the single date and the multitemporal classifications. Figure 5.4 shows the resultant F1 scores of the different LULC classes over time. It shows that the very early acquisition in the middle of May resulted in the highest class-accuracies for rapeseed (97 %), and

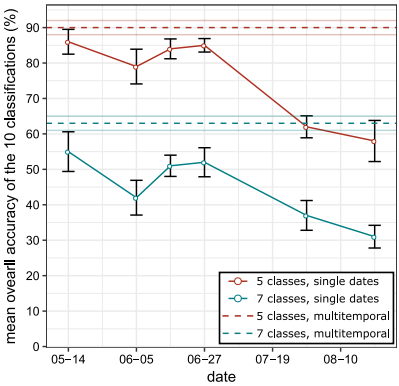

Figure 5.3: Mean OA of the single dates and the multitemporal approaches; seven classes and five classes (after merging barley, rye, and wheat to winter cereals). The error bars indicate one standard deviation of the 10 random splits into training and validation datasets.

a relatively good separation for potatoes (77 %). However, the 10 repetitions with different training and validations fields revealed a high standard deviation of 31 % for the accuracy in identifying the potato class. Furthermore, the early acquisition is necessary to separate the winter crops wheat, rye, and barely from the summer crops maize and sugar beet. While the winter crops have a full canopy closure at the time of the first acquisition, the summer crops are generally characterized by bare soil.

A further analysis of the accuracy over time shows that rapeseed is very well classified in the images taken before harvest. Based on experience from the optical analysis, we anticipated that, for the summer crops sugar beet and maize, the second half is more important. Strikingly, the highest accuracies were observed in the third and fourth date (16th and 27th June), where the maize plants and the sugar beet plants had just emerged. Although the winter cereals barley, wheat,

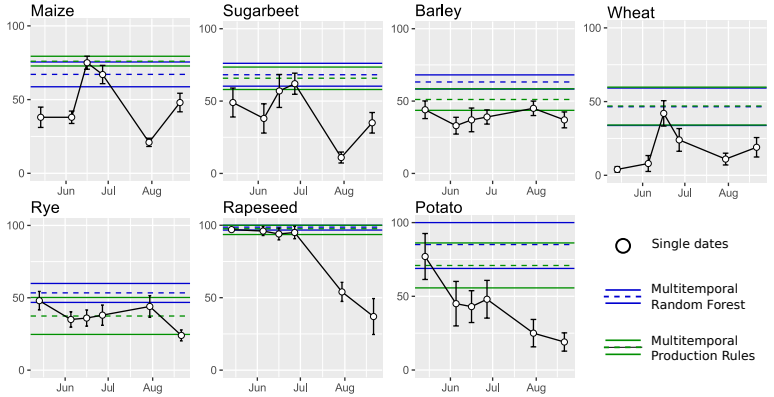

Figure 5.4: F1-scores (in %) of the classes in the single-date classifications and the multitemporal accuracy. Error bars indicate one standard deviation of the 10 random splits into training and validation.

and rye are easily distinguishable from all other classes, no optimal point in time for their disaggregation could be identified as attempts to classify them using the single dates rarely exceeded 50 % accuracy.

5.5.2 Class accuracies of the multitemporal supervised crop classification

By using the multitemporal information of the six dual-polarized TerraSAR-X acquisitions, it was possible to create improved multitemporal classifications. The winter crops barley, wheat, and rye were easily separable from the summer crops maize and sugar beet, mainly based on the good separation in the 1st acquisition. The classification accuracies of rapeseed and winter cereals were increased by the multitemporal analysis and reached the highest single-class accuracies of up to 99 %. Potatoes were classified with an adequate accuracy (RF 85 %,

Production Rules 71 %), but the high standard deviation of those accuracies found in the single-date classification from the first date could not be lowered in the multitemporal approaches and remained at the high level of about 32 %. The disaggregation of maize and sugar beet had lower F1-Scores of 66–76 %, mostly due to misclassification within the two classes but also from a confusion with potato. In this study, disaggregation of the winter cereals into barley, wheat, and rye was not satisfyingly possible.

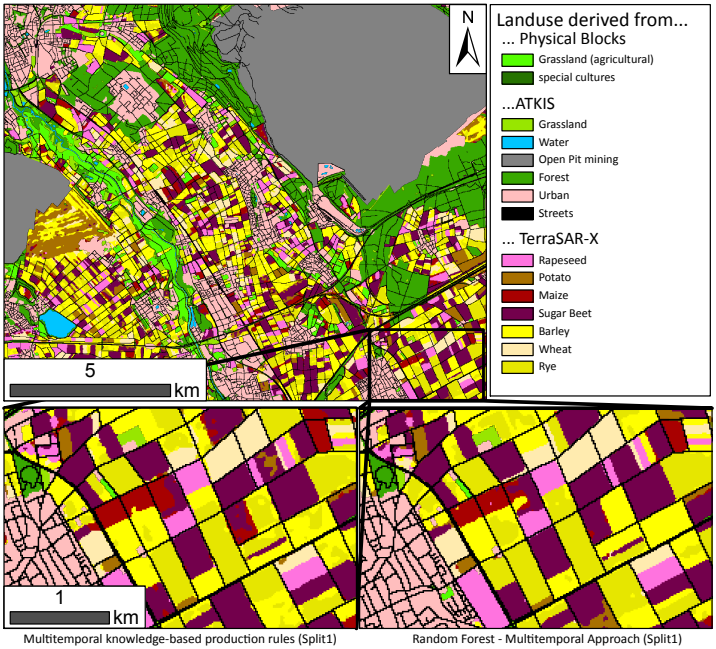

Figure 5.5: Map of the final classification. The lower part shows the difference between the production rules and the multitemporal random forest approach.

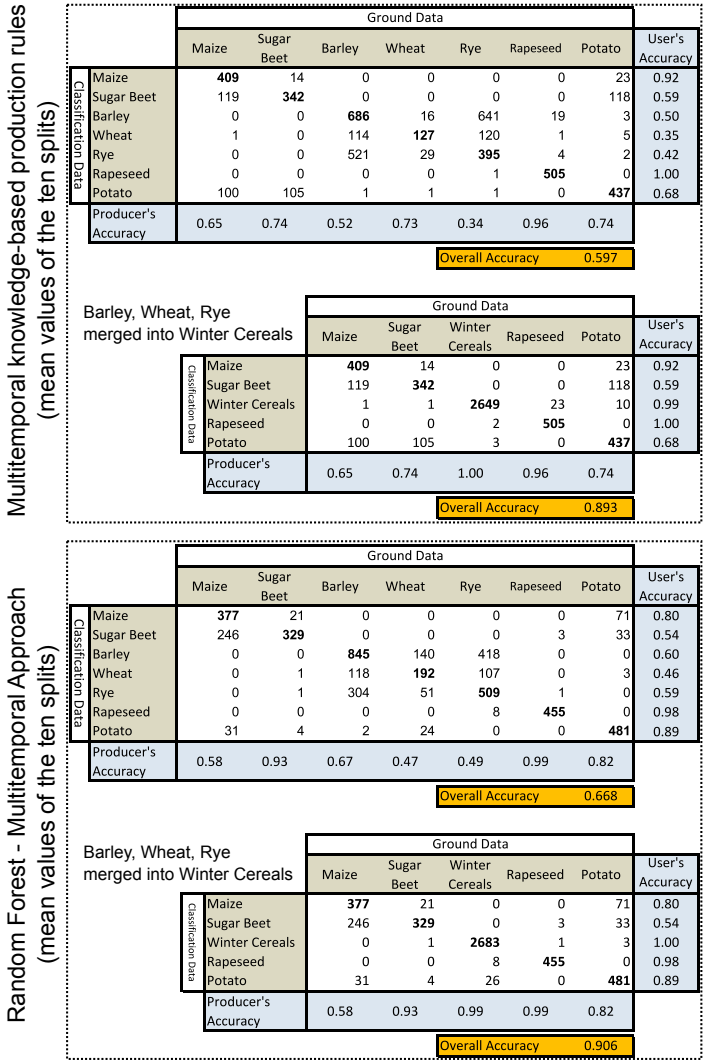

Figure 5.6: Mean error matrices of the two multitemporal methods.

5.5.3 Comparison of the multitemporal classification approaches

A comparison of the two multitemporal approaches shows that the multitemporal RF classification delivered a 7 % higher OA for the seven crops classification (Figure 5.5), the multitemporal combination with knowledge-based production rules still extracted most of the multitemporal information and provided an OA of 60 % (Figure 5.6). By merging the winter cereals, a higher accuracy 5-crop classification was created, with an accuracy of about 90 % for both approaches. However, due to the relatively high variance of the accuracies depending on which combination of training and reference fields was taken (exact values in Table 5.4), a significant difference in the mean OA between the two approaches could not be found in this study. By using 10 repetitions, with different training and validation fields, a significantly lower standard deviation of the accuracies of the knowledge-based approach could be achieved (F-test, $\alpha < 5\,\%$, $n = 10$). The efficient production rules meant that the computational resources were used more efficiently: no new classifications had to be performed. However, the very long runtime for the multitemporal RF given in Table 5.4 could be shortened by tuning the parameters of the RF classifier. The visual comparison of the maps created by the two approaches justifies the accuracy analysis above; major differences are rare. The RF classification maps contain specific errors that are seldom found in the knowledge-based result. For example, as can be seen from the comparison in Figure 5.6, winter wheat is sometimes obviously confused with maize. In the knowledge-based approach, misclassification is more likely to appear only within the summer or winter crops.

5.5.4 Fusion of the classifications with external geodata ATKIS and PB

Figure 5.5 shows the final LULC map. The high geometric accuracy of the TerraSAR-X classifications and the very low positional error of ATKIS and PB allowed a fusion without the need for additional

		Single dates random forest	Multitemporal production rules	Multitemporal random forest
Mean OA of 10 splits	7 classes	45%	59%	66%
	5 classes	76%	89%	90%
Standard deviation of OA (10 splits)	7 classes	11%	4%	10%
	5 classes	13%	3%	7%
Mean runtime for one classification (2.7 GHz Intel Core I5, 8 GB Ram)		~ 9 min	Less than 1 min	~ 6 h

Table 5.4: Comparison of the two multitemporal approaches.

co-registration. The data sets match on the pixel level. To lower misclassification, all non-agricultural classes were excluded from the classification process. Also, an enhanced LULC map including all information from ATKIS, PB, and the missing information of crop type is available. For demonstration purposes, to produce the map shown in Figure 5.5, the ATKIS and PB data were reclassified, allowing the datasets to be generalized. Originally, the ATKIS dataset contained numerous different LULC classes on transportation, built-up areas, agricultural land and other vegetation (AdV 2006). The complete PB data provide information about coherent parcels of the same agricultural land use type, such as arable land, grassland, and permanent crops (Landwirtschaftskammer, NRW 2011). All original LULC classes are available in the geographic information system (GIS).

5.6 Discussion

5.6.1 Objective I: optimizing the acquisition plan based on the findings of this study

Based on crop development and crop management practices in the Rur area, earlier studies (Waldhoff et al. 2012; Waldhoff 2014; Waldhoff et al. 2017) identified five AWs (Table 5.2) during which optical remote sensing images should be acquired if the annually grown crops are to be successfully identified. The first objective of our study was to assess whether the AWs from that study still

held for TerraSAR-X images. Our study's TerraSAR-X images are a high-resolution times series that can be acquired independently of cloud conditions. Consequently, the differences in the radar images are mostly influenced by altering conditions on the ground and not by different viewing geometries or atmospheric conditions at the time of image acquisitions. Therefore they provide more insights on optimal points in time for crop classification. From our results, we suggest three adjustments to the acquisition plan proposed by Waldhoff et al. (2017):

1. The last AW is obsolete when using SAR data as it serves the same purpose as AW4. It merely exists as a backup window in case there is no cloud-free image from AW4.

2. A new AW between AW2 and AW3 is needed as the classification from the third and fourth acquisition (Table 5.1) showed the highest accuracy of the classes maize and sugar beet (Figure 5.4). While, in optical analysis, those classes are best separated very late in the growing season (Waldhoff et al. 2012), TerraSAR-X seems most sensitive to the different structure of the emerging plants, which can be seen in relatively high F1 scores of maize and sugar beet in the acquisitions three and four (Figure 5.4). Being able to separate the two classes when the plants are still small enables an early mapping of the two classes and confirms the findings by McNairn et al. (2014), who show that TerraSAR-X and Radarsat-2 imagery can be used to separate maize from soybeans within the growing season. However, as planting dates for maize can vary between regions, farmers, and seed variety, data from later AWs may still be useful.

3. In optical remote sensing, the separation of rapeseed from the winter cereals is mainly achieved by using the bright yellow color of the flowering rapeseed plant. Hence, a thorough planning of the optical acquisitions is needed to image all rapeseed fields during the flowering stage. In this study, identification of rapeseed is highly accurate in all classifications of the first four images

(Figure 5.4). Fieuzal et al. (2013) have already demonstrated that the signal from polarimetric SAR is susceptible to the different crops types rapeseed and winter wheat. Those results are confirmed by our study, in which the separation works well for a prolonged time. Consequently, careful planning to identify rapeseed seems less important.

5.6.2 Objective II: crop differentiation potential of multitemporal and dual-polarimetric TerraSAR-X data

In this study, the classes rapeseed, potato, and winter cereals were mapped with high accuracy. TerraSAR-X can collect the scattering mechanisms related to different crops, crop growth stages, and management practices. Consequently, our study agrees with existing research, e.g. Skriver et al. (1999), who report that multitemporal SAR backscattering signatures capture crop differences well, using correlation coefficients of HH- and VV-polarization, as we did in this study.

The accuracies for maize and sugar beet were moderate due to confusion within the two classes (and with potato), probably because both crops have a broad-leaved plant structure and a similar phenology, leading to a similar x-band temporal signature. However, classification accuracy could be improved by using the different heights of maize and sugar beet at the end of the growing season. Hütt, Tilly, et al. (2016) showed how the height of maize plants could be measured using SAR data from the TerraSAR-X Add-on for Digital Elevation Measurements (TanDEM-X).

A further differentiation of the winter cereals into barley, wheat, and rye was not possible with the data from this study. Interestingly, the same classes show the highest errors in a study performed by Skriver (2012) with multitemporal airborne C- and L-band SAR data. Recently, Bargiel (2017) showed that the winter cereals could be successfully differentiated using c-band radar data of very high

temporal resolution from the Sentinel-1 satellite. Such data could be incorporated in future similar studies.

The experiment of 10 times randomly splitting the training and validation data during the classification process revealed a high variance of the accuracy of the class potato. This high variance probably has two reasons: (1) the inconsistent management practices. Due to different varieties, planting and harvesting dates are not as fixed as for the other crops in this study; (2) the characteristics of potato fields in this region. Potatoes are grown by digging long hilly rows. Theoretically, the measured SAR backscatter values vary depending on the orientation of the rows toward the SAR sensor. Lowering the accuracy variation requires more training fields and a higher temporal resolution, which would allow all row-sensor orientations and the different management practices to be covered.

The two multitemporal approaches of this study both resulted in higher classification accuracies than the single-date classification. While a slightly higher accuracy was achieved using the RF classification of all input bands, the production rules had a lower variance of accuracies and a better runtime. Both approaches benefitted from the MDA as the acquisition dates were chosen according to the principles of AWs during the growing season, based on the crop-specific phenology. The findings from the knowledge-based approach are also crucial for improving accuracy in the future and finding the reasons for non-optimal results. Consequently, the RF approach with all input bands and the integration of expert knowledge on crop phenology are promising ways to obtain parcel-based crop maps from multitemporal TerraSAR-X acquisitions, without the cloud-free limitations of optical data.

5.6.3 Objective III: fusion of the SAR classifications with external geodata to produce crop type enriched LULC maps

The fusion of the final classifications with the external geodata ATKIS and PB prevented possible confusion with all non-crops classes, such as urban, forest, streets, and grassland. The missing information about annually grown crops is retrieved from the remote sensing data. The combination allows the production of enhanced LULC maps, as shown in Figure 5.5. Additionally, the high spatial accuracy of both the TerraSAR-X data and the external geodata made any orthorectification obsolete, which enhances the quality of the final maps and improves the efficiency of their creation.

5.6.4 Study results in an operationalization context

Compared to other studies (e.g. Bargiel (2017)), fewer reference fields were used in this study. The reduction is useful as it reduces the costs of surveys on the ground. However, the identification of various classes, such as the potato in this study, is less accurate, and the variance of the accuracy is greater depending on which fields are taken for training the classifier. Contrariwise, the eight rapeseed fields in this study were found to suffice as the 10 repetitions revealed a high accuracy, but more importantly, a low accuracy variance. These results show that the amount of training data needed strongly depends on the class being observed. However, in an operational context, to calculate the high costs of field surveys, it would be essential to know beforehand the exact amount of ground data needed. This knowledge could be gained, e.g. through an optimization approach, such as that presented by Mathur & Foody (2008).

A shortcoming in an operationalization context is the problem of transferability to another region, which is also reported by Siachalou et al. (2015). As the AWs for crop classification are regionally specific and climate dependent, they would have to be adapted to the crop management practices and phenology of other regions. However, even

regions with similar climates have a high variation in crop productivity (Godfray et al. 2010). An elegant way of dealing with regional heterogeneity has been implemented by Homer et al. (2004), who used the concept of mapping zone delineation in combination with optical remote sensing and ancillary geodata to provide land cover for the whole of the US.

As in Homer et al. (2004), the integrating of external geodata is mainly country-specific; the DLM used in this study is, in this form, only available for Germany. However, the PB data is part of LPIS, which is available in a similar form for the whole EU. The most prominent worldwide dataset is the OpenStreetMap (OSM), which is freely available and could also be used to identify the non-agricultural areas. This use is demonstrated by Immitzer et al. (2016), who combine OSM data with CORINE land cover data (Büttner et al. 2004). However, the spatial accuracy and quality of OSM data depends on the volunteers collecting the data and is worse than that of the datasets used in the present study (Zhang & Malczewski 2017).

5.7 Conclusion

This study demonstrates how multitemporal and dual-polarimetric TerraSAR-X images can be incorporated into the MDA to produce annually updated crop type enriched LULC maps for a subset of the Rur area in Germany. Identification of optimal acquisition time frames to classify the crops revealed similarities to optical remote sensing but enabled future acquisition plans to be improved since radar remote sensing is independent of clouds and thus more reliable. High-classification accuracies were achieved for the classes rapeseed, potatoes, and winter cereals, with no major difference between the two multitemporal approaches used in this study. For the fusion with the external geodata, the high geometric accuracy of TerraSAR-X proved helpful. No manual orthorectification had to be performed for the fusion with the highly accurate ATKIS and PB data.

One particularity of the study was a limited number of reference fields. Repeating all classifications 10 times with different training and validation combinations revealed the variances of the accuracy of the mapped classes. For the class potato, a high variance was found, which suggests that more potato reference fields will be needed in future studies. For the class rapeseed, eight fields were enough to provide high accuracy and almost no variance.

Future research should be done on how to incorporate more SAR data from different viewing angles, polarizations, and other missions into the MDA. One such mission is Sentinel-1 with a higher temporal resolution and wider coverage (Bargiel 2017; Lussem et al. 2016).

5.8 Acknowledgements

TerraSAR-X data were acquired under the proposal no. LAN2156: Potential of TerraSAR-X for agriculture monitoring. The authors gratefully acknowledge financial support by the CRC/TR32 "Patterns in Soil-Vegetation-Atmosphere Systems: Monitoring, Modelling, and Data Assimilation" funded by the German Research Foundation (DFG).

5.9 References

Arbeitsgemeinschaft der Vermessungsverwaltungen (AdV), 2006. Documentation on the Modelling of Geoinformation of Official Surveying and Mapping (GeoInfoDok) - Chapter 5 - Technical applications of the basic schema - Section 5.4 - Explanations on ATKIS®, Version 5.1, Status 31 July 2006. http://www.adv-online.de/AAA-Modell/Dokumente-der-GeoInfoDok/binarywriterservlet?imgUid=8df46f15-1ff9-f216-afd6-ff3072e13d63&uBasVariant=11111111-1111-1111-1111-111111111111&isDownload=true, 2016-10-12.

Atzberger, C., 2013. Advances in remote sensing of agriculture: Context description, existing operational monitoring systems and major information needs. Remote Sensing 5(2), 949–981.

Bareth, G., 2008. Multi-Data Approach (MDA) for enhanced land use and land cover mapping. ISPRS Archives Vol. XXXVII. Part B8 Proceedings of the XXI ISPRS Congress, 3-11 July, 2008, Beijing, China, 1059–1066.

Bargiel, D., 2017. A new method for crop classification combining time series of radar images and crop phenology information. Remote Sensing of Environment 198, 369–383.

Bauer, M. E., Davis, B., Hixson, M., 1978. Area estimation of crops by digital analysis of Landsat data. Photogrammetric Engineering and Remote Sensing 44, 1033–1043.

Bhang, K., Schwartz, F., Braun, A., 2007. Verification of the vertical error in C-band SRTM DEM using ICESat and Landsat-7, Otter Tail County, MN. IEEE Transactions on Geoscience and Remote Sensing 45, 36–44.

Blaes, X., Vanhalle, L., Defourny, P., 2005. Efficiency of crop identification based on optical and SAR image time series. Remote Sensing of Environment 96(3-4), 352–365.

Breit, H., Fritz, T., Balss, U., Lachaise, M., Niedermeier, A., Vonavka, M., 2010. TerraSAR-X SAR processing and products. Geoscience and Remote Sensing, IEEE Transactions on 48(2), 727–740.

Brisco, B., Li, K., Tedford, B., Charbonneau, F., Yun, S., Murnaghan, K., 2013. Compact polarimetry assessment for rice and wetland mapping. International Journal of Remote Sensing 34(6), 1949–1964.

Bush, T., Ulaby, F., 1978. An evaluation of radar as a crop classifier. Remote Sensing of Environment 7(1), 15–36.

Büttner, G., Feranec, J., Jaffrain, G., Mari, L., Maucha, G., Soukup, T., 2004. The CORINE land cover 2000 project. EARSeL eProceedings 3, 331–346.

Cloude, S., Pottier, E., 1997. An entropy based classification scheme for land applications of polarimetric SAR. IEEE Transactions on Geoscience and Remote Sensing 35, 68–78.

Cloude, S. R., Goodenough, D. G., Chen, H., 2012. Compact decomposition theory. IEEE Geoscience and Remote Sensing Letters 9(1), 28–32.

Congalton, R. G. R., 1991. A review of assessing the accuracy of classifications of remotely sensed data. Remote sensing of environment 37(October 1990), 35–46.

Curlander, J., McDonough, R., 1991a. Synthetic Aperture Radar: Systems and Signal Processing. JohnWiley& Sons, New York, USA.

Fieuzal, R., Baup, F., Marais-Sicre, C., 2013. Monitoring wheat and rapeseed by using synchronous optical and radar satellite data—from temporal signatures to crop parameters estimation. Advances in Remote Sensing 2, 162–180.

Foerster, S., Kaden, K., Foerster, M., Itzerott, S., 2012. Crop type mapping using spectral-temporal profiles and phenological information. Computers and Electronics in Agriculture 89, 30–40.

Foody, G., McCulloch, M., Yates, W., 1994. Crop classification from c-band polarimetric radar data. International Journal of Remote Sensing 15, 2871.

Forkuor, G., Conrad, C., Thiel, M., Ullmann, T., Zoungrana, E., 2014. Integration of optical and Synthetic Aperture Radar Imagery for Improving Crop Mapping in Northwestern Benin, West Africa. Remote Sensing 6(7), 6472–6499.

Godfray, H., Beddington, J., Crute, I., Haddad, L., Lawrence, D., Muir, J., Toulmin, C., 2010. Food security: The challenge of feeding 9 billion people. Science 327.

Homer, C., Huang, C., Yang, L., Wylie, B., Coan, M., 2004. Development of a 2001 national land-cover database for the United States. Photogrammetric Engineering & Remote Sensing 70, 829.

Hoogeboom, P., 1983. Classification of Agricultural Crops in Radar Images. IEEE Transactions on Geoscience and Remote Sensing GE-21(3), 329–336. issn: 0196-2892.

Horning, N., 2013. *RandomForestClassification*. https://www.bitbucket.org/rsbiodiv/randomforestclassification/commits/534bc2f, 2019-1-5.

Hütt, C., Tilly, N., Schiedung, H., Bareth, G., 2016. Potential of multitemporal tandem-x derived crop surface models for maize growth monitoring. International Archives of the Photogrammetry, Remote Sensing and Spatial Information Sciences - ISPRS Archives 41, 803.

Hütt, C., Koppe, W., Miao, Y., Bareth, G., 2016. Best Accuracy Land Use/Land Cover (LULC) Classification to Derive Crop Types Using Multitemporal, Multisensor, and Multi-Polarization SAR Satellite Images. Remote Sensing 8(8, 684).

Immitzer, M., Vuolo, F., Atzberger, C., 2016. First experience with Sentinel-2 data for crop and tree species classifications in central Europe. Remote Sensing 8(3, 166), 1–27.

IT.NRW, 2016. Landwirtschaftszählung in Nordrhein- Westfalen 2010 - Gemeinde- und Kreisstatistik der land- wirtschaftlichen Betriebe Betriebsgrößen, Bodennutzung, Viehhaltung, sozialökonomische Betriebstypen, betriebs- wirtschaftliche Ausrichtung, Arbeitskräfte. https://www.destatis.de/GPStatistik/servlets/MCRFileNodeServlet/NWHeft_derivate_00006831/C913201051_A.pdf, 2016-10-12.

Jarvis, A., Reuter, H. I., Nelson, A., Guevara, E., 2016. Hole-filled SRTM for the globe Version 4, available from the CGIAR-CSI SRTM 90m Database. http://srtm.csi.cgiar.org, 2018-10-22.

Koppe, W., Gnyp, M. L., Hütt, C., Yao, Y., Miao, Y., Chen, X., Bareth, G., 2013. Rice monitoring with multi-temporal and dual-polarimetric terrasar-X data. International Journal of Applied Earth Observation and Geoinformation 21(1), 568–576.

Landwirtschaftskammer, NRW, 2011. LZ Rheinland - Ratgeber Förderung 2011. Rheinischer Landwirtschafts- Verlag GmbH, Bonn, Germany.

Landwirtschaftskammer, NRW (LWK-NRW), 2016. Bestellung von digitalen Feldblockgeometrien. http://www.lwk.nrw.de/foerderung/feldblock/angebot/bestellen.htm, 2016-11-1.

Liaw, A., Wiener, M., 2002. Classification and Regression by randomForest. R News 2(3), 18–22.

Lopez-Sanchez, J., Cloude, S., Ballester-Berman, J., 2012. Rice phenology monitoring by means of SAR polarimetry at X-band. IEEE Transactions on Geoscience and Remote Sensing 50, 2695.

Lu, D., Weng, Q., 2007. A survey of image classification methods and techniques for improving classification performance. International Journal of Remote Sensing 28, 823.

Lussem, U., Hütt, C., Waldhoff, G., 2016. Combined analysis of Sentinel-1 and RapidEye data for improved crop type classification: An early season approach for rapeseed and cereals. International Archives of the Photogrammetry, Remote Sensing and Spatial Information Sciences - ISPRS Archives 41, 959.

Lussem, U., Waldhoff, G., 2014. Enhanced land use classification 2014 of the Rur catchment - Update, CRC/TR32 Database (TR32DB). http://tr32db.uni-koeln.de/data.php?dataID=1142, 2017-12-11.

Mathur, A., Foody, G., 2008. Crop classification by support vector machine with intelligently selected training data for an operational application. International Journal of Remote Sensing 29, 2227.

McNairn, H., Kross, A., Lapen, D., Caves, R., Shang, J., 2014. Early season monitoring of corn and soybeans with TerraSAR-X and RADARSAT-2. International Journal of Applied Earth Observation and Geoinformation 28, 252–259.

McNairn, H., Champagne, C., Shang, J., Holmstrom, D., Reichert, G., 2009. Integration of optical and Synthetic Aperture Radar (SAR) imagery for delivering operational annual crop inventories. ISPRS Journal of Photogrammetry and Remote Sensing 64, 434–449.

McNairn, H., Shang, J., 2016. A review of multitemporal synthetic aperture radar (SAR) for crop monitoring. In: Ban, Y. (Ed.), Multitemporal Remote Sensing. Springer, 317–340.

Nonaka, T., Ishizuka, Y., Yamane, N., Shibayama, T., Takagishi, S., Sasagawa, T., 2008. Evaluation of the geometric accuracy

of TerraSAR-X. International Archives of the Photogrammetry, 135–140.

Oetter, D., Cohen, W., Berterretche, M., Maiersperger, T., Kennedy, R., 2001. Land cover mapping in an agricultural setting using multiseasonal Thematic Mapper data. Remote Sensing of Environment 76, 139.

Ok, A. O., Akar, O., Gungor, O., 2012. Evaluation of random forest method for agricultural crop classification. European Journal of Remote Sensing 45(3), 421.

Reichenau, T., Korres, W., Montzka, C., Fiener, P., Wilken, F., Stadler, A., Schneider, K., 2016. Spatial heterogeneity of leaf area index (LAI) and its temporal course on arable land: combining field measurements, remote sensing and simulation in a comprehensive data analysis approach (CDAA). Plos One 11, 1–24.

Siachalou, S., Mallinis, G., Tsakiri-Strati, M., 2015. A hidden markov models approach for crop classification: Linking crop phenology to time series of multi-sensor remote sensing data. Remote Sensing 7, 3633.

Simmer, C., Thiele-Eich, I., Masbou, M., Amelung, W., Bogena, H., Crewell, S., Zerenner, T., 2015. Monitoring and modeling the terrestrial system from pores to catchments: The transregional collaborative research center on patterns in the soil–vegetation–atmosphere system. Bulletin of the American Meteorological Society 96, 1765.

Simonett, D. S., 1967. The Potential of Radar as a Remote Sensor in Agriculture: 1. a Study with K-band Imagery in Western Kansas. University of Kansas, Center for Research Incorporated, Engineering Science Division, Lawrence, Kansas, USA.

Skriver, H., 2012. Crop classification by multitemporal C- and L-band single- and dual-polarization and fully polarimetric SAR. IEEE Transactions on Geoscience and Remote Sensing 50, 2138.

Skriver, H., Svendsen, M., Thomsen, A., 1999. Multitemporal C- and L-band polarimetric signatures of crops. IEEE Transactions on Geoscience and Remote Sensing 37, 2413.

Smith, G., Fuller, R., 2001. An integrated approach to land cover classification: An example in the Island of Jersey. International Journal of Remote Sensing 22, 3123.

Sonobe, R., Tani, H., Wang, X., Kobayashi, N., Shimamura, H., 2014. Random forest classification of crop type using multi-temporal TerraSAR-X dual-polarimetric data. Remote Sensing Letters 5(2), 157–164.

Tatsumi, K., Yamashiki, Y., Canales Torres, M., Taipe, C., 2015. Crop classification of upland fields using random forest of time-series Landsat 7 ETM+ data. Computers and Electronics in Agriculture 115, 171.

Van Niel, T., McVicar, T., 2004a. Determining temporal windows for crop discrimination with remote sensing: A case study in south-eastern Australia. Computers and Electronics in Agriculture 45, 91.

Vinciková, H., Hais, M., Brom, J., Procházka, J., Pecharová, E., 2010. Landscape studies use of remote sensing methods in studying agricultural landscapes – A review. Journal of Landscape Studies 3, 53.

Waldhoff, G., Curdt, C., Hoffmeister, D., Bareth, G., 2012. Analysis of multitemporal and multisensor remote sensing data for crop rotation mapping. ISPRS International Archives of the Photogrammetry, Remote Sensing and Spatial Information Sciences, I-7, 177–182.

Waldhoff, G., 2014. Multidaten-Ansatz zur fernerkundungs-und GIS-basierten Erzeugung multitemporaler, disaggregierter Landnutzungsdaten. Methodenentwicklung und Fruchtfolgenableitung am Beispiel des Rureinzugsgebiets. PhD thesis, Universität zu Köln.

Waldhoff, G., Bareth, G., 2009. GIS-and RS-based land use and land cover analysis: case study Rur-Watershed, Germany. Geoinformatics 2008 and Joint Conference on GIS and Built environment: Advanced Spatial Data Models and Analyses, International Society for Optics and Photonics.

Waldhoff, G., Lussem, U., Bareth, G., 2017. Multi-Data Approach for remote sensing-based regional crop rotation mapping: A

case study for the Rur catchment, Germany. International Journal of Applied Earth Observation and Geoinformation 61, 55–69.

Whitcraft, A., Vermote, E., Becker-Reshef, I., Justice, C., 2015. Cloud cover throughout the agricultural growing season: Impacts on passive optical earth observations. Remote Sensing of Environment 156, 438–447.

Zhang, H., Malczewski, J., 2017. Quality Evaluation of Volunteered Geographic Information: The Case of OpenStreetMap. In: Volunteered Geographic Information and the Future of Geospatial Data. IGI Global, Hershey, PA, USA, 19–46.

Zhao, Q., Lenz-Wiedemann, V., Yuan, F., Jiang, R., Miao, Y., Zhang, F., Bareth, G., 2015. Investigating within-field variability of rice from high resolution satellite imagery in Qixing Farm County, Northeast China. ISPRS International Journal of Geo-Information 4, 236.

6 An Open Data and Open Source Approach for Crop Type Mapping with Sentinel-1 SAR Satellite Images, Geodata from Open.NRW, and FOSS

Christoph Hütt[1], Guido Waldhoff[1], Georg Bareth[1]
Submitted to Photogrammetry Fernerkundung Geometrie
Original manuscript is embedded in dissertation format.

1. Institute of Geography, GIS & Remote Sensing Group, University of Cologne, Cologne, Germany,
e-mail: {christoph.huett} {guido.waldhoff} {g.bareth} @uni-koeln.de

6.1 Abstract

Accurate crop type maps are urgently needed as input data for various applications, leading to improved planning and more sustainable use of resources. Satellite remote sensing is the optimal tool to provide such data. However, the commonly used optical remote sensing approaches are unreliable as they only work under cloud-free conditions. Unfortunately, using the more reliable source of information from

microwave images is more complicated, although SAR sensors have development potential. Dealing with such a complexity urges current studies to be reproducible, open, and built upon Free and Open-Source Software (FOSS). This paper presents a case study of crop classification from microwave remote sensing relying on open data and open software only. We used multitemporal microwave remote sensing images from ESA's Sentinel-1 satellites and enriched the result with data from open.NRW. All software used in this study is open-source, such as the Sentinel Application Toolbox (SNAP), Orfeo Toolbox, R, and QGIS. Validation using an independent validation data set showed a high overall accuracy of 96.7 % with differentiation into 11 different crop-classes. All results are reproducible without further data or software costs as all input and output data are available in a repository as open data.

6.2 Introduction

Global food insecurity is on the rise again (FAO et al. 2017). Current and future challenges evolve from a growing world population with an increasing nutrition demand under climate change conditions (FAO 2017). Therefore, Godfray & Garnett (2014) demand a higher crop yield from agricultural production. To achieve this efficiency increase, the decision-makers in this domain can use information from agricultural monitoring systems based on satellite remote sensing data (Atzberger 2013).

However, Fritz et al. (2018) identify crop type maps as one missing, yet essential part of the current global systems. In addition, spatial crop type data is critical for modeling matter fluxes in soil-vegetation-atmosphere systems (Bareth 2009). While, on a local scale, crop type information is needed and available for agricultural management decisions (e.g. Machwitz et al. 2018), on regional, national, or continental scales, such crop type data is missing (Xiong et al. 2017), especially on an annual basis. This data gap causes issues not only for modeling agroecosystems (Kersebaum et al. 2007) but also for

decision-makers.

Delimiting crop type is a special kind of LULC classification. LULC can be efficiently derived by satellite remote sensing (Anderson et al. 1976; Xie et al. 2008; Jensen 2009), which provides continues monitoring of the earth's surface over extended areas at a comparably low cost. Separating crop types with remote sensing images is achieved using the crop specific reflection in multitemporal images. By considering the phenology of the plants under investigation, time frames can be identified where each crop type is more easily distinguishable from the others. The topic is being researched using improved sensors (Vuolo et al. 2018) and algorithms (Waldhoff et al. 2017; Sonobe et al. 2014). One recent approach classifies the crops without needing annual training data (Heupel et al. 2018), which is typically gathered by conducting field surveys each year to train the classifiers.

However, optical approaches are unreliable for acquiring data of a distinct phenological stage, as clouds during image acquisition hamper successful analysis (Whitcraft et al. 2015; Waldhoff et al. 2017). The mandatory multitemporal measurement is then sometimes impossible, resulting in degraded map accuracy. For cloudy conditions, Synthetic Aperture Radar (SAR) systems are a solution as they make crop classification approaches more reliable in cloudy areas (McNairn & Shang 2016; Hütt, Koppe, et al. 2016; Hütt & Waldhoff 2018; Bargiel 2017; Kenduiywo et al. 2018; Whelen & Siqueira 2018). For our AOI, although combining multiple optical satellite imaging systems, Waldhoff et al. (2017) report that no cloud-free remote sensing image was available for a seven year period. Unsurprisingly, the optical Sentinel-2 collected no cloud-free image over our AOI during the observation period (January-September 2017) of this study.

Interestingly, Schmullius et al. (2015) state that operational microwave applications are limited, providing as reasons the complexity of the radar signal and limited radar sensor capabilities. Furthermore, studies on the topic of crop type classification from SAR are not reproducible, as data restrictions lead to the input data not being available. Fritz et al. (2018) conclude that the lack of such data for calibration purposes is the primary constraint to operationalizing agricultural

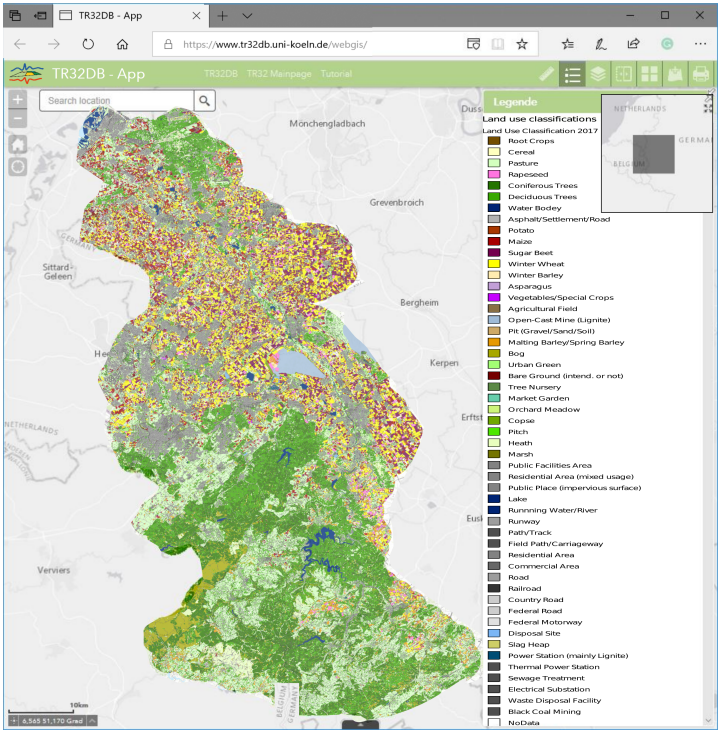

Figure 6.1: Location of the study region Rur Catchment and LULC analysis of 2017 using the MDA (Waldhoff et al. 2017) with optical satellite data and external data. Screenshot from the online available WebGIS of the TR32DB.

monitoring systems. In a more general context, transparency and openness are demanded by the Transparency and Openness Promotion (TOP) (Nosek et al. 2015; McNutt 2016).

More challenges in LULC analysis come from using proprietary software, which is expensive and the source code cannot be examined

or improved by others. FOSS works differently: The code is available online, and no costs are incurred when using, changing, or redistributing the software (Steiniger & Hunter 2013). In a different domain, Rocchini et al. (2017) have already shown how using FOSS helps to achieve reproducibility of remote sensing studies.

Additionally, remote sensing data analysis, including official geodata for creating LULC maps has proven beneficial. The MDA (Bareth 2008) has been proposed as a framework for fusing multitemporal satellite images and official geodata for LULC mapping. The concept has been adopted to crop type classifications using optical (Waldhoff et al. 2017) and to microwave (Hütt & Waldhoff 2018) satellite images. Such official geodata on, e.g., topography has recently been released as open data obtained by surveying and mapping authority of the German state NRW, which includes our AOI. Among other datasets, the program open.NRW provides the complete real estate register, with the geometry of every property (Waldhoff et al. 2015). A highly accurate DEM is also provided. Both open.NRW datasets are ideal for integration into the workflow of crop type classification from radar satellite remote sensing.

The availability of open microwave satellite imagery, FOSS for LULC analysis, and open geodata from official sources for the MDA creates new research opportunities. Therefore, the overall objective of this study was the development and implementation of an open remote sensing analysis workflow with open data and FOSS for crop type mapping on the field level for national scales. As a first step, we focused on a region in western Germany, the Rur Catchment, to develop, implement, and validate such an open data analysis workflow. The Rur Catchment is the study region of the DFG-funded CRC/TR32 "Patterns in Soil-Vegetation-Atmosphere Systems: Monitoring, Modelling, and Data Assimilation" (Fig. 6.1). Within the TR32 research activities, multiannual LULC data including crop types were produced (Fig. 6.1) and have been available via the TR32 project database (TR32DB) since 2008 (Curdt & Hoffmeister 2015).

The present study used open remote sensing data from the AOI satellite Sentinel-1, and external data from open.NRW to perform a

LULC crop type classification. We designed the whole workflow using FOSS to follow the demands of TOP. The used data models, all input, and the output data, including the labeled reference data set from our mapping campaign, are shared openly in a scientific data repository, the TR32DB. This combination allows others to access, use, change, evaluate, reproduce, and even refine or improve the present study's outcomes.

6.3 Study Site and Data

6.3.1 Rur Catchment

This study was performed within the collaborative research project TR32. The project has a defined study area, situated at the German borders with Belgium and the Netherlands (compare Fig 6.1). For the present study, only those parts that lie within the German borders were considered. The extent of the area is about 2500 km^2. The area is characterized by fertile loess soils and humid, temperate climate. It is intensively used for agricultural production. Waldhoff et al. (2017) describe the study area in detail.

6.3.2 Sentinel-1 Open SAR data

The positive effects of open data have been seen by the remote sensing community, as the opening of the optical Landsat archive in 2008 by the USGS Landsat (Woodcock et al. 2008) had a positive impact on how satellites images are used for scientific purposes (Wulder et al. 2012). Consequently, the prominent statement from Wulder & Coops (2014) was to "Make Earth observations open access." The ESA followed the USGS example by distributing all satellite observations of their current satellite program Copernicus Sentinel as open data (ESA 2013). Hence, the Sentinel-1 radar satellite, which was used in the present study, is the first operational radar satellite, with an open data policy.

The two Sentinel-1 AOI satellites work in a constellation to provide a repeat cycle of six days for the same imaging properties. The revisit time for different image properties is shorter and varies depending on the geographic location. Over land, the satellites monitor continuously with a spatial resolution of 5 m x 20 m (Torres et al. 2012).

For this study, we acquired 70 Sentinel-1 images, for the growing period of 2017, between January and August. As can be seen in Table 6.1, the images are two time series from the relative orbits 88 and 37. Only the images covering the entire AOI of approx 2500 km^2 were considered. Table 6.2 shows the individual acquisition dates. Notably, the two chosen relative orbits from the two satellites offer at least one image acquisition per week. Even more images would be available that only partly cover the AOI.

The Sentinel-1 SAR images were downloaded from ESA's Scihub in prepossessed Ground Range Detected (GRD)form. The advantage of this server-side preprocessing is smaller download sizes and reduced speckle. The disadvantages are a decreased spatial resolution and losing the phase information, which are used for SAR interferometry and polarimetry (Torres et al. 2012). As the Sentinel-1 images are provided with high geometric accuracy (Schubert et al. 2015) a multitemporal image classification is possible without further coregistration. All used Sentinel-1 scenes can be downloaded from the TR32DB (Copernicus 2018a; Copernicus 2018c; Copernicus 2018b; Copernicus 2018d).

relative orbit	orbit direction	time (UTC) of acquisition	number of acquisitons	Polarisations	Incidence Angle over AOI
88	Ascending	17:24	39	VV/VH	38.4° - 41.2°
37	Descending	8:12	31	VV/VH	33.2° - 37.6°

Table 6.1: Metadata of the Sentinel-1, A and B, acquisitions used in this study

			Jan.				Feb.				Mar.				Apr.				May				June				July				Aug.			
cal. week			1	2	3	4	5	6	7	8	9	10	11	12	13	14	15	16	17	18	19	20	21	22	23	24	25	26	27	28	29	30	31	32	33	34	35
rel. orbit	39	S1a	★	★		★		★			★		★		★	★		★		★	★															
		S1b	★		★	★			★	★		★		★	★		★		★		★	★		★		★	★		★		★	★			★	
	88	S1a	★		★	★		★		★		★	★			★		★	★		★		★	★	★				★	★		★		★	★	★
		S1b		★		★	★		★		★	★		★		★		★	★		★		★	★		★		★		★	★				★	★	

Table 6.2: Sentinel-1A (S1a) and Sentinel-1b (S1b) acquisitions of the study period, each acquisition covers the whole AOI. As can be seen, there is at least one acquisition for each week.

6.3.3 Crop Distribution Mapping of 2017

Over 1200 agricultural fields were visited and mapped in a ground survey campaign (Waldhoff & Herbrecht 2018a). After transferring the mapping results to the GIS environment, the areas were checked for plausibility using the remote sensing Sentinel-1 datasets described above. To exclude the edges, an inner buffer of 20 m was applied, and only fields within the AOI were used. Detailed information on the area statistics of the final 775 fields that were used for the present study can be found in Table 6.3. Besides the typical crops of the region such as maize, sugar beet, rapeseed, potato, wheat, and pasture, we found 19 pea and eight carrot fields. Consequently, we additionally included those crops in our classification scheme.

The consequent division into independent training and validation fields was obtained by sorting the fields by crop type and field size. The fields were then alternately assigned to independent validation and training datasets, starting with validation. Consequently, the tallest field per crop was always chosen for validation. Hence, the resulting area statistics are slightly higher for the validation fields.

All data from the ground campaign (Waldhoff & Herbrecht 2018a) and the pre-processed independent training and validation datasets (Hütt 2018) are distributed under an open data policy via the TR32DB.

Crop Type	Number of Fields			Area (ha)			Number of Pixels (10x10m)			Mean Field Size (ha)
	Tot.	Train.	Val.	Tot.	Train.	Val.	Tot.	Train.	Val.	
Maize	75	37	38	205	98	107	20,490	9,763	10,727	2.73
Sugar Beet	108	54	54	364	177	188	36,422	17,660	18,762	3.37
Barley	206	103	103	600	296	304	60,005	29,626	30,379	2.91
Wheat	87	43	44	279	134	146	27,937	13,351	14,586	3.21
Rye	51	25	26	113	54	59	11,331	5,389	5,942	2.22
Spring Barley	51	25	26	103	49	54	10,309	4,924	5,384	2.02
Pasture	82	41	41	147	69	78	14,696	6,907	7,789	1.79
Rapeseed	72	36	36	220	105	115	21,953	10,471	11,482	3.05
Potato	16	8	8	73	34	39	7,305	3,365	3,940	4.57
Pea	19	9	10	58	27	31	5,848	2,740	3,108	3.08
Carrot	8	4	4	56	25	31	5,623	2,499	3,124	7.03
Total	775	385	390	2219	1067	1152	221,919	106,695	115,224	2.86

Table 6.3: Collected field data of crop distribution during the growing season 2017

6.3.4 Authorative official data from Open.NRW

For preprocessing of remote sensing data, and SAR data in particular, using a DEM is advised (Jensen 2009). In this study, we used the high resolution, high precision, openly available elevation data from open.NRW. The DEM is produced from LIDAR data with a point density of at least 4 points per m^2 and updated every six years. The final spatial resolution of 1 m has an absolute height error of less than 40 cm in most areas (Bezirksregierung Köln 2018a). The newest version of the DEM can be found online (Bezirksregierung Köln 2018a), and a preprocessed version over the AOI of the DEM can be acquired via the TR32DB (Bezirksregierung Köln 2017). For compatibility reasons with the radar processing software SNAP the DEM was projected to WGS84 and the spatial resolution reduced to 5 m (Hütt 2018c).

For the delineation of the arable land, we exploited the real estate register German Authoritative Real Estate Cadastre Information System (ALKIS), which is freely available for the state Northrhinewestfalia (NRW) from Open.NRW Bezirksregierung Köln 2018b. The register contains, besides other information, the primary usage of each

of the 9 million property parcels in NRW. In our case, only parcels that have "agricultural land" as their primary usage were selected and used as a crop mask (Hütt 2018b).

6.4 Methods

6.4.1 Preprocessing of the Sentinel-1 Radar data using the SNAP toolbox

The preprocessed GRD images were individually processed using the SNAP Toolbox SNAP-ESA 2017. The following tools were executed on each acquisition:

1. As a first step, a subset of the images was calculated by cropping the images to the extent of the AOI.

2. To enhance the geometric accuracy, the precise orbit files were auto-downloaded from the ESA server and applied to the images. The precise orbit files are calculated within two weeks after the image acquisition and significantly enhance the geometric accuracy of the Sentinel-1 images.

3. Next, the images were converted to beta0, which is the measured radar brightness (Small 2011), and a prerequisite for the next step.

4. The highly accurate DEM from Open.NRW was used to perform a Radiometric Terrain Correction to gamma0. Thereby, based on the DEM, the terrain-induced radiometric effects are eliminated, and the signal is normalized for the local illuminated area (Small 2011).

5. All SAR images inherit a salt-and-pepper-like noise (Curlander & McDonough 1991a). A Gamma Map Speckle Filter with a 3x3 moving window was applied to reduce it.

6. To project the images from slant range to ground range, a Range Doppler Terrain Correction was performed using the DEM from Open.NRW. (Curlander & McDonough 1991a). Notably, a higher accuracy of the DEM translates into a higher horizontal accuracy of the projected image. The DEM resampling was set to Bicubic Interpolation, while the image resampling was performed with nearest-neighbor resampling to avoid unnecessary mixing with neighboring pixels. The final pixel spacing was set to 10 m, and the reference system is UTM 32 N with WGS 84 as the reference ellipsoid.

7. For a better data handling, conversion of the raster values from linear to dB was applied.

8. To reduce the amount of disc space being used for the images and to accelerate classification, the pixel-depth was reduced to unsigned integer with a linear scaling using slope and intercept of the histogram.

The graph to apply those steps in the SNAP software (Hütt 2018d), and the final stacked image composite (Hütt 2018e) can be downloaded via the TR32DB.

6.4.2 Supervised Random Forest Classification

The 70 individual Sentinel-1 images were stacked, and a supervised pixel-based classification was performed using the independent training data from the mapping campaign. The Random Forest (RF) algorithm was used as the classifier, as it had already proved beneficial in other SAR-based crop classification scenarios (Hütt, Koppe, et al. 2016; Hütt & Waldhoff 2018; Sonobe et al. 2014). The advantages of the RF classifier are its capabilities to handle high dimensional data and the ability to work without normally distributed data. While there are more advanced algorithms such as the one developed by Bargiel (2017), previous studies have found the RF classifier to be highly accurate (Rodriguez-Galiano et al. 2012).

Validation of the gained classifications was conducted using the fields from the mapping campaign that had not been used for training the classifier. The resultant error matrix is the basis for the accuracy measures such as the user's and the producer's accuracy, but also the general accuracy indicator - the overall accuracy (Congalton & Green 2008).

6.4.3 Real estate cadastre and post-classification filtering

Deploying the ALKIS real estate cadastre for delineation of the cropland enabled all non-crop pixels to be removed. Only after that step is a post-classification filter reasonable. Otherwise, non-crop pixels would be considered in the filtering process, possibly degrading the classification quality. We used a majority filter with a ball-shaped structuring element, setting the center pixel to the majority value of the pixel values within the ball (Orfeo Developement Team 2018). The filtering was conducted twice: the first one with a ball radius of three pixels, the second one with two pixels.

6.4.4 Open Source Software used in this study

One of the principles of the present study was to rely solely on Open Source Software. Preprocessing of the radar images was conducted using the Sentinel Application Toolbox (SNAP) (SNAP-ESA 2017). The actual multitemporal random forest classification was performed in R (R Core Team 2018) (Version 3.4.3) using a freely available R-script (R Core Team 2018) from (Horning 2013) that uses the following R-packages: randomforest (Liaw & Wiener 2002), GDAL (Bivand et al. 2017), Raster (Hijmans 2017), Maptools (Bivand & Lewin-Koh 2017), and SP (Pebesma & Bivand 2005). For postprocessing including the Error Matrix generation and the post classification filter, we used the Orfeo Toolbox (Orfeo Developement Team 2017). Map-making, integration of the ALKIS, cropping of the raster data, and preprocessing of the crop distribution maps

was conducted in QGIS (QGIS Development Team 2017). The ALKIS data was imported to a PostGIS (PostGIS 2017) geospatial database, which is based on PostgreSQL (PostgreSQL 2017), using the free software ALKISimport (NorGIS 2017). The preprocessing of the DEM was achieved with GDAL (GDAL Development Team 2017).

6.5 Results

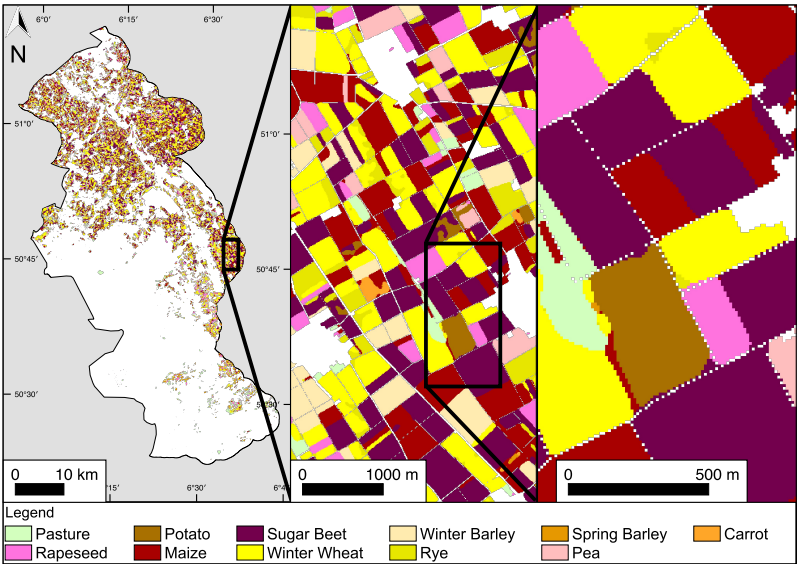

Figure 6.2: Final Classification with a two times post classification majority filter of the whole AOI covering about 2500 km^2

Using the proposed approach made it possible to classify 11 different crops with an accuracy of around 95 %. The final crop classification map is presented in Figure 6.2. It covers the entire 2500 km^2 of the

		Validation (Ground Data)											User's Accuracy
		Pasture	Rape seed	Potato	Maize	Sugar Beet	Barley	Wheat	Rye	Spring Barley	Pea	Carrot	
Classification Data	Pasture	**3093**	0	0	0	0	116	0	0	25	3	0	**96%**
	Rapeseed	6	**11045**	0	0	0	3	0	0	0	0	0	**100%**
	Potato	0	0	**2845**	0	0	0	0	0	0	0	0	**100%**
	Maize	314	0	2	**10826**	93	35	3	1	0	6	81	**95%**
	Sugar Beet	32	0	1096	9	**18667**	2	10	1	0	0	0	**94%**
	Barley	49	0	0	0	0	**27979**	3	247	7	0	0	**99%**
	Wheat	40	0	0	0	0	4	**14345**	2	0	0	0	**100%**
	Rye	8	0	1	0	0	1228	2	**5585**	0	0	0	**82%**
	Spring Barley	7	0	0	0	0	135	0	0	**4855**	0	0	**97%**
	Pea	29	0	0	0	0	0	0	0	0	**3105**	0	**99%**
	Carrot	0	0	0	0	0	1	0	0	0	0	**2967**	**100%**
Producer's Accuracy		**86%**	**100%**	**72%**	**100%**	**100%**	**95%**	**100%**	**96%**	**99%**	**100%**	**97%**	

Table 6.4: Error Matrix of the open data MDA classification shown in Figure 6.2, Overall Accuracy: 96.669%

AOI at a spatial resolution of 10 m. It is available for download in the TR32DB (HÜTT 2018a).

As can be seen in Table 6.4, the accuracy of all crop classes was in the acceptable accuracy range, as all user and producer accuracy measures were beyond 80 %, with one exception: - 72 % producer accuracy of the class potato, which was mixed up with sugar beet.

Integrating the external ALKIS data allowed crop areas to be focused on, as all non-crop areas were masked out. Thereby, applying the two times majority filter became feasible, which resulted in a 1.7 % accuracy gain (Overall Accuracy: 96.69 %). A map of the final classification is shown in 6.2. Although 1.7 % might not seem impressive, the advantages from this procedure go beyond the pure number. Most important, pixels values classified as a crop type and not within the feature class "agricultural land" of ALKIS are deleted, and the correct ALKIS land use class is assigned. Consequently, no agricultural land use is present in the final LULC map.

To follow the principles of TOP, the workflow of the current study was designed and implemented with FOSS. All of the necessary steps to perform the final crop classification could be successfully conducted in the following software environments:

		Validation (Ground Data)									User's Accuracy
		Rape seed	Potato	Maize	Sugar Beet	Barley	Wheat	Summer Crops	Spring Barley	Pea	
Classification Data	Rapeseed	**2655**	0	25	0	255	168	0	53	77	**83%**
	Potato	0	**784**	0	103	0	34	32	0	0	**82%**
	Maize	9	126	**4582**	70	95	0	279	0	2	**89%**
	Sugar Beet	0	79	538	**11265**	7	2	118	0	35	**94%**
	Barley	0	30	21	1	**6681**	319	0	0	0	**95%**
	Wheat	3	51	11	26	120	**13311**	0	8	21	**98%**
	Summer Crops	102	503	291	63	0	1	**4062**	13	116	**79%**
	Spring Barley	3	82	6	0	57	99	195	**1076**	20	**70%**
	Pea	0	0	0	0	0	0	9	0	**988**	**99%**
Producer's Accuracy		**96%**	**47%**	**84%**	**98%**	**93%**	**96%**	**87%**	**94%**	**78%**	

Table 6.5: Error Matrix of the MDA-LULC classification with optical data shown in Fig. 6.1 (Waldhoff & Herbrecht 2018b). The classification was performed using the MDA approach described by Waldhoff et al. (2017), Overall Accuracy: 91.444%

- The Sentinel-1 images were pre-processed in SNAP (SNAP-ESA 2017).
- Transferring the ALKIS into a PostGIS database was performed with ALKISimport (NorGIS 2017).
- Processing of the DEM from open.NRW was done in (GDAL Development Team 2017).
- Performing the random forest classification was executed in R (R Core Team 2018).
- Post classification Filtering and evaluating of the classification was achieved with the Orfeo Toolbox (Orfeo Developement Team 2017).
- Creating the final maps of the classification 6.2 was conducted with QGIS (QGIS Development Team 2017).

6.6 Discussion

This paper presents an open data and open source remote sensing workflow to derive crop type for a region in west Germany, the area of the Rur Catchment. The all-weather capability of the used AOI sensor Sentinel-1 makes the results independent of the cloud coverage that is typical for the study region (Waldhoff et al. 2017). External data in the form of a height model and cadastre data (Waldhoff et al. 2015) assisted the classification process. The final classification of 11 different crops shows a high accuracy of approx. 97 % overall accuracy on a spatial resolution of 10 m.

A comparison with the LULC analysis based on optical data, shown in Fig. 6.1, revealed merely 56 % agreement of the two classifications within the agricultural area. As that dataset is available for download project internally (Waldhoff & Herbrecht 2018b), the differences could be further analyzed:

- 11 % of the differences originate from incomplete disaggregation to the crop level in the optical classification. Merely superior classes such as agricultural field, or summer crop are given.
- Another 10 % stems from the class rye, which is dissolved in the winter wheat class in the optical classification and correctly differentiated in the classification of this study.
- About 9 % difference is due to roads and tracks that are modeled into the optical MDA Classifications (Waldhoff et al. 2017). It is debatable whether that area is representative of the fields in the study area.

Additional to those shortcomings in the optical classification, the error matrix, shown in Table 6.5, reveals more confusion than the one from the current study shown in Table 6.4. Consequently, the overall accuracy is about 5 % lower than that of the present study, although fewer classes were considered. Finally, the spatial resolution is increased from 15 m to 10 m, providing more details of the

crop distribution. In summary, a superiority of the present study's classification can be inferred in almost all aspects.

Another comparison was performed with the results of a recent study by Bargiel (2017). He also used multitemporal Sentinel-1 images to distinguish similar crop types in another study region also situated in Germany. In general, the results of this study are consistent with the study by Bargiel (2017), who concluded that dense time series of SAR images provide a high crop-separation potential. The final crop classifications are not publicly available. Hence, the comparison had to be conducted with the accuracy numbers given in the publication.

Table 6.6 shows the direct comparison of the user and producer accuracies of both studies. The accuaries from Bargiel (2017) are taken from his most sophisticated crop classification, which uses information about the crop's phenology. As can be seen, there is a consistency on the high accuracies of pasture, maize, sugar beet, and wheat. Both studies revealed challenges to correctly classify potatoes, which is probably due to the alignment of the potato hills and various phenology due to varying planting dates (Hütt & Waldhoff 2018). The classes rye, and especially spring barley, was significantly better classified in the present study. This confusion could stem from fewer mapped fields and fewer Sentinel-1 images in the study by Bargiel (2017).

Although the current study's results show less confusion, the algorithm of Bargiel (2017) seems more sophisticated, as it includes crop phenology information. However, it is not possible to compare the algorithms, the input data, or the obtained results as neither the source code nor the data is publicly shared.

That last aspect highlights the innovation of this study, which lies in the unique implementation of the workflow: - All datasets used in the process, provided by ESA and open.NRW, are distributed as open data by the data providers, as well as in the TR32DB. Also, the ground reference of the study, about 1200 labeled agricultural fields, is shared. Furthermore, since the whole workflow is designed with FOSS, there are no additional costs for software and the source code is open. The combination of open data and FOSS allows reproducibility

Crop	Bargiel (2017) Season 1		Bargiel (2017) Season 2		Present Study	
	PA	UA	PA	UA	PA	UA
Pasture	96	89	96	92	86	96
Rapeseed	100	91	100	66	100	99.9
Potato	81	93	75	87	72	100
Maize	96	93	96	89	100	95
Sugar Beet	97	94	89	94	100	94
Barley	96	97	88	56	95	99
Wheat	90	97	88.2	98	100	100
Rye	93	93	89	74	96	82
Spring Barley	74	74	67	96	99	97
Pea	-	-	-	-	100	99
Carrot	-	-	-	-	97	100
Oat	-		43	46	-	
Mean	91.4	91.4	87.2	83.5	94.2	95.8

Table 6.6: Comparison of the Producer's Accuracy (PA) and User's Accuracy (UA) (in %) of crop classes of the study carried out by Bargiel (2017) and of the present study. Unsatisfactory results below 80 % are marked in red (80 - 70 %, 70 - 60 %, below 60 %).

of the study, which enables other scientists to build upon this study's results and evaluate their approaches with our data.

Next, crop type classifications on larger scales are to be pursued and can be integrated into global agricultural systems (Fritz et al. 2018). In doing so, such systems can provide better outputs to enable the principles of agricultural intensification to be following, resulting in lower environmental impacts and higher food security.

However, upscaling the approach brings additional challenges. One is the availability and quality of external data. Geodata is often not available in such high precision as the geodata provided by open.NRW. For DEMs, that problem could be solved by relying on global data sets, such as the TanDEM-X derived DEM (Zink et al. 2014), which has recently been made freely available for scientific purposes in 90 m

resolution. However, releasing the full resolution as open data would be favorable.

In the case of including external cadastre data into the classification process (Waldhoff et al. 2015), a high spatial accuracy cannot be anticipated in many areas of the world. In such cases, Zhao, Hütt, et al. (2015) present a smart way to improve the accuracy of external data, using a composite of multitemporal TerraSAR-X images as a spatial reference. As Sentinel-1 has a similarly high spatial accuracy (Schubert et al. 2015), the approach could be adapted to areas where merely external geodata of lower spatial accuracy is available.

As shown above, the workflow's implementation was performed in 6 different FOSS environments. Each environment has its characteristics, which involves a high demand of technical abilities necessary to execute the whole workflow. One way of coping with that issue is to create comprehensive documentation, user forums, and user mailing lists. It would also be possible to develop new software based on the environments used or to extend existing environments to meet the requirements of AOI-based crop classification in one environment.

6.7 Conclusion

This study demonstrates the feasibility of multitemporal microwave c-band AOI data from Sentinel-1 to distinguish crop types in our study site in western Germany. The final classification was evaluated with high accuracy, which was reached through the innovative integration of publicly available open data from Open.NRW. One of them was the high resolution and high precision DEM, which assisted the SAR preprocessing. The other one was the spatially highly accurate real estate register enabling to exclude the non- and special crop areas using the MDA. To overcome the problem of limited radar applications due to the complexity of radar data, all data used and produced in this study is openly available in the TR32DB. Additionally, the processing was done solely with FOSS. Consequently, all results are reproducible without any additional data or software costs. Hence, the current

study makes a substantial contribution to science in the context of microwave-based crop classification.

6.8 Acknowledgements

The authors gratefully acknowledge financial support by the CRC/TR32 'Patterns in Soil-Vegetation-Atmosphere Systems: Monitoring, Modelling, and Data Assimilation' funded by the German Research Foundation (DFG).

6.9 References

Anderson, J., Hardy, E., Roach, J., Witmer, R., 1976. A land use and land cover classification system for use with remote sensor data. United States Government Printing Office, Washington D.C., USA.

Atzberger, C., 2013. Advances in remote sensing of agriculture: Context description, existing operational monitoring systems and major information needs. Remote Sensing 5(2), 949–981.

Bareth, G., 2008. Multi-Data Approach (MDA) for enhanced land use and land cover mapping. ISPRS Archives Vol. XXXVII. Part B8 Proceedings of the XXI ISPRS Congress, 3-11 July, 2008, Beijing, China, 1059–1066.

Bareth, G., 2009. GIS-and RS-based spatial decision support: structure of a spatial environmental information system (SEIS). International Journal of Digital Earth 2(2), 134–154.

Bargiel, D., 2017. A new method for crop classification combining time series of radar images and crop phenology information. Remote Sensing of Environment 198, 369–383.

Bezirksregierung Köln, 2017. *Digital Elevation Model (DGM1) of the Rur Catchment, based on data from Bezirksregierung Köln, Bonn, Germany. CRC/TR32 Database (TR32DB).* http://www.tr32db.uni-koeln.de/data.php?dataID=1690, 2019-1-5.

Bezirksregierung Köln, 2018a. *Gelaendemodelle*. https://www.bezreg-koeln.nrw.de/brk_internet/geobasis/hoehenmodelle/gelaendemodelle/index.html, 2019-1-5.

Bezirksregierung Köln, 2018b. *Liegenschaftskataster*. https://www.bezreg-koeln.nrw.de/brk_internet/geobasis/liegenschaftskataster/index.html, 2019-1-5.

Bivand, R., Keitt, T., Rowlingson, B., 2017. *rgdal: Bindings for the 'Geospatial' Data Abstraction Library*. (R package version 1.2-15). https://CRAN.R-project.org/package=rgdal.

Bivand, R., Lewin-Koh, N., 2017. *maptools: Tools for Reading and Handling Spatial Objects*. (R package version 0.9-2). https://CRAN.R-project.org/package=maptools.

Congalton, R. G., Green, K., 2008. Assessing the accuracy of remotely sensed data: principles and practices. CRC press, Taylor & Francis, Boca Raton, Florida, USA.

Copernicus, 2018a. *Sentinel-1a IW GRDH images from orbit 37, growing season 2017. CRC/TR32 Database (TR32DB)*. http://www.tr32db.uni-koeln.de/data.php?dataID=1846.

Copernicus, 2018b. *Sentinel-1a IW GRDH images from orbit 88, growing season 2017. CRC/TR32 Database (TR32DB)*. http://www.tr32db.uni-koeln.de/data.php?dataID=1848.

Copernicus, 2018c. *Sentinel-1b IW GRDH images from orbit 37, growing season 2017. CRC/TR32 Database (TR32DB)*. http://www.tr32db.uni-koeln.de/data.php?dataID=1847.

Copernicus, 2018d. *Sentinel-1b IW GRDH images from orbit 88, growing season 2017. CRC/TR32 Database (TR32DB)*. http://www.tr32db.uni-koeln.de/data.php?dataID=1849.

Curdt, C., Hoffmeister, D., 2015. Research data management services for a multidisciplinary, collaborative research project: Design and implementation of the TR32DB project database. Program 49(4), 494–512.

Curlander, J., McDonough, R., 1991a. Synthetic Aperture Radar: Systems and Signal Processing. JohnWiley& Sons, New York, USA.

ESA, 2013. *Free access to Copernicus Sentinel satellite data*. (last accessed 6-June-2018).

FAO, 2017. The Future of Food and Agriculture. Trends and Challenges. FAO, Rome, Italy.

FAO, IFAD, UNICEF, WHO, 2017. The State of Food Security and Nutrition in the World 2017: Building Resilience for Peace and Food Security. FAO, Rome, Italy.

Fritz, S., See, L., Bayas, J. C. L., Waldner, F., Jacques, D., Becker-Reshef, I., Whitcraft, A., Baruth, B., Bonifacio, R., Crutchfield, J., et al., 2018. A comparison of global agricultural monitoring systems and current gaps. Agricultural Systems.

GDAL Development Team, 2017. *GDAL - Geospatial Data Abstraction Library, Version 2.2.3*. Open Source Geospatial Foundation. http://www.gdal.org.

Godfray, H. C. J., Garnett, T., 2014. Food security and sustainable intensification. Phil. Trans. R. Soc. B 369(1639), 20120273.

Heupel, K., Spengler, D., Itzerott, S., 2018. A Progressive Crop-Type Classification Using Multitemporal Remote Sensing Data and Phenological Information. PFG–Journal of Photogrammetry, Remote Sensing and Geoinformation Science 86, 53–69.

Hijmans, R. J., 2017. *raster: Geographic Data Analysis and Modeling*. (R package version 2.6-7). https://CRAN.R-project.org/package=raster.

Horning, N., 2013. *RandomForestClassification*. https://www.bitbucket.org/rsbiodiv/randomforestclassification/commits/534bc2f, 2019-1-5.

Hütt, C., 2018a. *Crop Classification 2017 of the Rur Catchement using Sentinel-1 and data from open.NRW. CRC/TR32 Database (TR32DB)*. http://www.tr32db.uni-koeln.de/data.php?dataID=1844.

Hütt, C., 2018b. *Crop mask 2017 derived from the ALKIS. CRC/TR32 Database (TR32DB)*. http://www.tr32db.uni-koeln.de/data.php?dataID=1850.

Hütt, C., 2018c. *DGM1, WGS84, 5m, based on data from Bezirksregierung Köln, Bonn, Germany. CRC/TR32 Database (TR32DB)*. http://www.tr32db.uni-koeln.de/data.php?dataID=1851.

Hütt, C., 2018d. *Enhanced Graph File for Processing Sentinel-1 Images using SNAP. CRC/TR32 Database (TR32DB).* http://www.tr32db.uni-koeln.de/data.php?dataID=1803.

Hütt, C., 2018e. *Sentinel-1 composite of the growing season 2017. CRC/TR32 Database (TR32DB).* http://www.tr32db.uni-koeln.de/data.php?dataID=1845.

Hütt, C., 2018. *Training and Validation Data for a Crop Type Classification of the TR32 - 2017 - based on the Crop Type Distribution Mapping 2017. CRC/TR32 Database (TR32DB).* http://www.tr32db.uni-koeln.de/data.php?dataID=1818.

Hütt, C., Koppe, W., Miao, Y., Bareth, G., 2016. Best Accuracy Land Use/Land Cover (LULC) Classification to Derive Crop Types Using Multitemporal, Multisensor, and Multi-Polarization SAR Satellite Images. Remote Sensing 8(8, 684).

Hütt, C., Waldhoff, G., 2018. Multi-data approach for crop classification using multitemporal, dual-polarimetric TerraSAR-X data, and official geodata. European Journal of Remote Sensing 51(1), 62–74.

Jensen, J. R., 2009. Remote sensing of the environment: An earth resource perspective. Pearson Education, London, United Kingdom.

Kenduiywo, B. K., Bargiel, D., Soergel, U., 2018. Crop-type mapping from a sequence of Sentinel 1 images. International Journal of Remote Sensing, 1–22.

Kersebaum, K. C., Hecker, J.-M., Mirschel, W., Wegehenkel, M., 2007. Modelling water and nutrient dynamics in soil–crop systems: a comparison of simulation models applied on common data sets. In: Kersebaum, K., Hecker, J.-M., Mirschel, W., Wegehenkel, M. (Eds.), Modelling water and nutrient dynamics in soil–crop systems. Springer, 1–17.

Liaw, A., Wiener, M., 2002. Classification and Regression by randomForest. R News 2(3), 18–22.

Machwitz, M., Hass, E., Junk, J., Udelhoven, T., Schlerf, M., 2018. CropGIS–A web application for the spatial and temporal visualization of past, present and future crop biomass development. Computers and Electronics in Agriculture.

McNairn, H., Shang, J., 2016. A review of multitemporal synthetic aperture radar (SAR) for crop monitoring. In: Ban, Y. (Ed.), Multitemporal Remote Sensing. Springer, 317–340.

McNutt, M., 2016. Taking up TOP. Science 352(6290), 1147.

NorGIS, 2017. ALKIS Import. https://github.com/norBIT/alkisimport, 2018-10-22.

Nosek, B. A., Alter, G., Banks, G. C., Borsboom, D., Bowman, S. D., Breckler, S. J., Buck, S., Chambers, C. D., Chin, G., Christensen, G., et al., 2015. Promoting an open research culture. Science 348(6242), 1422–1425.

Orfeo Developement Team, 2017. Orfeo Toolbox v. 5.8.0. https://www.orfeo-toolbox.org/, 2018-11-7.

Orfeo Developement Team, 2018. Classification Map Regularization, https://%5C-www.orfeo-%5C-toolbox.org/%5C-Cook%5C-Book/%5C-Applications/%5C-app%5C--%5C_Classification%5C-Map%5C-Regularization.html%5C#detailed-%5C-description, 2018-11-7.

Pebesma, E. J., Bivand, R. S., 2005. Classes and methods for spatial data in R. R news 5(2), 9–13.

PostGIS, 2017. *Spatial and Geographic objects for PostgreSQL 2.4.3, https://postgis.net.*

PostgreSQL, 2017. *The World's Most Advanced open source relational database, Version 10.2, https://www.postgresql.org/.*

QGIS Development Team, 2017. *Open Source Geospatial Foundation Project. http://qgis.osgeo.org.*

R Core Team, 2018. *R: A Language and Environment for Statistical Computing*. R Foundation for Statistical Computing. Vienna, Austria. https://www.R-project.org/,

Rocchini, D., Petras, V., Petrasova, A., Horning, N., Furtkevicova, L., Neteler, M., Leutner, B., Wegmann, M., 2017. Open data and open source for remote sensing training in ecology. Ecological Informatics 40, 57–61.

Rodriguez-Galiano, V. F., Ghimire, B., Rogan, J., Chica-Olmo, M., Rigol-Sanchez, J. P., 2012. An assessment of the

effectiveness of a random forest classifier for land-cover classification. ISPRS Journal of Photogrammetry and Remote Sensing 67, 93–104.

Schmullius, C., Thiel, C., Pathe, C., Santoro, M., 2015. Radar time series for land cover and forest mapping. In: Kuenzer, C., Dech, S., Wagner, W. (Eds.), Remote Sensing Time Series. Springer, New York, USA, 323–356.

Schubert, A., Small, D., Miranda, N., Geudtner, D., Meier, E., 2015. Sentinel-1A product geolocation accuracy: commissioning phase results. Remote sensing 7(7), 9431–9449.

Small, D., 2011. Flattening gamma: Radiometric terrain correction for SAR imagery. IEEE Transactions on Geoscience and Remote Sensing 49(8), 3081–3093.

SNAP-ESA, 2017. *Sentinel Application Platform v 5.0.1, http://step.esa.int.*

Sonobe, R., Tani, H., Wang, X., Kobayashi, N., Shimamura, H., 2014. Random forest classification of crop type using multi-temporal TerraSAR-X dual-polarimetric data. Remote Sensing Letters 5(2), 157–164.

Steiniger, S., Hunter, A. J., 2013. The 2012 free and open source GIS software map–A guide to facilitate research, development, and adoption. Computers, environment and urban systems 39, 136–150.

Torres, R., Snoeij, P., Geudtner, D., Bibby, D., Davidson, M., Attema, E., Potin, P., Rommen, B., Floury, N., Brown, M., et al., 2012. GMES Sentinel-1 mission. Remote Sensing of Environment 120, 9–24.

Vuolo, F., Neuwirth, M., Immitzer, M., Atzberger, C., Ng, W.-T., 2018. How much does multi-temporal Sentinel-2 data improve crop type classification? International Journal of Applied Earth Observation and Geoinformation 72, 122–130.

Waldhoff, G., Eichfuss, S., Bareth, G., 2015. Integration of remote sensing data and basic geodata at different scale levels for improved land use analyses. The International Archives of Photogrammetry, Remote Sensing and Spatial Information Sciences 40(3), 85.

Waldhoff, G., Herbrecht, M., 2018a. *Crop Type Distribution Mapping 2017. CRC/TR32 Database (TR32DB).* http://www.tr32db.uni-koeln.de/data.php?dataID=1820.

Waldhoff, G., Herbrecht, M., 2018b. *Enhanced land use classification of 2017 for the Rur catchment. CRC/TR32 Database (TR32DB).* http://www.tr32db.uni-koeln.de/data.php?dataID=1795.

Waldhoff, G., Lussem, U., Bareth, G., 2017. Multi-Data Approach for remote sensing-based regional crop rotation mapping: A case study for the Rur catchment, Germany. International Journal of Applied Earth Observation and Geoinformation 61, 55–69.

Whelen, T., Siqueira, P., 2018. Time-series classification of Sentinel-1 agricultural data over North Dakota. Remote Sensing Letters 9(5), 411–420.

Whitcraft, A., Vermote, E., Becker-Reshef, I., Justice, C., 2015. Cloud cover throughout the agricultural growing season: Impacts on passive optical earth observations. Remote Sensing of Environment 156, 438–447.

Woodcock, C. E., Allen, R., Anderson, M., Belward, A., Bindschadler, R., Cohen, W., Gao, F., Goward, S. N., Helder, D., Helmer, E., et al., 2008. Free access to Landsat imagery. Science 320(5879), 1011–1011.

Wulder, M. A., Coops, N. C., 2014. Make Earth observations open access: freely available satellite imagery will improve science and environmental-monitoring products. Nature 513(7516), 30–32.

Wulder, M. A., Masek, J. G., Cohen, W. B., Loveland, T. R., Woodcock, C. E., 2012. Opening the archive: How free data has enabled the science and monitoring promise of Landsat. Remote Sensing of Environment 122, 2–10.

Xie, Y., Sha, Z., Yu, M., 2008. Remote sensing imagery in vegetation mapping: a review. Journal of plant ecology 1(1), 9–23.

Xiong, J., Thenkabail, P. S., Gumma, M. K., Teluguntla, P., Poehnelt, J., Congalton, R. G., Yadav, K., Thau, D., 2017. Automated cropland mapping of continental Africa using Google

Earth Engine cloud computing. ISPRS Journal of Photogrammetry and Remote Sensing 126, 225–244.

Zhao, Q., Hütt, C., Lenz-Wiedemann, V. I. S., Miao, Y., Yuan, F., Zhang, F., Bareth, G., 2015. Georeferencing Multi-source Geospatial Data Using Multi-temporal TerraSAR-X Imagery: a Case Study in Qixing Farm, Northeast China. Photogrammetrie - Fernerkundung - Geoinformation 2015(2), 173–185.

Zink, M., Bachmann, M., Brautigam, B., Fritz, T., Hajnsek, I., Moreira, A., Wessel, B., Krieger, G., 2014. TanDEM-X: the new global DEM takes shape. IEEE Geoscience and Remote Sensing Magazine 2(2), 8–23.

7 Fusion of High Resolution Remote Sensing Images and Terrestrial Laser Scanning for Improved Biomass Estimation of Maize

Christoph Hütt[1], Henning Schiedung[2], Nora Tilly[1], Georg Bareth[1]

Published in: The International Archives of the Photogrammetry, Remote Sensing and Spatial Information Sciences, Volume XL-7, 2014 ISPRS Technical Commission VII Symposium, 29 September - 2 October 2014, Istanbul, Turkey

Original manuscript is embedded in dissertation format.

1. Institute of Geography (GIS & Remote Sensing Group), University of Cologne, 50923 Cologne, Germany,
e-mail: {christoph.huett} {n.tilly} {g.bareth}@uni-koeln.de

2. Institute of Crop Science and Resource Conservation, University of Bonn, 53121 Bonn, Germany,
e-mail: henning.schiedung@uni-bonn.de

7.1 Abstract

In this study, images from the satellite system WorldView-2 in combination with terrestrial laser scanning (TLS) over a maize field in Germany are investigated. Simultaneously to the measurements a biomass field campaigns was carried out. From the point clouds of the terrestrial laser scanning campaigns Crop Surface Models (CSMs) from each scanning date were calculate to model plant growth over time. These results were resampled to match the spatial resolution of the WorldView-2 images, which had to orthorectified using a high resolution digital elevation model and atmosphere corrected using the ATCOR Software package. A high direct correlation of the Normalized Difference Vegetation Index (NDVI) calculated from the WorldView-2 sensor and the dry biomass was found in the beginning of June. At the same date, the heights from laser scanning can also explain a certain amount of the biomass variation ($R^2 = 0.6$). By combining the NDVI from WorldView-2 and the height from the laser scanner with a linear model, the R^2 reaches higher values of 0.86. To further understand the relationship between CSM derived crop heights and reflection indices, a comparison on a pixel basis was performed. Interestingly, the correlation of the NDVI and the crop height is rather low at the beginning of June ($R^2 = 0.4$, n = 1857) and increases significantly ($R^2 = 0.79$, N= 1857) at a later stage.

7.2 Introduction

Sustainable modern agriculture practises have to guarantee food security for the increasing population of the world, minimize the difference of potential and actual yield, provide biomass for renewable energy production and optimize the input of fertilizers and pesticides while minimizing environmental impacts (Tilman et al. 2011; Gebbers & Adamchuk 2010). The only way to achieve those ambitious goals is the use of precision agriculture (Oliver 2013). But to apply this, measurements of plant parameters and its variability are needed with

high temporal and spatial resolution over the area under investigation. Remote Sensing is the technology to provide exactly this information (Mulla 2013). In this study the reflection values from the optical satellite WorldView-2 and plant height monitored with TLS are evaluated and combined to estimate the biomass of a maize field. Biomass is a very important parameter. It is the main input factor for the calculation of the Nitrogen Nutrition Index (NNI). With this parameter the manager of the field can use precision agriculture techniques to apply the exact amount of fertilizer Lemaire et al. (2008). Wrong amounts of fertilizer are related to some very important issues such as climate change through N2O release (Davidson et al. 2000) and water pollution through nitrate (Walton 1951).

7.3 Methods

7.3.1 Remote Sensing of Biomass

Reflectances of different wavelengths of the electromagnetic spectrum are used to make estimations of plant parameters. Mainly the difference of red light absorbed by the chlorophyll and the reflected energy in the infrared domain can be directly linked to the amount of photosynthesis (Gates et al. 1965). Within the resolution cell of imaging sensors mounted on different platforms the NDVI is used to use reflection for the approximation of the amount of photosynthesis. This amount of photosynthesis determines the biomass that is accumulated in the plant which leads to the yield. This approach has been well researched in the last decades and is applied on scales reaching from fields to regions (Moulin et al. 1998). Progress of sensor technology has led to use satellite remote sensing to monitor the scale underneath, the variations within a field or intra field variability is researched just after very high resolution sensors became available in the early 2000s (e.g. (Colombo et al. 2003)).

One aspect that is ignored when using only reflection values to estimate crop biomass is the 3 *rd* dimension. Imaging systems usually

only scan the top canopy of vegetation. To include plant height and structure related parameters in the calculation of biomass could on the one hand reduce the uncertainty of the measurement and on the other hand overcome limitations of the approach such as saturation of vegetation indices from reflection measurements with higher biomass and uncertainty in the measurement of the growth stages of agricultural crops.

7.3.2 Study Site and Data acquisition

All measurements of this study were carried out in the growing season of 2013 on a maize field situated near the village Selhausen-Niederzier. The next bigger cities are Düren (~10 km), Aachen (~30 km) and Cologne (~40 km). Mean Temperature varies from 9-11°C and the vegetation period last for about 170-190 days. Due to the position in the Lee-Side of the Eifel mountain range the precipitation is a bit lower than typically observed in nearby regions. It ranges from 500 to 600 mm/year. This temperate climate combined with the fertile soils provides good conditions for the intense agricultural production of the region; the main crops are maize, wheat, barley, sugar beet and potatoes. The terrain is virtually flat with slopes ranging from 0° to 3°. The mean elevation is about 100 m above sea level.

The maize field is situated at N 50°52'5", E 6°27'11" and has a spatial extent of about 60 m by 160 m and was chosen because of the heterogeneous soil conditions and thus an expected in- field variability of the plant biomass. Figure 7.3 and 7.4 show the field from different perspectives on different dates. Figure 7.2 gives an overview of how the field looks like on the four WorldView-2 images.

The satellite WorldView-2 is an optical satellite that acquires images with 8 Bands in the visible and infrared domain of the electromagnetic spectrum with a spatial resolution of 2 m and a panchromatic band with 0.5 m resolution (Updike & Comp 2010). Acquisitions were planned in the time frame where the most increase of biomass and plant height was anticipated. The actual image acquisitions took place on June 8th, July 7th, July 23rd and August 7th, Fig. 1 gives

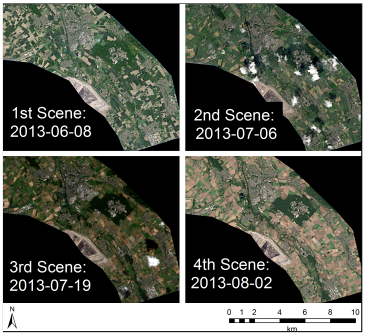

Figure 7.1: Overview of the four acquired WorldView-2 Scenes

Figure 7.2: Overview of the area of interest on the four satellite scenes. Note the cloud cover on the 3^{rd} scene which made any analysis impossible.

Figure 7.3: Southwest looking photo of the maize field on July 2nd, shortly before the 2nd WorldView-2 acquisition.

Figure 7.4: Northeast looking photo of the maize field on July 31st, just before the 4th WorldView-2 acquisition.

an overview of the Area that was covered. It consists of a strip of about 5 km width and approximately 15 km in length; the area is about 100 km2.

TLS measurements were carried out on 6 dates between May and September 2013. On each date the maize field was scanned with the TLS system Riegl LMS-Z420i (Riegl LMS GmbH 2010) mounted on a cherry picker and thereby reaching a height of about 8 meters. Four positions were chosen around the field corners to cover the whole field and minimize shadowing effects. For this study only the 2 datasets acquired on July 3rd and July 31st were used as they can be related to the 2nd and 4th satellite acquisition. Those were the only acquisitions where meaningful reflection values of the maize field could be extracted. A more detailed description of the season long TLS measurements can be found in Tilly, Hoffmeister, Schiedung, et al. (2014).

Corresponding to the TLS campaigns biomass was destructively taken. At 12 sample points distributed in the field, five plants were taken and their aboveground biomass was dried and and measured. The position of the points was measured using the highly accurate RTK-DGPS system Topcon HiPer Pro (Topcon Positioning Systems, Inc. 2014). Again in this study only the biomass samplings at the time of the 2nd and 4th World-View2 acquisition were useful. Unfortunately the processing of biomass was difficult for the 4th date due to technical problems while drying the biomass. Some plants were not completely dry before weighing therefore the biomass from this date was not used in this study.

7.3.3 Satellite data processing

A digital elevation model provided by the Landesvermessungsamt NRW with a 1 m spatial resolution was used to correct the topography related distortions of the images. For this orthorectification the only additional information that was needed was the Rational Polynomial Coefficients with sensor information at the time of the acquisition that are provided with the satellite images. GCPs were not needed. However, to test the spatial accuracy of the outcome a comparison of

the orthorectified panchromatic image to the digital orthophoto from the Landesvermessungsamt NRW in 40 cm resolution was performed. The absolute positional accuracy of these images is stated to be less than 6 dm (Geobasis-NRW 2014). To evaluate the absolute accuracy of the orthorectified images 5 check points mainly in urban areas distributed over the image area were used. The panchromatic images with a spatial resolution of 50 cm positioned at the same location as the multispectral 8 Band image was used to evaluate the accuracy of the multispectral image at a sub pixel level of the multispectral image (Figure 7.5). The ATCOR2 Software Package from Geosystems was used to correct the signal that was received at the satellite for the atmospheric distortion that exists in all optical satellite imagery. The algorithm was supplied with positions of the satellite and the sun at the time of image acquisition which can be found in the metadata file delivered with images. The visibility parameter acquired by the Deutscher Wetterdienst at the nearby weather observation station Düren were included to approximate the condition of the atmosphere at the time of image acquisition. As the open pit coal mining in this area and the surrounding cities are responsible for an increased amount of fine particular matter in the atmosphere the approximation parameter for the atmosphere was set to rural. The resultant reflectance values are the basis of the calculation of the NDVI from the bands of the WorldView-2 sensor. Mutanga et al. (2012) state that the NDVI calculated from the red edge (band 6) and NIR (band 8) improve the prediction accuracy of biomass and was therefore used in this study.

7.3.4 Statistical Analysis

The TLS-derived data sets are used to create CSMs, introduced by Hoffmeister et al. (2009) for plant growth monitoring. One CSM represents the crop surface of the whole field in a high resolution of 1 cm. As described in Tilly, Hoffmeister, Cao, et al. (2014), CSMs can be used to calculate plant height pixel-wise. For the combined analysis of the data sets, the high resolution CSMs had to be downsampled to match the comparatively coarse resolution of 2 m

of the multispectral WorldView-2 satellite. This was done using the mean crop height from the CSM per pixel area of the satellite image. For the extraction of all the values a regular point grid was created with the distance between points as long as the raster resolution. The ArcGIS-tool *extract multiple values at points* can then be used to extract the different reflection values of the 8 bands from different acquisitions of the WorldView-2 Satellite and the downsampled CSMs. Data from the biomass campaign was added to this complete dataset at those 12 points where ground measurements were made. The statistical analyses were done using the R software package (R Core Team 2014) and included computation of the NDVI values and linear regression analysis. Correlation and regression analyses were carried out to investigate the accuracy of the results and examine the usability of WorldView-2 in combination with plant height as predictor for biomass of maize.

7.4 Results

7.4.1 Positional Accuracy of the orthorectified WorldView-2 images

The CSMs from the laserscanning were acquired with a very high positional accuracy. The relative accuracy is less than 1 cm, whereas the absolute accuracy depends on the used differential Global Positioning System (GPS) which in this case is less than 1 m. A combined analysis with the optical satellite images only makes sense if their absolute positional accuracy also reaches high precision. Figure 7.5 shows one of 5 checkpoints where the positional accuracy of the satellite images was tested. Table 7.1 shows the results for all the points. The absolute positional error of the images was never higher than two multispectral pixels and on average a little bit larger than one multispectral pixel. Therefore, a combined analysis with the CSM derived plant heights is possible. The spatial combination in the GIS revealed spatial accordance of the datasets.

Check Point	absolute location error of orthorectified WV-2 to DOP [m]			
	June 8	July 6	July 19	August 2
1	1.0	3.5	1.2	3.7
2	2.2	3.1	0.4	2.6
3	3.6	3.6	0.8	2.5
4	3.4	3.2	1.3	3.8
5	1.6	3.5	3.1	2.2
Mean	**1.36**	**2.96**	**3.38**	**2.36**
Max	**3.1**	**3.8**	**3.6**	**3.6**
		Total	**Mean**	**2.52**
			Max	**3.8**

Table 7.1: Absolute positional error of the WorldView-2 images.

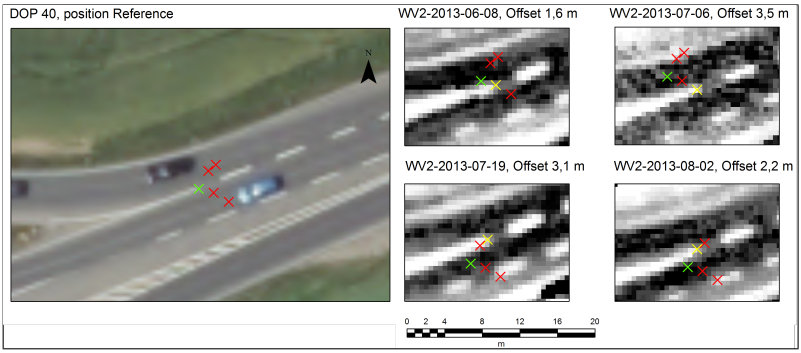

Figure 7.5: Accuracy checkpoint 5 and its position in the 4 satellite scenes. The total offset distance is always less than 2 multispectral pixels.

7.4.2 Statistical analysis

As the positional accuracy of the WorldView-2 images is sufficient for a combined analysis with the CSM derived plant height, correlation analysis were performed. The results can be divided into two parts:

1. Correlation of all measurements of the field. Analysis of the CSM derived plant heights and the reflection from WorldView-2 at the 2nd satellite image (WV-2: 2013-07-06, TLS: 2013-07-03) and about 1 month later at the 4th image (WV-2: 2013-08-02, TLS: 2013-07-31)

2. Biomass estimation with a combination of the data from the 2nd satellite image (2013-07-06) and the CSM derived plant height from the 2013-07-03. The first analysis from beginning of July where the maize plants are about 75 cm high reveals that the CSM plant height and the NDVI values are somehow related but not highly correlated (R^2=0.4). This indicates that the measurements contain independent information (Fig. 7.6). This changes at the end of July, where the plant height and NDVI have both increased a lot (Fig. 7.7). The maize plants have almost tripled in size and the NDVI values are a little less than twice as high. Here the R^2 increases to 0.79 which is an indicator for redundant information of the 2 measurements but also a proof that the proposed fusion is possible.

The second part made use of the biomass sampling at the 12 points (5 plants for each point). For the beginning of July with the linear regression analysis with CSM derived plant height and NDVI from WorldView-2 as estimator for the biomass the following formula was established:

$$\begin{aligned} &DryBiomass = \\ &CSMderivedplantheight * 7.17 \\ &+WorldView2NDVI(Bands8 + 6) * 131.697 \\ &-26.053 \end{aligned} \tag{7.1}$$

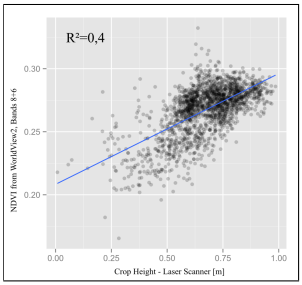

Figure 7.6: Correlation of NDVI from WorldView-2 (July, 7th) and CSM-derived plant height from July, 3rd (N=1857)

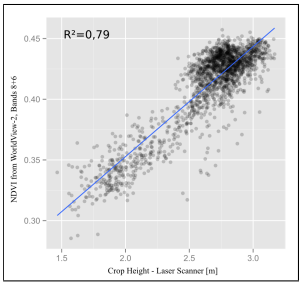

Figure 7.7: Correlation of NDVI from WorldView-2 (August 7th) and CSM-derived plant height from July 31th (N=1857)

Figure 7.10 shows the predicted biomass values from this formula plotted against the real measured values. The high R^2 of 0.86 shows the high correlation of the combination of the measurements. It has to be noted that this formula is valid for one date and one field only.

7.4.3 Spatial analysis

Based on the findings from the statistical analysis, Formula 7.1 was used to calculate a biomass map from the linear combination of WorldView-2 NDVI and CSM derived plant height of the whole maize field. Figure 7.11 shows the biomass distribution as sensed by the combination of the two sensors. In the western part the values are lower due to delayed plant development. The red line from north to south in the eastern part of the field results from drilling practices: The drilling machine had to drill in opposite directions in the end parts of the field. In those small lines with higher biomass predictions there there are twice as many plants due to overlapping of the drilling rows. Plant density was anticipated to be homogeneous over the field and was therefore not taken into account in this approach.

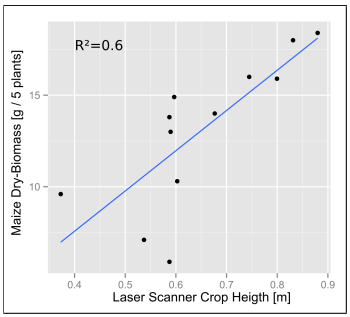

Figure 7.8: Regression of the CSM-derived plant height from July 3rd and dry biomass. (N=12)

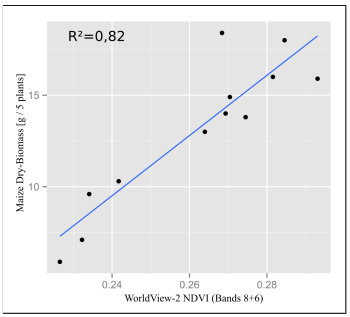

Figure 7.9: Regression of the NDVI (Bands 8+6) from 2nd WorldView-2 acquisition from the 6th July and the dry biomass taken on 3rd July (N=12).

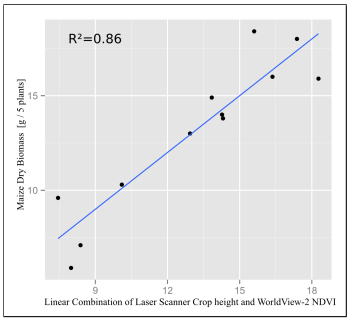

Figure 7.10: Regression of the linear (best Fit) combination of CSM-derived plant height and NDVI (Bands 8+6) from WorldView-2 with the dry biomass.

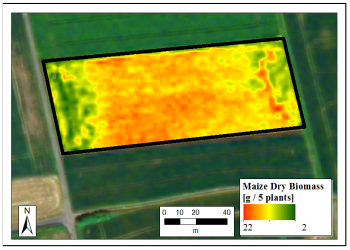

Figure 7.11: Final dry biomass Map for the 2nd date (07.07.2013), calculated from WorldView-2 NDVI and CSM derived plant height using formula 7.1. Background: Pansharpened WorldView-2 image from 8th June.

7.5 Discussion

Anticipated results were that TLS is able to monitor plant growth and its variability over the period where plant growth is dominant as shown by Hoffmeister et al. (2013) and Tilly, Hoffmeister, Cao, et al. (2014). Some limitations were expected if it comes to computation of the field variability at single dates. This in contrast was supposed to be the advantage of optical very high resolution imagery such as from the WorldView-2 for example shown by Colombo et al. (2003). The conducted field experiment revealed the difficulties of field experiments. Only two out of four satellite scenes could be linked to ground measurements. The biomass sampling could only be related to one of the images. For this event, however, the synergetic use of TLS and reflectance indices from optical sensors the improvement of the estimation of biomass for the biomass of the maize field was demonstrated. With the help of TLS, the third dimension in the calculation of biomass could be added and the precision of the calculation was increased. The high values of the R^2 of 0.86 has to treated cautiously as the established formula is only valid for a single field for one date. The biomass used to establish the formula was also used to calculate the R^2. An independent biomass sampling dataset would be needed to properly asses the accuracy of the proposed method.

However a spatial representation of the formula revealed patterns of intra-field biomass variability that can be related to the status of the field and could be the basis for further investigations. At a later stage, the similarity of the measurements of the two sensors was shown. But if two measurements are highly correlated it seems not meaningful to combine them as proposed. Other values from TLS could be extracted. Höfle (2014) showed how to extract individual maize plants from TLS. This approach could help to refine the proposed method as plant density was expected to be homogeneous all over the field and therefore not taken into account. Also it has to be noted that the spatial resolution of the TLS was degraded a lot to match the 2 m pixel size of the WorldView-2 sensor. A different approach could

include an upscaling of the WorldView-2 image to make use of the spatially far more precise TLS measurements.

Also it has to be noted that TLS measurements are very labor intense and can only be made for single selected fields. The main advantage of satellite imagery is transferability to larger areas with hardly any additional effort. On the other hand, consideration of the crop calendar has to be taken into account when monitoring crops with satellite images and clouds can make analysis impossible. A complete season long monitoring with optical very high resolution images seems only possible when the number of acquisitions is dramatically increased as for example shown by Claverie et al. (2012), who used 95 FORMOSAT-2 images at 8 meter resolution to monitor maize on a field level and stated the research of intra field variability as a future focus.

7.6 Conclusion an Outlook

In summary, the good potential of the WorldView-2 Sensor to monitor intra field biomass variation of a maize field was demonstrated for a single date. Height from TLS was included by combining crop surface models into the estimation of biomass and the measurement could be further refined. At a later stage the synergetic effects of the fusion have to be doubted as high correlation of the two sensors has been found. Limitations of optical satellite acquisitions due to cloud cover and problems in the processing of the biomass made it difficult to monitor the field for an extended period of time. More study is needed to understand the relation of plant height, reflectance and the accumulated biomass of maize. The measurements are repeated in the growing season 2014 with refinements learned from this study. Future analysis include multiple acquisitions of other satellites to also extract crop height variations from a satellite platform for an extended area.

7.7 References

Claverie, M., Demarez, V., Duchemin, B., Hagolle, O., Ducrot, D., Marais-Sicre, C., Dejoux, J.-F., Huc, M., Keravec, P., Béziat, P., 2012. Maize and sunflower biomass estimation in south-west France using high spatial and temporal resolution remote sensing data. Remote Sensing of Environment 124, 844–857.

Colombo, R., Bellingeri, D., Fasolini, D., Marino, C. M., 2003. Retrieval of leaf area index in different vegetation types using high resolution satellite data. Remote Sensing of Environment 86(1), 120–131.

Davidson, E. A., Keller, M., Erickson, H. E., Verchot, L. V., Veldkamp, E., 2000. Testing a Conceptual Model of Soil Emissions of Nitrous and Nitric Oxides: Using two functions based on soil nitrogen availability and soil water content, the hole-in-the-pipe model characterizes a large fraction of the observed variation of nitric oxide and nitrous oxide emissions from soils. Bioscience 50(8), 667–680.

Gates, D. M., Keegan, H. J., Schleter, J. C., Weidner, V. R., 1965. Spectral properties of plants. Applied optics 4(1), 11–20.

Gebbers, R., Adamchuk, V. I., 2010. Precision agriculture and food security. Science 327(5967), 828–831.

Geobasis-NRW, 2014. Digitale Orthophotos. https://www.bezreg-koeln.nrw.de/brk_internet/geobasis/luftbilderzeugnisse/digitale_orthophotos/index.html, 2018-1-16.

Hoffmeister, D., Waldhoff, G., Curdt, C., Tilly, N., Bendig, J., Bareth, G., 2013. "Spatial variability detection of crop height in a single field by terrestrial laser scanning". In: Precision agriculture '13. Ed. by J. V. Stafford. Wageningen Academic Publishers, Wageningen, Netherlands, 267–274.

Hoffmeister, D., Bolten, A., Curdt, C., Waldhoff, G., Bareth, G., 2009. High-resolution Crop Surface Models (CSM) and Crop Volume Models (CVM) on field level by terrestrial laser scanning. The Sixth International Symposium on Digital Earth, International Society for Optics and Photonics.

Höfle, B., 2014. Radiometric correction of terrestrial LiDAR point cloud data for individual maize plant detection. IEEE Geoscience and Remote Sensing Letters 11(1), 94–98.

Lemaire, G., Jeuffroy, M.-H., Gastal, F., 2008. Diagnosis tool for plant and crop N status in vegetative stage: Theory and practices for crop N management. European Journal of agronomy 28(4), 614–624.

Moulin, S., Bondeau, A., Delecolle, R., 1998. Combining agricultural crop models and satellite observations: from field to regional scales. International Journal of Remote Sensing 19(6), 1021–1036.

Mulla, D. J., 2013. Twenty five years of remote sensing in precision agriculture: Key advances and remaining knowledge gaps. Biosystems engineering 114(4), 358–371.

Mutanga, O., Adam, E., Cho, M. A., 2012. High density biomass estimation for wetland vegetation using WorldView-2 imagery and random forest regression algorithm. International Journal of Applied Earth Observation and Geoinformation 18, 399–406.

Oliver, M., 2013. An overview of precision agriculture. In: Oliver, M., Bishop, T., Marchant, B. (Eds.), Precision Agriculture for Sustainability and Environmental Protection (Earthscan Food and Agriculture). Routledge, London, United Kingdom. 3–19.

R Core Team, 2014. *R: A Language and Environment for Statistical Computing*. R Foundation for Statistical Computing. Vienna, Austria. http://www.R-project.org/,

Riegl LMS GmbH, 2010. Datasheet Riegl LMS-Z420i. http://www.riegl.com/uploads/tx_pxpriegldownloads/10_DataSheet_Z420i_03-05-2010.pdf, 2017-12-11.

Tilly, N., Hoffmeister, D., Schiedung, H., Hütt, C., Brands, J., Bareth, G., 2014. Terrestrial laser scanning for plant height measurement and biomass estimation of maize. The International Archives of Photogrammetry, Remote Sensing and Spatial Information Sciences 40(7), 181–187.

Tilly, N., Hoffmeister, D., Cao, Q., Huang, S., Lenz-Wiedemann, V., Miao, Y., Bareth, G., 2014. Multitemporal crop surface models: accurate plant height measurement and biomass estimation

with terrestrial laser scanning in paddy rice. Journal of Applied Remote Sensing 8(1), 083671.

Tilman, D., Balzer, C., Hill, J., Befort, B. L., 2011. Global food demand and the sustainable intensification of agriculture. Proceedings of the National Academy of Sciences 108(50), 20260–20264.

Topcon Positioning Systems, Inc., 2014. HiPer Pro Operator's Manual. http://www.top-survey.com/top-survey/downloads/HiPerPro_om.pdf, 2014-7-30.

Updike, T., Comp, C., 2010. Radiometric use of WorldView-2 imagery. Technical Note, 1–17.

Walton, G., 1951. Survey of literature relating to infant methemoglobinemia due to nitrate-contaminated water. American Public Health Association 41, 986–996.

8 Potential of Multitemporal TanDEM-X Derived Crop Surface Models for Maize Growth Monitoring

Christoph Hütt[1], Nora Tilly[1], Henning Schiedung[2], Georg Bareth[1]

Published in: The International Archives of the Photogrammetry, Remote Sensing and Spatial Information Sciences, Volume XLI-B7, 2016 XXIII ISPRS Congress, 12-19 July 2016, Prague, Czech Republic

Original manuscript is embedded in dissertation format.

1. Institute of Geography (GIS & Remote Sensing Group), University of Cologne, 50923 Cologne, Germany, e-mail: {christoph.huett} {n.tilly} {g.bareth}@uni-koeln.de

2. Institute of Crop Science and Resource Conservation, University of Bonn, 53121 Bonn, Germany, e-mail: henning.schiedung@uni-bonn.de

8.1 Abstract

In this study, first results of retrieving plant heights of maize fields from multitemporal TanDEM-X images are shown. Three TanDEM-X dual polarization spotlight acquisitions were taken over a rural area in Germany in the growing season 2014. By interferometric processing,

Digital Terrain Models (DTMs) were derived for each date with 5 m resolution. From the data of the first acquisition (June 1st) taken before planting, a DTM of the bare ground is generated. The data of the following acquisition dates (July 15th, July 26th) are used to establish CSMs. A CSM represents the crop surface of a whole field in a high resolution. By subtracting the DTM of the ground from each CSM, the actual plant height is calculated. Within these data sets 30 maize fields in the area of interest could be detected and verified by external land use data. Besides the spaceborne measurements, one of the maize fields was intensively investigated using TLS, which was carried out at the same dates as the predicted TanDEM-X acquisitions. Visual inspection of the derived plant heights, and accordance of the individually processed polarisations over the maize fields, demonstrate the feasibility of the proposed method. Unfortunately, the infield variability of the intensively monitored field could not be successfully captured in the TanDEM-X derived plant heights and merely the general trend is visible. Nevertheless, the study shows the potential of the TanDEM-X constellation for maize height monitoring on field level.

8.2 Introduction

The TanDEM-X Constellation (TDM) consists of the SAR satellites TerraSAR-X and TanDEM-X that fly in a close formation. TDM is the first satellite based solution for single pass radar interferometry (Krieger et al. 2007). Its main aim is the generation of a global elevation model. During the science phase other objectives can be pursued with innovative imaging modes, such as the one presented in this study.

Maize is one of the most important crops in the world. It is used to produce bio-fuel, but most importantly it serves as food for humans and animals (Nuss & Tanumihardjo 2010). In the context of a growing world population and decreasing area that is available for agriculture, a higher productivity is needed (Spiertz

2013). Therefore, accurate information about the state of maize fields is of great importance to allow precision agriculture techniques. In this context, is has been demonstrated that parameters based on optical and near infrared reflections, such as the NDVI correlate with plant height of maize (Freeman et al. 2007). Furthermore, Freeman et al. (2007) proposed a combined usage of plant height and NDVI to estimate biomass accumulation, resulting in an improved application of nitrogen.

Maize can be monitored from space using the visible and infrared part of the electromagnetic spectrum alone (Claverie et al. 2012; Pimstein et al. 2007). However, these techniques require cloud-free conditions and are therefore not reliable. In contrast, SAR is an all weather, day and night imaging system. Besides, the commonly used approach to use vegetation indices suffers from saturation effects (Chen, Fedosejevs, et al. 2006). Especially for monitoring maize plants, that gain a lot of height during the growing period, additional information about plant height, extracted from SAR images could help to overcome such saturation effects.

Accordingly, spaceborne SAR interferometry, such as from the ERS-Tandem mission (Santoro et al. 2010), has been utilized for maize monitoring. Though, the fast decorrelation of plants in general, mainly due to wind, resulting in a changing geometry of plants, hindered height retrieval. The innovative bistatic interferometric capability of TDM allows height retrieval even of moving vegetation. Therefore, TDM data has been used for height retrieval and biomass estimation of forests (Kugler et al. 2014) and the potential for agricultural purposes have already been demonstrated on paddy rice (Rossi & Erten 2015).

In the context of such promising capabilities of TDM, the objective of this paper is to investigate the potential of TDM for maize growth monitoring. We present first results of height retrieval by combining TDM image pairs from three dates. At each date, high resolution spotlight images with two independent polarisations were acquired with the same viewing geometry. As maize fields merely gain about 3 m in height, an increased baseline configuration of the TDM was

favoured, making it sensitive to the height variations of growing maize fields. The results are evaluated by comparing the heights from the two polarisations over all maize fields in the area of interest. For further reference, one maize field was intensively monitored using TLS and manual measurements within the field at similar dates as the images acquired from TDM.

8.3 Study site and data sets

The measurements were carried out over a collection of maize fields near Jülich, Germany (50.8°N, 6.4°E) in 2014. As the area is characterised by fertile soils, it provides good conditions for intense agricultural production. The main crops include maize, wheat, barley, sugar beet and potatoes. The terrain is virtually flat with slopes rarely exceeding 3°. The mean elevation is about 140 m above sea level.

The TDM images acquired for this study are a time series of three TDM image pairs, taken during the vegetation period 2014. The exact dates and individual characteristics of the acquisitions can be found in Table 8.1. As it can be seen, they have a Height of Ambiguity (HoA) reaching from 21.5 m to 27 m, which is a low value for the TDM, which makes the measurements sensitive to small height variances. All other configurations of the acquisitions were the same for all three image pairs: The viewing geometry is steep-looking with an incidence angle of only 23.4°. The polarization configuration is HH/VV for both satellites. This configuration results in 4 independent images for every acquisition, as they were taken in the standard bistatic mode with one satellite serving as the transmitter and both satellites as recorder of the same signal (Krieger et al. 2007). While the pixel spacing of the products is 0.9 m x 1.8 m (range x azimuth), the actual spatial resolution of the images is about 2 m.

On the predicted dates of the TDM acquisitions TLS was carried out on the same maize field that was already investigated one year earlier (Hütt et al. 2014; Tilly, Hoffmeister, Schiedung, et al. 2014). Based on experiences gained in this previous year, the scanning

No.	Date	Height of Ambiguity [m]	Effective Baseline [m]
1	June 1, 2014	-22.90	151.13
2	July 15, 2014	-21.58	160.29
3	July 26, 2014	-27.11	127.60

Table 8.1: TDM acquisitions that were used in this study. All acquisition are in Spotlight HS Mode with dual Polarisation HH/VV + HH/VV. They are taken from relative orbit 40 (ascending) and have an incidence angle of 23.4°.

dates were planned to be in the time-frame where the most plant growth was anticipated. The actual measurements took place on June 13, June 26, July 15, and July 31. On each date the field was scanned with the TLS system Riegl LMS-Z420i (Riegl GmbH, 2010) mounted on a cherry picker. Four positions close to the corners of the field were established to cover the whole field and minimize shadowing effects. An illustration of the methodology to use TLS-derived crop surface models for plant monitoring is given by Tilly, Hoffmeister, Schiedung, et al. (2014).

8.4 Methods

8.4.1 Interferometric Processing of the TDM acquisitions

The dual polarimetric measurement on both satellites results in four independent images for each acquisition. The images taken by the TDM constellation were preprocessed by the data provider German Aerospace Center (DLR) and delivered in CoSSC data format. All images resulting from one acquisition are already co-registered and filtered to the same Doppler spectrum (Duque et al. 2012). They can be directly used for interferogram generation. There is also no

Figure 8.1: Cherry Picker with Riegl Scanner next to the maize field, date: June 13, 2014.

need for additional bistatic considerations.

We used the SNAP processing environment (SNAP-ESA 2016), which conveniently also subtracts the flat earth phase and computes the coherence during the interferogram generation. Each polarisation was treated separately. In consequence there are two independent interferograms from every acquisition. The result of this first processing step can be seen in Figure 8.2.

The next step was a multilooking, which decreases the pixel spacing, but also the unwanted speckle effect. We chose 2 pixels in range and 3 pixels in azimuth. The result of this processing step can be seen in Figure 8.3.

The observed phase values are in modulo 2 π. A process called phase unwrapping estimates unambiguous phase values from those modulo 2 π interferograms. We used the SNAPHU algorithm (Chen & Zebker 2002) with MST initialisation and the statistical-cost method TOPO (see Figure 8.4).

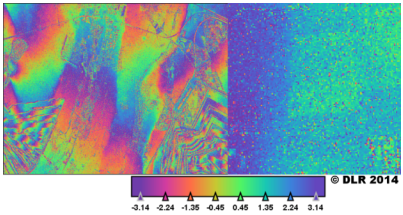

Figure 8.2: Interferogram generated from the TDM pair of July 15, 2014 (HH-Polarisation), left: whole scene, right: over the intensively monitored maize field.

Geocoding of all images was done by using the range doppler terrain correction (Curlander & McDonough 1991b; Dowman 1992) with the help of a high resolution digital terrain model (DTM) (Scilands-GmbH 2010). Final pixel spacing was set to 5 m during this process.

For geographic reference, we also processed a mean amplitude image with the same geometry. The very high relative accuracy of the images from one acquisition made it possible to stack the reference image with the two interferograms (HH+VV). Surprisingly, we found the absolute geometric accuracy of the TDM images to be not sufficient for a multitemporal pixel based processing. This issue was solved by co-registering the stack of each TDM acquisition to high resolution and highly accurate digital orthophotos (Geobasis-NRW 2014). The achieved accuracy was high, as the resulting root mean square error (RMSE) was always below half a pixel (2.5 m).

After that processing, the unwrapped interferograms were positioned correctly on the ground, but the values were still in degrees. Therefore, we used the HoA from the TDM metadata and formula 8.1 to transfer the values to meters.

$$heigth[m] = \frac{HoA * unwrappedphase}{2\pi} \tag{8.1}$$

Obtaining absolute height values was achieved by subtracting the

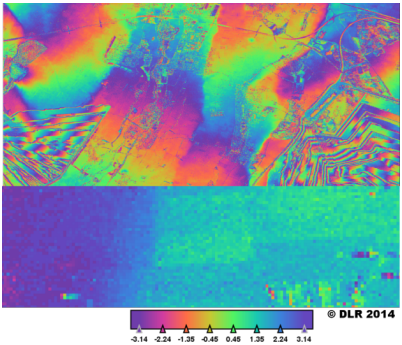

Figure 8.3: Multilooked Interferogram generated from the TDM pair of July 15, 2014, top: whole scene, bottom: over the intensively monitored maize field.

high resolution reference DTM (Scilands-GmbH 2010) from the TDM-derived DTM. Next, the median value of this Difference-DTM was used as offset-value to get the absolute ground height. Figure 8.5 shows the final DTM from HH-polarisation. The described processing was equally applied to all three TDM acquisitions for each polarisation individually, resulting in 6 DTMs.

8.4.2 Using crop surface models for plant height calculation

At the first TDM acquisition date (June 1st) the maize plants were just about to emerge. Consequently, the DTM derived from this date was used to calculate a DTM representing the bare ground. As no significant difference of the DTMs from HH- and VV-polarization was observed, we used the mean value of both DTMs. The later dates (July 15th, July 26th) were used to calculate crop surface models (CSM). As introduced by Hoffmeister et al. (2009) CSMs represent the surface of a whole field with a high spatial resolution. By subtracting the

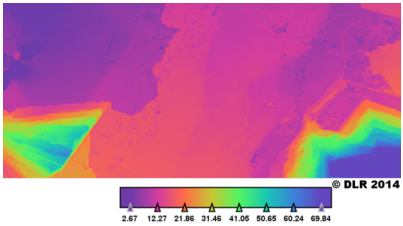

Figure 8.4: Unwrapped Phase generated from the TDM pair of July 15, 2014.

DTM of the bare ground from the CSM the plant height is calculated.

8.5 Results

Applying the described methodology resulted in rasters representing the difference in height between the first TDM acquisition and the later acquisitions. While the former is taken at the time, where merely the ground of the maize fields was visible, the latter were acquired at the time where the maize plants were developed. Therefore, this difference can be interpreted as maize plant height at the time of the later acquisitions. A high coherence over the maize fields made it possible to create Figures 8.6 and 8.7, which give an overview of the final plant heights acquired over the study area. Maize plants are clearly visible as the crops that gained the most height during the observation period in the study area. Consequently, they could be identified in these images. Furthermore, the identification is in accordance with land use classification data of this region (Lussem & Waldhoff 2014), which was generated using multitemporal optical satellite images and the land use class maize was validated with high accuracy (Waldhoff & Bareth 2009). To some degree the maps presented in Figures 8.6 and 8.7 can be used to identify delayed growth of some maize fields. However, there is still a high degree of noise, as

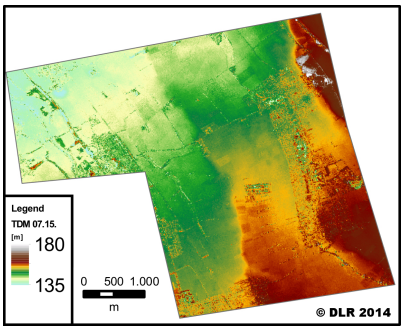

Figure 8.5: Geocoded DTM, generated from the TDM pair from 15.07.2014 (HH-Polarization images only)

a result of the speckle effect, within the fields.

While the proposed methodology was developed for monitoring growing maize fields, the images also reveal interesting facts of the nearby fields. Some of these non-maize fields show merely a pure noise pattern, because the processing over those fields failed. This is mostly because of low coherence at one of the TDM acquisitions. The field westwards of the intensively monitored field shows negative plant heights. This field was a rapeseed fields, which has been harvested in between the image acquisitions. Consequently, this results in a lower surface at the later acquisition and is therefore represented as negative plant height in the Figures 8.6 and 8.7.

To further evaluate the maize field plant heights extracted from TDM, results from the two individually processed polarizations were compared to each other. Figure 8.8 shows a comparison of the mean height values extracted over the maize fields in the area of interest. As above, the first TDM acquisition (June 1st) was used to create a DTM representing the bare ground from the mean value of the two polarisations. Especially for this figure the images from the HH- and the VV-Polarisation of the second TDM acquisition were processed independently and the outcomes were compared to each other. Results

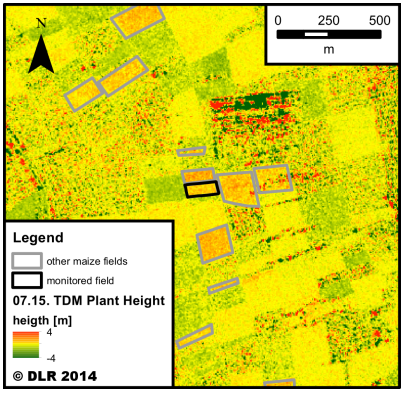

Figure 8.6: Heigth difference between June 1st and July 15th, derived from TDM.

show that the mean maize field plant heights, extracted from the two polarizations are well in accordance. They only differ very slightly from each other and no general difference of the polarizations can be observed.

After internal validation of the TDM-derived plant heights using the two polarizations separately, the heights retrieved from TDM were compared to TLS-derived height values. Figure 8.9 shows the result of the TLS-derived heights plotted against the TDM-derived heights over the intensively monitored maize field. For each TDM pixel the mean TLS-derived plant height was calculated. The TDM-derived plant heights show a fairly high standard deviation compared to the plant heights derived from the TLS measurements. Generally, the TDM data tempts to underestimate maize plant heights and merely the general trend of maize plant growth is visible. The pixel-based values of the TLS- and TDM-derived plant heights were not correlated.

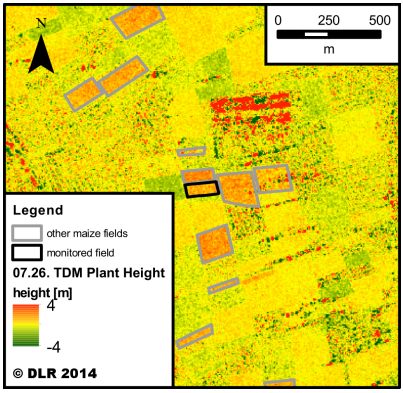

Figure 8.7: Heigth difference between June 1 st and July 26th, derived from TDM.

8.6 Discussion

In this paper, we investigated the potential of TDM for maize growth monitoring. Our results show that maize field heights can be successfully extracted from multitemporal, dual polarimetric TanDEM-X observations. The high resolution spotlight mode was useful for monitoring maize growth on a field basis. A successful validation using the two polarizations individually indicates the usability of the proposed method (shown in figure 8.8). Unlike (Rossi & Erten 2015) who found polarization and growth state related height differences in paddy rice, no difference of the heights obtained from the different polarisations was detected.

One limitation of this study is the quantification of the in-field variability of the intensively monitored field. The comparison to the TLS measurements revealed an underestimation of the maize plant height derived from TDM and a high standard deviation of the TDM-derived plant heights compared to the TLS-derived plant heights. The former can partly be explained by the difference of the observation

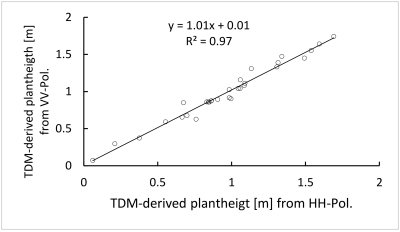

Figure 8.8: Mean height values from HH- and VV-Polarisations over of the maize fields of the region, generated from the TDM acquisitions No. 1 and 2 (Table 8.1) (n = 30).

angle. Even though the Laser Scanner was mounted on a cherry picker that reached a height of 8 m above the ground, the angle was still oblique compared to the steep incidence angle of TDM of 23.4°. The consequence of this steep angle should be a much deeper penetration of the radar signal into the maize field, whereas the oblique view of the TLS mainly interacts with higher parts of the plant.

Regarding the high standard deviation of the TDM-derived maize plant heights there are several issues to be taken into account. A key issue is the effective baseline of the TDM at image acquisition and the resulting HoA. For the analysis of complex terrain, higher HoAs and lower baselines prevent phase ambiguities. However, in this study, phase ambiguities were not an issue due to the low relief of the study site. Consequently, a much lower HoA and longer effective baselines would result in a higher sensitivity to the height differences within the maize fields. Another issue is the complex structure maize fields with multiple scatterers per SAR resolution cell resulting in speckle noise. This noise was already reduced by multilooking (Section 8.4). Conversely, the disadvantage of multilooking is a reduced spatial resolution, whereas a higher resolution of the final difference maps would improve sensitivity to small scale height differences of the maize field. Interferometric phase filtering (Lee et al. 1998) instead of multilooking could be used to decrease the speckle effect. Further-

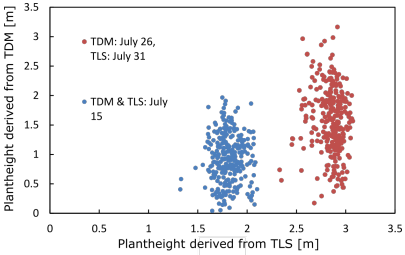

Figure 8.9: All pixel-wise extracted plant heights of the maize field at two different dates. For estimation of the TDM heights the mean of HH- and VV-Polarisation plant height was taken (each n = 293).

more, potential quality improvements can be achieved by considering atmospheric path delays (Fritz et al. 2011), which have not been taken into account at the presented processing chain.

In summary, our study shows that it is possible to obtain maize plant heights from the bistatic interferometric phase measurements of TDM. Since maize plant height correlates with maize biomass (Freeman et al. 2007), there is now the potential to estimate the actual biomass accumulation of maize fields, over an extended area, and regardless of the weather conditions.

8.7 Conclusions and Outlook

The study is a first attempt to retrieve maize plant heights based on interferometric processing of multitemporal TDM acquisitions. Plant height of maize fields could be spatially visualized and the results show the potential to monitor maize field heights. However, the reference data acquired with TLS on one maize field, revealed the limitations of the approach to monitor the in-field variability, which could not be detected from the TDM data so far. Future studies could include additional reference data, investigations of polarimetric

interferometric (PolIn) SAR features and integration of additional TanDEM-X acquisitions with different viewing geometries.

8.8 Acknowledgments

The TerraSAR-X / Tandem-X data were provided by DLR under the proposal: no. XTI_VEGE1746: Potential of Single Pass PolInSAR for Agriculture Monitoring.

8.9 References

Chen, C. W., Zebker, H. A., 2002. Phase unwrapping for large SAR interferograms: statistical segmentation and generalized network models. IEEE Transactions on Geoscience and Remote Sensing 40(8), 1709–1719.

Chen, P.-Y., Fedosejevs, G., Tiscareno-Lopez, M., Arnold, J. G., 2006. Assessment of MODIS-EVI, MODIS-NDVI and VEGETATION-NDVI composite data using agricultural measurements: an example at corn fields in western Mexico. Environmental monitoring and assessment 119(1-3), 69–82.

Claverie, M., Demarez, V., Duchemin, B., Hagolle, O., Ducrot, D., Marais-Sicre, C., Dejoux, J.-F., Huc, M., Keravec, P., Béziat, P., 2012. Maize and sunflower biomass estimation in south-west France using high spatial and temporal resolution remote sensing data. Remote Sensing of Environment 124, 844–857.

Curlander, J. C., McDonough, R. N., 1991b. Synthetic aperture radar- Systems and signal processing. John Wiley & Sons, Inc., New York, USA.

Dowman, I., 1992. The geometry of SAR images for geocoding and stereo applications. International Journal of Remote Sensing 13, 1609–1617.

Duque, S., Balss, U., Rossi, C., Fritz, T., 2012. *CoSSC Generation and Interferometric Considerations.*

Freeman, K. W., Girma, K., Arnall, D. B., Mullen, R. W., Martin, K. L., Teal, R. K., Raun, W. R., 2007. By-plant prediction of corn forage biomass and nitrogen uptake at various growth stages using remote sensing and plant height. Agronomy Journal 99(2), 530–536.

Fritz, T., Rossi, C., Yague-Martinez, N., Rodriguez-Gonzalez, F., Lachaise, M., Breit, H., 2011. Interferometric processing of TanDEM-X data. Geoscience and Remote Sensing Symposium (IGARSS), 2011 IEEE International, IEEE, 2428–2431.

Geobasis-NRW, 2014. Digitale Orthophotos. https://www.bezreg-koeln.nrw.de/brk_internet/geobasis/luftbilderzeugnisse/digitale_orthophotos/index.html, 2018-1-16.

Hoffmeister, D., Bolten, A., Curdt, C., Waldhoff, G., Bareth, G., 2009. High-resolution Crop Surface Models (CSM) and Crop Volume Models (CVM) on field level by terrestrial laser scanning. The Sixth International Symposium on Digital Earth, International Society for Optics and Photonics.

Hütt, C., Schiedung, H., Tilly, N., Bareth, G., 2014. Fusion of high resolution remote sensing images and terrestrial laser scanning for improved biomass estimation of maize. The International Archives of Photogrammetry, Remote Sensing and Spatial Information Sciences 40(7), 101–108.

Krieger, G., Moreira, A., Fiedler, H., Hajnsek, I., Werner, M., Younis, M., Zink, M., 2007. TanDEM-X: A satellite formation for high-resolution SAR interferometry. Geoscience and Remote Sensing, IEEE Transactions on 45(11), 3317–3341.

Kugler, F., Schulze, D., Hajnsek, I., Pretzsch, H., Papathanassiou, K. P., 2014. TanDEM-X Pol-InSAR performance for forest height estimation. Geoscience and Remote Sensing, IEEE Transactions on 52(10), 6404–6422.

Lee, J.-S., Papathanassiou, K. P., Ainsworth, T. L., Grunes, M. R., Reigber, A., 1998. A new technique for noise filtering of SAR interferometric phase images. Geoscience and Remote Sensing, IEEE Transactions on 36(5), 1456–1465.

Lussem, U., Waldhoff, G., 2014. Enhanced land use classification 2014 of the Rur catchment - Update, CRC/TR32 Database (TR32DB). http://tr32db.uni-koeln.de/data.php?dataID=1142, 2017-12-11.

Nuss, E. T., Tanumihardjo, S. A., 2010. Maize: a paramount staple crop in the context of global nutrition. Comprehensive reviews in food science and food safety 9(4), 417–436.

Pimstein, A., Karnieli, A., Bonfil, D. J., 2007. Wheat and maize monitoring based on ground spectral measurements and multivariate data analysis. Journal of Applied Remote Sensing 1(1).

Rossi, C., Erten, E., 2015. Paddy-rice monitoring using TanDEM-X. Geoscience and Remote Sensing, IEEE Transactions on 53(2), 900–910.

Santoro, M., Wegmüller, U., Askne, J. I., 2010. Signatures of ERS–Envisat interferometric SAR coherence and phase of short vegetation: an analysis in the case of maize fields. Geoscience and Remote Sensing, IEEE Transactions on 48(4), 1702–1713.

Scilands-GmbH, 2010. *Digital Elevation Model 10 with anthropogenic landforms, Goettingen, Germany.*

SNAP-ESA, 2016. *Sentinel Application Platform v 2.0.2, http://step.esa.int.*

Spiertz, H., 2013. Challenges for crop production research in improving land use, productivity and sustainability. Sustainability 5(4), 1632–1644.

Tilly, N., Hoffmeister, D., Schiedung, H., Hütt, C., Brands, J., Bareth, G., 2014. Terrestrial laser scanning for plant height measurement and biomass estimation of maize. The International Archives of Photogrammetry, Remote Sensing and Spatial Information Sciences 40(7), 181–187.

Waldhoff, G., Bareth, G., 2009. GIS-and RS-based land use and land cover analysis: case study Rur-Watershed, Germany. Geoinformatics 2008 and Joint Conference on GIS and Built environment: Advanced Spatial Data Models and Analyses, International Society for Optics and Photonics.

9 Overall Discussion

In the introduction, the overall objective of the work was elaborated. It is to obtain knowledge on how the combination of radar remote sensing, optical remote sensing, and other geodata can provide necessary geoinformation for land use science, precision farming, and agricultural monitoring systems. The overall objective was subdivided into smaller objectives. An elaboration on how those objectives were achieved forms the first chapter 9.1 of this overall discussion. Next, those results are put in a scientific context in chapter 9.2, before the limitations and recommendations for further research are given in chapter 9.3.

9.1 Overall Discussion of the Study Objectives

This overall discussion of the study objectives is structured in line with the same principle of increasing spatial and temporal resolution used throughout the thesis (compare 1.1). Consequently, the general LULC is considered first, with a second paragraph focusing on crop type. The third part discusses determining crop traits.

9.1.1 Objective 1: Determining LULC in Agricultural Landscapes

The research studies presented in chapters 3, 5, and 6 all perform LULC-classifications in an agricultural landscape. A typical characteristic of the two study sites is that the grown crops change annually. Before focusing on these crops, however, the differentiation of the

arable areas is required. Arable land does usually not change on an annual basis; hence, usually, a lower temporal resolution is needed. It is considered in the general LULC.

In chapter 3, this task of arable area determination was accomplished using the available remote sensing data. Therefore, the classification scheme has been extended to include the classes Urban, Concrete, Coniferous and Deciduous forest. The method introduced more costs, as each class had to be mapped and classified. Furthermore, the accuracy of classification potentially decreased, as a confusion with the crop classes could occur. As can be seen in the error matrices of Figures 3.4 and 3.5, the class Urban shows high confusion with almost all other classes. The confusion arises from the various surfaces found within the class Urban, which is often a mixture of different land covers (Albertz 2009: 163).

A solution to that problem is to include geo-information from other datasets (Albertz 2009: 165). However, such geodata often lacks the geometric precision (Bareth & Yu 2004; Zhang & Malczewski 2017) that is needed to be spatially fused with the remote sensing data (Zhang 2010). Therefore, in chapter 4, a methodology is presented to enhance the spatial accuracy of external geodata data of different sources. The innovative idea in chapter 4 is to use the high geometric accuracy found in modern SAR satellites such as TerraSAR-X (Reinartz et al. 2011) and Sentinel-1(Schubert et al. 2015).

The developed methodology of chapter 4 theoretically provides the opportunity to even include external data of lower spatial accuracy. However, the two studies where such data was applied are situated in Germany, where external data of very high accuracy already exists. Nevertheless, one focus of the two studies presented in chapters 5 and 6 was to quantify the benefit of using the MDA for integrating external data into the classification process.

By including external geodata, chapters 5 and 6 are applications of the MDA. The MDA crop classification approach using optical data (Waldhoff et al. 2015) has thereby been extended to using SAR images.

By comparing chapter 3 and chapters 5/6, it becomes apparent how

including the external geodata relaxes the spectral resolution needs of the remote sensing data. All three studies have comparable final OA accuracies. However, the first one needs a much higher spectral and spatial resolution. As discussed above, this higher resolution is partly needed to distinguish the arable land.

Furthermore, it is shows that including the external data with the MDA goes beyond just delineating arable land. The original non-crop classes of the external ATKIS, PB, and ALKIS data can be obtained, allowing information to be shown that is beyond the capabilities of remote sensing. Figure 5.5 demonstrates this approach by showing classes from the two mentioned datasets and those classes that were obtained by classifying the multitemporal TerraSAR-X remote sensing data.

The presented crop type enriched LULC maps show the often missing information about crop type along with the original LULC classes of the external data that was used. One example is grass in a park: It would not be distinguishable from agricultural pasture, as both have the same remote sensing signal. In this case, with appropriate external geodata, it would not only be possible to differentiate between the two; it would even be possible to present any related information. The crop-type enriched LULC maps found in Figures 5.5 and 6.1 provide more examples.

From the comparison of the three studies, it can be concluded that using external geodata in an MDA LULC-classification approach with SAR data proves beneficial for delineation of the arable land, enabled crop-type-enriched LULC maps with increased accuracy, and lowers the resolution needs of the remote sensing data.

9.1.2 Objective 2: Mapping Crop Types, especially the Annually Changing Cultivated Crops

After discussing the issue of determining general LULC, it is possible to focus on the crop classification only. Hence, an overall discussion of the classification of the crop type classes performed in the chapters 3, 5, and 6 is the focus of this section. For comparing the crop

type mapping performances, it is necessary to compare the different resolutions of the input datasets as shown in Figure 9.1.

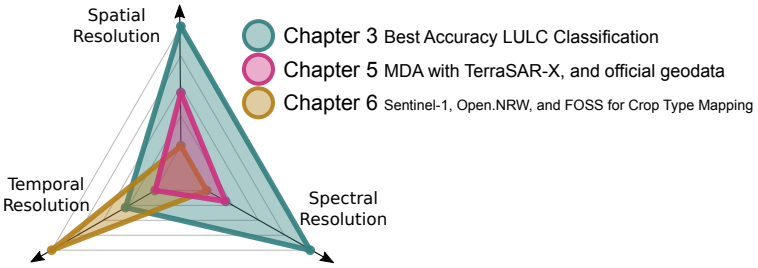

Figure 9.1: Comparison of the resolutions of the remote sensing input data of chapters 3, 5, and 6.

Chapter 3 deals with three C-band and ten X-band SAR images with varying polarization combinations (compare Table 3.2) and one optical image with four multispectral bands. The input data can hence be characterized as a very high spectral resolution. The spatial resolution reaches values of less than one meter from the TerraSAR-X satellite operating in spotlight mode, which can also to be considered as high. In comparison, the input data of chapter 5 is of lower resolution in all three relevant aspects. Only six dual-polarimetric images from TerraSAR-X were taken with a lower spatial resolution. The Sentinel-1 A and B images used in chapter 6 have an even further decreased spatial resolution compared to the other crop type studies. However, the temporal resolution is increased to 70 images.

In a comparative discussion, the question arises: *what is the optimal resolution for crop classifications using SAR and optical satellite remote sensing?*. It is challenging to find the general optimum resolution recommendation in the triangle of temporal, spatial, and spectral resolution for crop type classification (Löw & Duveiller 2014). Nevertheless, the comparison of the different resolution over the chapters reveals new insights into that issue.

The spatial resolution for crop type mapping is determined by the

field sizes of the AOI (Duveiller & Defourny 2010). For the study site Qixing farm, China, the high spatial resolution was especially suitable for accurate mapping of the sometimes small paddy rice fields. For example, each high-resolution image in chapter 3 provides an OA between 79 % OA and 86 %. The lower resolution single date images struggle with this task; their OA is merely 51 %–73 %. Even the combination of all lower resolution images provides only 83 %, compared to 95 % from the combined high-resolution images. Hence, the accuracies only reach high values from the high spatial resolution. Unsurprisingly, in the German AOI with larger fields, this is different. This can be seen from the high of 97 % OA reached in chapter 6, although the spectral and spatial resolutions of the input data are considerably lower than the input data used in the other chapters.

The spectral resolution has to be high enough to differentiate between different crops. It can be seen that the optical FORMOSAT-2 image slightly outperforms the single-date radar images (Figure 3.3) in terms of crop separation capability, which is in accordance with other studies (Blaes et al. 2005; McNairn, Champagne, et al. 2009; Forkuor et al. 2014). Almost no difference was observable between C-band or X-band polarimetric SAR (Skriver 2012). The combination of optical with SAR and the combination of X- and C-band always resulted in higher accuracies. Hence, the spectral resolution recommendation based on the studies is that all used sensors deliver information for distinguishing between the crops, but a combination of different sensors is beneficial and provides increased accuracies. For SAR-based studies, polarimetric decompositions can be performed for crop classifications (Sun et al. 2018). In chapter 6, this advantage of the polarimetry (Cloude 2010) was not exploited, although it was in the other studies. Still, the resulting crop type map of 6 showed a very high OAs. This shows that the question of spectral resolution is strongly connected to the available temporal resolution.

The temporal resolution needs for a successful crop classification are also AOI dependent, mainly due to different climates (McNairn & Shang 2016). The continental climate of the Chinese AOI results

in frigid winters, with no plant growth possible. The vegetation period is short but intense. All crops are seeded, grown, and harvested during that time (compare 2.4.1). The effect is that a reduced temporal resolution is needed to classify the crops in the Chinese AOI: Firstly, because all crops are grown in the same period, and are all visible during that time and secondly, because the vegetation period is shorter and there is no need for monitoring during winter. This lower dependence on a high temporal resolution, can be seen in the results: the best single date classifications of chapter 3 provided an OA of 89 % (Figure 3.3) for the Qixing farm including classification of non-crop classes. In contrast, all single-date crop-only classifications in chapter 5 performed worse although the crop area was delineated using the external geodata. It only reached a sufficient OA when the crop classes were reduced (compare Figure 5.3).

From chapter 5.6.1, where optimizing the acquisition plan was discussed, the crucial importance of timing in the German AOI is further elaborated. Under the circumstances of a continuous monitoring pattern, such as provided by Sentinel-1 (Torres et al. 2012), this knowledge becomes less important as the surface is imaged nevertheless. Notably, the higher temporal resolution described in chapter 6, with 70 Sentinel-1 images was even able to disaggregate the winter cereals with decent accuracy.

The research performed and this overall discussion on crop type mapping allow the conclusion that:

- multitemporal SAR sensors provide an excellent opportunity for crop type mapping.

- fusing sensors with different spectral properties, X-band with C-band, optical and radar, proved beneficial for increasing the OA of the crop type maps.

- choosing the spatial resolution for crop type mapping is crucial for sufficient accuracy. However, it is AOI dependent, and a general recommendation is difficult.

- a very high temporal resolution, such as the one from the SAR sensor Sentinel-1, accounted for other sensor's deficiencies in the spatial and spectral domain. It outperformed TerraSAR-X data with higher spectral and spatial resolution.

9.1.3 Objective 3: Detecting the In-Field Variability of Crop Traits such as Plant Vitality, Height, and Biomass.

A further increase in spatial and temporal resolution is provided in the data used in the chapters 7 and 8. They work on the level of one single field and aim to detect in-field variations of the crop traits height, and photosynthesis, and, based on that prediction, of the biomass . This alone is a reason to sort them behind the other chapters. Additionally, the knowledge of crop type is a prerequisite to analyzing crop traits on the field level, and should, therefore, be determined first.

Both studies rely on TLS measurements (compare chapters 8.3 and 7.3.2) and satellite-based observations, over the same maize field near Selhausen. Chapter 7 describes the fusion of high-resolution Worldview-2 optical reflectance data with the TLS height measurements to better predict biomass. In chapter 8, the highly accurate TLS measurements are used as a reference for a new method to derive maize canopy height from the TDM.

The studies had the particularity of relying on the ground measurements TLS from a cherrypicker and destructive biomass samplings. The high dynamic of the growing maize field made it necessary to keep a tight schedule for all measurements. Fundamental changes in between measurements would not allow the comparison or fusion of the datasets (Zhang 2010). Therefore, the temporal resolution of the remote sensing sensors has to be high. In this case, it is not the actual number of acquisitions being taken but the ability to acquire an image within a time-window of one or two days. In the case of WorldView-2, which is steerable, an image can be captured daily. However, the problem of clouds in the image drastically decreases this capability, as

can be seen in Figure 7.2. A whole ground campaign was performed in vain as one single cloud was over the maize field at the time of the acquisition.

This is different for TDM. The system is also electronically steerable, with the possibility of an almost daily acquisition (Krieger et al. 2007). The difference lies in the used microwave frequencies, which are not disturbed by clouds. However, the two satellites of the TDM system have a particular movement around each other, resulting in varying effective baselines, and hence varying height sensitivities (Fritz et al. 2011). Therefore, with the current implementation of TDM, not all images are suitable for maize height determination.

Potentially, the methods provided in chapters 7 and 8 could be used together to provide enhanced biomass predictions by combining crop height measurements from TDM and spectral information from Worldview-2. However, the performance evaluation using the TLS shows the deficiencies of the TDM derived crop heights. The height variability over the maize field was too high for precision farming purposes.

One reason might be because the TDM sensor was designed as a tool to capture the earth's relief with variation in the order of 10^4 m and not of plant growth (Zink et al. 2014). However, the innovative single-pass interferometry of TDM provides insights into the potential next-generation microwave sensors for determining crop traits. This aspect is further discussed in chapter 9.2.3.

9.2 Putting the Results in a Scientific Context

After the overall discussion of the different chapters of the thesis, this section provides a further discussion against relevant publications in the respective context.

9.2.1 Improving LULC-mapping by Combining SAR and Optical Remote Sensing Data

The studies described in chapters 3, 4 and 5 have shown that LULC can be derived efficiently, and with high accuracy from SAR images. This statement is in agreement with various other studies on the topic, such as Bryan (1983), Dobson et al. (1995), and Qi et al. (2012). Also, the fusion of different sensors was found to improve the classifications, which is in general accordance with the studies by Solberg et al. (1994), (Schmullius et al. 2015), and Gomez-Chova et al. (2015).

Incorporating more satellite sensors for LULC-mapping is shown by Hagensieker & Waske (2018), who use the L-Band sensor ALOS-2 in combination with X- and C-Band SAR sensors Radarsat-2 and TerraSAR-X. L-Band should theoretically be useful in discriminating different forest types, a possible extension to the research studies presented in this thesis. Furthermore, a combined analysis of X- C- and L- Band could be used to evaluate the potential of dual-band SAR-missions, such as the proposed NISAR mission concept (Xaypraseuth et al. 2015).

However, the shown studies work on a local scale and extent only. Although the developed methodologies are theoretically relevant for mapping on a wider area, there are challenges when LULC needs to be available over a national, continental or global extent. Until recently, LULC information on such larger areas was only available in lower spatial resolution (Ban et al. 2015). Recently, a global land cover map in 30 m resolution was created (Chen et al. 2015) using Landsat data. Although the class agriculture, for example, is not further classified into different crops, and the maps might contain misclassifications, the great potential of remote sensing for mapping the entire earth's surface is demonstrated.

SAR-based mapping approaches on larger areas are also possible. Ottinger et al. (2017) demonstrate how to include more than 500 Sentinel-1 scenes for mapping coastal aquaculture ponds over larger areas. Esch et al. (2013) demonstrate the immense potential of

TDM for global mapping. They delineate the global area of human settlements at 12 m resolution. With a high resolution DEM from the TDM being available (Zink et al. 2014), processing Sentinel-1 images for global LULC should also be feasible. However, even though global or large area mapping is possible, there is still the need to also validate such approaches on a local to regional scale. The studies presented in chapters 3, 5 and 6 would be suited to such a validation.

Applying the MDA on larger scales would also imply further opportunities and challenges. One advantage of extending the MDA approach using SAR images was the delineation of arable land using external geodata. Bargiel (2017) also use ATKIS, Immitzer et al. (2016) use open street map data for this task. While ATKIS is only available on a national scale, the latter would also be available globally, however with lower accuracy Zhang & Malczewski (2017). The second advantage of the MDA for a post-classification fusion of a SAR-based classification with classes from external geodata for enhanced LULC maps, as presented in chapter 5, was not found in the literature. This is in accordance with the statement of (Bareth & Waldhoff 2018), who conclude, that many studies fail to exploit the full potential to use such GIS-concepts for LULC-mapping .

9.2.2 Crop Type Mapping with Increased Efficiency and Accuracy

The high temporal capability of Sentinel-1 was demonstrated to be beneficial for separating crops in chapter 6, where 70 acquisitions were combined within one cropping period. The strategy proposed in chapters 3, 5 and 6 would be suited to handling an immense amount of images to extract LULC and crop type with high accuracy. The question is whether an even higher temporal resolution would be more beneficial. Another study by Moran et al. (2012) used 57 C-band Radarsat-2 images to distinguish crop types; they merely conclude that the high number of images improved the classification accuracy. However, with an increasing number of acquisitions, it should be possible to increase the number of classes. One possible extension

that could arise from the increased amount of remote sensing images is the additional consideration of winter land use (Denize et al. 2019), which has been neglected in the crop classifications of this study. Another benefit of a further increase of the temporal resolution would be identification of the crops earlier within the season (Lussem et al. 2016; McNairn et al. 2014).

However, most approaches, such as the recent ones by Moran et al. (2012) or Bargiel (2017), as well as the studies presented here, are supervised classifications. They are adapted to the crop classes that occur in the AOI. In such approaches, much depends on the quality of the mapping campaign. Categorial errors based on mislabelled classes could decrease the accuracy of the classification, especially if RF is used (Pal 2005). Insufficient ground reference can result in unreliable results, as discussed in chapter 5, where the number of potato field was identified to be insufficient.

Those supervised approaches all fail to build a general connection between scattering mechanism, phenology, and crop type. Especially for SAR-based studies, it is known that each crop has its distinct phenology with each stage associated with different scattering mechanisms (Koppe et al. 2013; Ulaby et al. 1996). Cloude & Pottier (1996) and Cloude & Pottier (1997), for example, interpret interactions of the signal with the target, which leads to a characterization of those surfaces without a ground reference. Hence, theoretically, as already demonstrated for optical remote sensing by (Heupel et al. 2018), future SAR-based crop classifications should be possible based on knowledge of phenology, without relying on a ground reference.

9.2.3 Crop Traits Mapping with Increased Accuracy using SAR Satellite Measurements

Hyperspectral remote sensing has long been used to determine crop traits (Thenkabail et al. 2000). However, the common method of using vegetation indices to predict parameters such as plant biomass contains drawbacks (Homolova et al. 2013), leading to uncertainties in the prediction (Chao et al. 2019). One promising methodology is

combining height measurements and optical reflectance measurements for predicting biomass with increased accuracy (Tilly et al. 2015). An increase in prediction accuracy has also been found in chapter 7. However, crop height alone was already highly correlated with the biomass of the plants (Tilly, Hoffmeister, Schiedung, et al. 2014). Furthermore, established methods to obtain crop height, such as TLS (Tilly, Hoffmeister, Cao, et al. 2014), Lidar, or UAV are expensive and not available over larger areas.

Obtaining crop height from satellite measurements would dramatically decrease the costs per area and increase the coverage. However, until recently, other attempts to do just that failed because of temporal decorrelation (Santoro et al. 2010). Only with the unique TDM, first attempts at height retrieval from a satellite were made in the research portrayed in chapter 8. Interestingly, the potential of the system was also illustrated by (Erten et al. 2016), who show such height measurements from TDM over rice. They also state that the accuracy of the height measurements strongly depends on the effective baseline of the TDM. This parameter changes randomly, but the general magnitude of the parameter can be controlled. The idea for future bistatic SAR missions is to fly several lower-cost receiver-only SAR satellites, which operate with multiple baselines to improve the height measurement (Kraus et al. 2017). One such mission is SESAME, which is proposed for a future mission (López-Dekker et al. 2017). With several baselines available, one baseline could be optimized for the determining plant crop height. Furthermore, as already elaborated in chapter 2.1.2, SAR-satellites are about to improve in the near future (Moreira et al. 2013), which should also provide enhanced crop traits mapping potentials.

It can be concluded that crop traits mapping with a combination of optical reflectance and radar-based height is possible. However, planned sensor innovations are awaited to lower the inaccuracy of the measurements, allowing more precise crop traits predictions.

9.3 Limitations and Possible Research Extensions

Although the developed workflows of the presented studies all delivered high accuracies, many aspects of the workflows have further development potential. This section discusses the limitations of the research and possible follow-up research possibilities.

The present study mainly relies on pixels as the geometric unit. Other studies include a segmentation preceding the classification or use external data to obtain the objects that are to be classified (McNairn, Champagne, et al. 2009, Mahmoud et al. 2011). On the one hand, such object-based approaches can result in increased accuracy (Blaschke 2010). On the other hand, a segmentation adds more complexity to the process and increases the difficulties of adapting the methodology to other classification scenarios.

The presented studies do not incorporate crop growth models, which is an extension that is widely used in remote sensing studies in an agricultural context (Houborg et al. 2015). Using such models in conjunction with remote sensing data provides the opportunity to predict crop traits with improved accuracy (Launay & Guerif 2005). Furthermore, such models run with user-defined time steps and the crop trait development in between the remote sensing acquisitions can be modeled (Kersebaum 2011). Nevertheless, the studies shown in chapters 7 and 8 could well be used to either improve existing crop growth models or to validate them.

Another extension that can optionally be performed before carrying out extensive field campaigns for remote sensing is the implementation of radiative transfer models. They have been implemented for optical remote sensing (Verhoef 1998) and for microwave remote sensing (Mo et al. 1982). Such approaches allow the remote sensing signal to be connected to the target value, which can be vegetation traits such as leaf area index or biomass (Houborg et al. 2015). The remote sensing campaign could then be planned better according to the spectral, spatial and temporal resolution needs, even before any

acquisition is acquired.

A logical follow-up is increasing the size of AOIs. The methodologies developed and applied for LULC mapping and crop type mapping are theoretically also applicable to the level of states, countries, and continents. However, the data needed to cover continents is currently more than standard computer hardware can handle. Continent-wide applications, such as the one presented by (Xiong et al. 2017), demand a shift in paradigm – from local processing to cloud computing environments. They have the advantage of distributing the processing to computers that are combined in the cluster.

10 Conclusion

This thesis is motivated by the fundamental necessity of the availability of geodata from agricultural land for a sound planning basis, for the improvement of field management and thus, for the future food security of mankind. Despite an unprecedented data diversity, the unsatisfying availability of usable geodata hinders both the various users of LULC and agricultural monitoring systems from delivering more profound decision support.

However, the needed data either already exists or can be acquired through satellite remote sensing systems. As frequent cloud coverage over agriculture is typical, SAR microwave remote sensing with the ability of also working in cloudy conditions has a central role to play. The thereby-increased reliability proved beneficial for fulfilling the objectives of the study, despite the increased processing complexity and peculiar look of the images. A particular advantage of SAR-sensors is the high geometric accuracy of the processed images once a high quality elevation model is available. This accuracy proved to be beneficial for creating a spatial reference. It also proved useful in combination with the MDA for the fusion with external existing geodata, either before a classification to enable the focus on the arable land – which increased the crop separation capability of the remote sensing images – or post classification for creating enhanced LULC-maps.

For precision farming purposes, the information of crop biomass on the field level is essential. Optical reflectance information from high resolution satellite image were successfully used in conjunction with plant height parameters to better predict in-field biomass variations of a maize field. A logical extension would be to also measure plant height from space. A case study using the new possibilities offered by

the TDM showed potentials to achieve this.

Images from SAR sensors showed themselves to be highly suitable for the monitoring of agricultural surfaces. LULC and especially the yearly changing crops with be precisely mapped. The fusion with data from optical sensors and external geodata proofed beneficial for the accuracy of the results. Together with the expected SAR sensor developments in the near future, also precision agricultural applications are possible.

Land use studies and agricultural monitoring systems should make use of satellite SAR data or the derived information to increase their reliability and accuracy of prediction. Decision-makers at various levels can thus better prepare themselves for the future challenges of global agricultural production.

11 References of chapters 1, 2 and 9

Albertz, J., 2009. Einführung in die Fernerkundung. Wissenschaftliche Buchgesellschaft, Darmstadt, Germany.

Alexander, P., Rounsevell, M. D., Dislich, C., Dodson, J. R., Engström, K., Moran, D., 2015. Drivers for global agricultural land use change: the nexus of diet, population, yield and bioenergy. Global Environmental Change 35, 138–147.

Anderson, J., Hardy, E., Roach, J., Witmer, R., 1976. A land use and land cover classification system for use with remote sensor data. United States Government Printing Office, Washington D.C., USA.

Atkinson, P. M., Tatnall, A. R., 1997. Introduction neural networks in remote sensing. International Journal of remote sensing 18(4), 699–709.

Atzberger, C., 2013. Advances in remote sensing of agriculture: Context description, existing operational monitoring systems and major information needs. Remote Sensing 5(2), 949–981.

Ban, Y., Gong, P., Giri, C., 2015. Global land cover mapping using Earth observation satellite data: Recent progresses and challenges. ISPRS journal of photogrammetry and remote sensing (Print) 103(1), 1–6.

Bareth, G., 2008. Multi-Data Approach (MDA) for enhanced land use and land cover mapping. ISPRS Archives Vol. XXXVII. Part B8 Proceedings of the XXI ISPRS Congress, 3-11 July, 2008, Beijing, China, 1059–1066.

Bareth, G., Waldhoff, G., 2018. GIS for Mapping Vegetation. In: Huang, B. (Ed.), Comprehensive Geographic Information Systems.

Reference Module in Earth Systems and Environmental Sciences. Elsevier, Amsterdam, Netherlands.

Bareth, G., Yu, Z., 2004. Verfügbarkeit von digitalen Geodaten in China. Petermanns Geographische Mitteilungen 148(5), 78–85.

Bargiel, D., 2017. A new method for crop classification combining time series of radar images and crop phenology information. Remote Sensing of Environment 198, 369–383.

Bendig, J., Bolten, A., Bareth, G., 2012. Introducing a low-cost mini-UAV for thermal-and multispectral-imaging. Int. Arch. Photogramm. Remote Sens. Spat. Inf. Sci 39, 345–349.

Bendig, J., Yu, K., Aasen, H., Bolten, A., Bennertz, S., Broscheit, J., Gnyp, M. L., Bareth, G., 2015. Combining UAV-based plant height from crop surface models, visible, and near infrared vegetation indices for biomass monitoring in barley. International Journal of Applied Earth Observation and Geoinformation 39, 79–87.

Benediktsson, J. A., Chanussot, J., Moon, W. M., 2012. Very high-resolution remote sensing: Challenges and opportunities [point of view]. Proceedings of the IEEE 100(6), 1907–1910.

Blaes, X., Vanhalle, L., Defourny, P., 2005. Efficiency of crop identification based on optical and SAR image time series. Remote Sensing of Environment 96(3-4), 352–365.

Blaschke, T., 2010. Object based image analysis for remote sensing. ISPRS journal of photogrammetry and remote sensing 65(1), 2–16.

Brisco, B., Brown, R., 1995. Multidate SAR/TM synergism for crop classification in western Canada. Photogrammetric Engineering and Remote Sensing 61, 1009.

Bryan, L. M., 1983. Urban land use classification using synthetic aperture radar. International Journal of Remote Sensing 4(2), 215–233.

Bush, T., Ulaby, F., 1978. An evaluation of radar as a crop classifier. Remote Sensing of Environment 7(1), 15–36.

Büttner, G., Feranec, J., Jaffrain, G., Mari, L., Maucha, G., Soukup, T., 2004. The CORINE land cover 2000 project. EARSeL eProceedings 3, 331–346.

Campbell, J. B., Wynne, R. H., 2011. Introduction to remote sensing. Guilford Press, New York, USA.

Carlson, T. N., Ripley, D. A., 1997. On the relation between NDVI, fractional vegetation cover, and leaf area index. Remote sensing of Environment 62(3), 241–252.

Carr, P., Carlson, G., Jacobsen, J., Nielsen, G., Skogley, E., 1991. Farming soils, not fields: A strategy for increasing fertilizer profitability. Journal of Production Agriculture 4(1), 57–61.

Cerutti-Maori, D., Sikaneta, I., Klare, J., Gierull, C. H., 2014. MIMO SAR processing for multichannel high-resolution wide-swath radars. IEEE Transactions on Geoscience and Remote Sensing 52(8), 5034–5055.

Chao, Z., Liu, N., Zhang, P., Ying, T., Song, K., 2019. Estimation methods developing with remote sensing information for energy crop biomass: A comparative review. Biomass and Bioenergy 122, 414–425.

Chen, J., Chen, J., Liao, A., Cao, X., Chen, L., Chen, X., He, C., Han, G., Peng, S., Lu, M., Zhang, W., Tong, X., Mills, J., 2015. Global land cover mapping at 30 m resolution: A POK-based operational approach. ISPRS Journal of Photogrammetry and Remote Sensing 103, 7–27.

Chen, P.-Y., Fedosejevs, G., Tiscareno-Lopez, M., Arnold, J. G., 2006. Assessment of MODIS-EVI, MODIS-NDVI and VEGETATION-NDVI composite data using agricultural measurements: an example at corn fields in western Mexico. Environmental monitoring and assessment 119(1-3), 69–82.

Cloude, S., Pottier, E., 1997. An entropy based classification scheme for land applications of polarimetric SAR. IEEE Transactions on Geoscience and Remote Sensing 35, 68–78.

Cloude, S., 2010. Polarisation: applications in remote sensing. Oxford University Press, New York, USA.

Cloude, S. R., Pottier, E., 1996. A review of target decomposition theorems in radar polarimetry. IEEE Transactions on Geoscience and Remote Sensing 34, 498–518.

Congalton, R. G., Green, K., 2008. Assessing the accuracy of remotely sensed data: principles and practices. CRC press, Taylor & Francis, Boca Raton, Florida, USA.

Curlander, J., McDonough, R., 1991a. Synthetic Aperture Radar: Systems and Signal Processing. JohnWiley& Sons, New York, USA.

Davis, F., Tarpley, J., 1983. Estimation of shelter temperatures from operational satellite sounder data. Journal of Climate and Applied Meteorology 22(3), 369–376.

Denize, J., Hubert-Moy, L., Betbeder, J., Corgne, S., Baudry, J., Pottier, E., 2019. Evaluation of using sentinel-1 and-2 time-series to identify winter land use in agricultural landscapes. Remote Sensing 11(1), 37.

Dobson, M. C., Ulaby, F. T., Pierce, L. E., 1995. Land-cover classification and estimation of terrain attributes using synthetic aperture radar. Remote Sensing of Environment 51(1), 199–214.

Drusch, M., Del Bello, U., Carlier, S., Colin, O., Fernandez, V., Gascon, F., Hoersch, B., Isola, C., Laberinti, P., Martimort, P., et al., 2012. Sentinel-2: ESA's optical high-resolution mission for GMES operational services. Remote Sensing of Environment 120, 25–36.

Duveiller, G., Defourny, P., 2010. A conceptual framework to define the spatial resolution requirements for agricultural monitoring using remote sensing. Remote Sensing of Environment 114(11), 2637–2650.

Emery, W., Camps, A., 2017. Introduction to Satellite Remote Sensing: Atmosphere, Ocean, Land and Cryosphere Applications. Elsevier, Amsterdam, Netherlands.

Erten, E., Lopez-Sanchez, J. M., Yuzugullu, O., Hajnsek, I., 2016. Retrieval of agricultural crop height from space: A comparison of SAR techniques. Remote Sensing of Environment 187, 130–144.

Esch, T., Marconcini, M., Felbier, A., Roth, A., Heldens, W., Huber, M., Schwinger, M., Taubenböck, H., Müller, A., Dech, S., 2013. Urban footprint processor—Fully automated processing chain generating settlement masks from global data of

the TanDEM-X mission. IEEE Geoscience and Remote Sensing Letters 10(6), 1617–1621.

FAO, IFAD, UNICEF, WHO, 2017. The State of Food Security and Nutrition in the World 2017: Building Resilience for Peace and Food Security. FAO, Rome, Italy.

Fisher, P., Comber, A. J., Wadsworth, R., 2005. Land use and land cover: contradiction or complement. In: Fisher, P., Unwin, D. (Eds.), Re-presenting GIS. John Wiley & Son., 85–98.

Foerster, S., Kaden, K., Foerster, M., Itzerott, S., 2012. Crop type mapping using spectral-temporal profiles and phenological information. Computers and Electronics in Agriculture 89, 30–40.

Foody, G., McCulloch, M., Yates, W., 1994. Crop classification from c-band polarimetric radar data. International Journal of Remote Sensing 15, 2871.

Forkuor, G., Conrad, C., Thiel, M., Ullmann, T., Zoungrana, E., 2014. Integration of optical and Synthetic Aperture Radar Imagery for Improving Crop Mapping in Northwestern Benin, West Africa. Remote Sensing 6(7), 6472–6499.

Fritz, S., See, L., Bayas, J. C. L., Waldner, F., Jacques, D., Becker-Reshef, I., Whitcraft, A., Baruth, B., Bonifacio, R., Crutchfield, J., et al., 2018. A comparison of global agricultural monitoring systems and current gaps. Agricultural Systems.

Fritz, T., Rossi, C., Yague-Martinez, N., Rodriguez-Gonzalez, F., Lachaise, M., Breit, H., 2011. Interferometric processing of TanDEM-X data. Geoscience and Remote Sensing Symposium (IGARSS), 2011 IEEE International, IEEE, 2428–2431.

Gantert, S., Kern, A., Düring, R., Janoth, J., Petersen, L., Herrmann, J., 2013. The future of X-band SAR: TerraSAR-X next generation and WorldSAR constellation. Synthetic Aperture Radar (APSAR), 2013 Asia-Pacific Conference on, IEEE, 20–23.

Gao, J., Liu, Y., 2011. Climate warming and land use change in Heilongjiang Province, Northeast China. Applied Geography 31(2), 476–482.

Garnett, T., Appleby, M. C., Balmford, A., Bateman, I. J., Benton, T. G., Bloomer, P., Burlingame, B., Dawkins, M.,

Dolan, L., Fraser, D., et al., 2013. Sustainable intensification in agriculture: premises and policies. Science 341(6141), 33–34.

Gebbers, R., Adamchuk, V. I., 2010. Precision agriculture and food security. Science 327(5967), 828–831.

Geologischer Dienst NRW, 2018. *Bodenkarte von Nordrhein-Westfalen 1 : 50 000*.

Godfray, H. C. J., Aveyard, P., Garnett, T., Hall, J. W., Key, T. J., Lorimer, J., Pierrehumbert, R. T., Scarborough, P., Springmann, M., Jebb, S. A., 2018. Meat consumption, health, and the environment. Science 361(6399), eaam5324.

Goense, D., 1997. The accuracy of farm machinery for precision agriculture: a case for fertilizer application. NJAS wageningen journal of life sciences 45(1), 199–215.

Gomez-Chova, L., Tuia, D., Moser, G., Camps-Valls, G., 2015. Multimodal Classification of Remote Sensing Images: A Review and Future Directions. Proceedings of the IEEE 103(9), 1560–1584.

Hagensieker, R., Waske, B., 2018. Evaluation of multi-frequency SAR images for tropical land cover mapping. Remote Sensing 10(2), 257.

Heipke, C., 2017. Photogrammetrie und Fernerkundung – eine Einführung. In: Freeden, W., Rummel, R. (Eds.), Photogrammetrie und Fernerkundung: Handbuch der Geodäsie. Springer.

Heupel, K., Spengler, D., Itzerott, S., 2018. A Progressive Crop-Type Classification Using Multitemporal Remote Sensing Data and Phenological Information. PFG–Journal of Photogrammetry, Remote Sensing and Geoinformation Science 86, 53–69.

Homolova, L., Malenovsky, Z., Clevers, J. G., Garcia-Santos, G., Schaepman, M. E., 2013. Review of optical-based remote sensing for plant trait mapping. Ecological Complexity 15, 1–16.

Houborg, R., Fisher, J. B., Skidmore, A. K., 2015. Advances in remote sensing of vegetation function and traits. International Journal of Applied Earth Observation and Geoinformation.

Idso, S. B., Jackson, R. D., Reginato, R. J., 1977. Remote-sensing of crop yields. Science 196(4285), 19–25.

Immitzer, M., Vuolo, F., Atzberger, C., 2016. First experience with Sentinel-2 data for crop and tree species classifications in central Europe. Remote Sensing 8(3, 166), 1–27.

IPCC, 2014. Climate change 2014: synthesis report. In: Contribution of Working Groups I, II and III to the fifth assessment report of the Intergovernmental Panel on Climate Change. Core Writing Team, Pachauri, P.K., and Meyers, L.A., Geneva, Switzerland.

Jensen, J. R., 2007. Remote sensing of the environment: An earth resource perspective. Pearson Prentice Hall, Upper Saddle River, New Jersey, USA.

Jensen, J. R., 2014. Remote sensing of the environment: An earth resource perspective 2/e. Pearson Education, Harlow, United Kingdom.

Jones, H. G., Vaughan, R. A., 2010. Remote sensing of vegetation: principles, techniques, and applications. Oxford university press, New York, USA.

Jones, J. W., Antle, J. M., Basso, B., Boote, K. J., Conant, R. T., Foster, I., Godfray, H. C. J., Herrero, M., Howitt, R. E., Janssen, S., et al., 2017. Toward a new generation of agricultural system data, models, and knowledge products: State of agricultural systems science. Agricultural systems 155, 269–288.

Jutzi, B., Meyer, F. J., Hinz, S., 2017. Aktive Fernerkundungssensorik – Technologische Grundlagen und Abbildungsgeometrie. In: Freeden, W., Rummel, R. (Eds.), Photogrammetrie und Fernerkundung: Handbuch der Geodäsie. Springer.

Kersebaum, K., 2011. Special features of the HERMES model and additional procedures for parameterization, calibration, validation, and applications. Methods of introducing system models into agricultural research, 65–94.

Koppe, W., Gnyp, M. L., Hütt, C., Yao, Y., Miao, Y., Chen, X., Bareth, G., 2013. Rice monitoring with multi-temporal and dual-polarimetric terrasar-X data. International Journal of Applied Earth Observation and Geoinformation 21(1), 568–576.

Kraus, T., Bachmann, M., Heiderich, L., Krieger, G., Moreira, A., 2017. Multistatic SAR imaging: Comparison of simulation results

and experimental data. International Conference on Radar Systems (Radar 2017), IET.

Krieger, G., Moreira, A., Fiedler, H., Hajnsek, I., Werner, M., Younis, M., Zink, M., 2007. TanDEM-X: A satellite formation for high-resolution SAR interferometry. Geoscience and Remote Sensing, IEEE Transactions on 45(11), 3317–3341.

Lambin, E. F., Meyfroidt, P., 2011. Global land use change, economic globalization, and the looming land scarcity. Proceedings of the National Academy of Sciences 108(9), 3465–3472.

Launay, M., Guerif, M., 2005. Assimilating remote sensing data into a crop model to improve predictive performance for spatial applications. Agriculture, ecosystems & environment 111(1-4), 321–339.

Lee, J.-S., Pottier, E., 2009. Polarimetric Radar Imaging From Basics To Applications. CRC press, Taylor &Francis, Boca Raton, Florida, USA.

Leroy, M., Roujean, J.-L., 1994. Sun and view angle corrections on reflectances derived from NOAA/AVHRR data. IEEE Transactions on Geoscience and Remote Sensing 32(3), 684–697.

Liang, S., 2005. Quantitative remote sensing of land surfaces. Vol. 30. John Wiley & Sons.

Liang, S., Li, X., Wang, J., 2012. Advanced remote sensing: terrestrial information extraction and applications. Academic Press, London, United Kingdom.

Lillesand, T., Kiefer, R., Chipman, J., 2004. Remote Sensing and Image interpretation. John Wiley & Sons, Inc., New Jersey, USA.

López-Dekker, P., Rot, H., Solberg, S., Zonno, M., Rodriguez-Cassola, M., Prats-Iraola, P., Moreira, A., 2017. Companion SAR constellations for single-pass interferometric applications: The SESAME mission. 2017 IEEE International Geoscience and Remote Sensing Symposium (IGARSS), IEEE, 119–122.

Löw, F., Duveiller, G., 2014. Defining the spatial resolution requirements for crop identification using optical remote sensing. Remote Sensing 6(9), 9034–9063.

Lu, D., Weng, Q., 2007. A survey of image classification methods and techniques for improving classification performance. International Journal of Remote Sensing 28, 823.

Lussem, U., Hütt, C., Waldhoff, G., 2016. Combined analysis of Sentinel-1 and RapidEye data for improved crop type classification: An early season approach for rapeseed and cereals. International Archives of the Photogrammetry, Remote Sensing and Spatial Information Sciences - ISPRS Archives 41, 959.

Machwitz, M., Hass, E., Junk, J., Udelhoven, T., Schlerf, M., 2018. CropGIS–A web application for the spatial and temporal visualization of past, present and future crop biomass development. Computers and Electronics in Agriculture.

Mahlein, A.-K., Oerke, E.-C., Steiner, U., Dehne, H.-W., 2012. Recent advances in sensing plant diseases for precision crop protection. European Journal of Plant Pathology 133(1), 197–209.

Mahmoud, A., Elbialy, S., Pradhan, B., Buchroithner, M., 2011. Field-based landcover classification using TerraSAR-X texture analysis. Advances in space research 48(5), 799–805.

Massonnet, D., Rossi, M., Carmona, C., Adragna, F., Peltzer, G., Feigl, K., Rabaute, T., 1993. The displacement field of the Landers earthquake mapped by radar interferometry. Nature 364(6433), 138.

McCarthy, U., Uysal, I., Melis, R. B., Mercier, S., Donnell, C. O., Kteniou daki, A., 2018. Global food security–Issues, challenges and technological solutions. Trends in Food Science & Technology.

McNairn, H., Kross, A., Lapen, D., Caves, R., Shang, J., 2014. Early season monitoring of corn and soybeans with TerraSAR-X and RADARSAT-2. International Journal of Applied Earth Observation and Geoinformation 28, 252–259.

McNairn, H., Champagne, C., Shang, J., Holmstrom, D., Reichert, G., 2009. Integration of optical and Synthetic Aperture Radar (SAR) imagery for delivering operational annual crop inventories. ISPRS Journal of Photogrammetry and Remote Sensing 64, 434–449.

McNairn, H., Shang, J., 2016. A review of multitemporal synthetic aperture radar (SAR) for crop monitoring. In: Ban, Y. (Ed.), Multitemporal Remote Sensing. Springer, 317–340.

Mo, T., Choudhury, B., Schmugge, T., Wang, J., Jackson, T., 1982. A model for microwave emission from vegetation-covered fields. Journal of Geophysical Research: Oceans 87(C13), 11229–11237.

Moran, M. S., Alonso, L., Moreno, J. F., Cendrero Mateo, M. P., Cruz, D. F. de la, Montoro, A., Pilar, M., Mateo, C., Cruz, D. F. D., Moran, S. M., Alonso, L., Moreno, J. F., Cendrero Mateo, M. P., Fernando De La Cruz, D., Montoro, A., Moran, M. S., Alonso, L., 2012. A RADARSAT-2 quad-polarized time series for monitoring crop and soil conditions in Barrax, Spain. IEEE Transactions on Geoscience and Remote Sensing 50(4), 1057–1070.

Moreira, A., Prats-Iraola, P., Younis, M., Krieger, G., Hajnsek, I., Papathanassiou, K. P., 2013. A tutorial on synthetic aperture radar. IEEE Geoscience and remote sensing magazine 1(1), 6–43.

Mulla, D. J., 2013. Twenty five years of remote sensing in precision agriculture: Key advances and remaining knowledge gaps. Biosystems engineering 114(4), 358–371.

National Oceanic and Atmospheric Administration (NOAA), 2018. National Centers for Environmental Information: Climate Data Online. https://www.ncdc.noaa.gov/cdo-web/, 2018-9-10.

Njoku, E., 2013. Encyclopedia of Remote Sensing. Springer, New York, USA.

Ottinger, M., Clauss, K., Kuenzer, C., 2017. Large-scale assessment of coastal aquaculture ponds with sentinel-1 time series data. Remote Sensing 9(5), 440.

Ozdogan, M., Yang, Y., Allez, G., Cervantes, C., 2010. Remote sensing of irrigated agriculture: Opportunities and challenges. Remote sensing 2(9), 2274–2304.

Pal, M., 2005. Random forest classifier for remote sensing classification. International Journal of Remote Sensing 26(1), 217–222.

Pal, M., Mather, P., 2005. Support vector machines for classification in remote sensing. International Journal of Remote Sensing 26(5), 1007–1011.

Parr, J., Papendick, R., Hornick, S., Meyer, R., 1992. Soil quality: attributes and relationship to alternative and sustainable agriculture. American Journal of Alternative Agriculture 7(1-2), 5–11.

Phalan, B., Onial, M., Balmford, A., Green, R. E., 2011. Reconciling food production and biodiversity conservation: land sharing and land sparing compared. Science 333(6047), 1289–1291.

Pinter Jr, P. J., Hatfield, J. L., Schepers, J. S., Barnes, E. M., Moran, M. S., Daughtry, C. S., Upchurch, D. R., 2003. Remote sensing for crop management. Photogrammetric Engineering & Remote Sensing 69(6), 647–664.

Pocock, D., 1983. Geographical fieldwork: an experiential perspective. Geography, 319–325.

Prestele, R., Alexander, P., Rounsevell, M. D., Arneth, A., Calvin, K., Doelman, J., Eitelberg, D. A., Engström, K., Fujimori, S., Hasegawa, T., et al., 2016. Hotspots of uncertainty in land-use and land-cover change projections: a global-scale model comparison. Global change biology 22(12), 3967–3983.

Qi, Z., Yeh, A. G.-O., Li, X., Lin, Z., 2012. A novel algorithm for land use and land cover classification using RADARSAT-2 polarimetric SAR data. Remote Sensing of Environment 118, 21–39.

Reichenau, T., Korres, W., Montzka, C., Fiener, P., Wilken, F., Stadler, A., Schneider, K., 2016. Spatial heterogeneity of leaf area index (LAI) and its temporal course on arable land: combining field measurements, remote sensing and simulation in a comprehensive data analysis approach (CDAA). Plos One 11, 1–24.

Reinartz, P., Müller, R., Schwind, P., Suri, S., Bamler, R., 2011. Orthorectification of VHR optical satellite data exploiting the geometric accuracy of TerraSAR-X data. ISPRS Journal of Photogrammetry and Remote Sensing 66(1), 124–132.

Ribbert, K., 2010. Geologie im Rheinischen Schiefergerbirge - Teil 1 Nordeifel. Geologie im Rheinischen Schiefergerbirge1. Geologischer Dienst Nordrhein-Westfahlen, Krefeld, Germany.

Richards, J. A., 2009. Remote Sensing with Imaging Radar. Springer, Heidelberg, Germany.

Rockström, J., Williams, J., Daily, G., Noble, A., Matthews, N., Gordon, L., Wetterstrand, H., DeClerck, F., Shah, M., Steduto, P., et al., 2017. Sustainable intensification of agriculture for human prosperity and global sustainability. Ambio 46(1), 4–17.

Rodriguez-Galiano, V. F., Ghimire, B., Rogan, J., Chica-Olmo, M., Rigol-Sanchez, J. P., 2012. An assessment of the effectiveness of a random forest classifier for land-cover classification. ISPRS Journal of Photogrammetry and Remote Sensing 67, 93–104.

Rodriguez, E., Morris, C., Belz, J., 2006. A global assessment of the SRTM performance. Photogrammetric Engineering & Remote Sensing 72, 249–260.

Rosen, P. A., Hensley, S., Shaffer, S., Veilleux, L., Chakraborty, M., Misra, T., Bhan, R., Sagi, V. R., Satish, R., 2015. The nasa-isro sar mission-an international space partnership for science and societal benefit. Radar Conference (RadarCon), 2015 IEEE, IEEE, 1610–1613.

Rost, S., Gerten, D., Bondeau, A., Lucht, W., Rohwer, J., Schaphoff, S., 2008. Agricultural green and blue water consumption and its influence on the global water system. Water Resources Research 44(9).

Roy, D. P., Wulder, M., Loveland, T. R., Woodcock, C., Allen, R., Anderson, M., Helder, D., Irons, J., Johnson, D., Kennedy, R., et al., 2014. Landsat-8: Science and product vision for terrestrial global change research. Remote sensing of Environment 145, 154–172.

Santoro, M., Wegmüller, U., Askne, J. I., 2010. Signatures of ERS–Envisat interferometric SAR coherence and phase of short vegetation: an analysis in the case of maize fields. Geoscience and Remote Sensing, IEEE Transactions on 48(4), 1702–1713.

Schmullius, C., Thiel, C., Pathe, C., Santoro, M., 2015. Radar time series for land cover and forest mapping. In: Kuenzer, C., Dech, S., Wagner, W. (Eds.), Remote Sensing Time Series. Springer, New York, USA, 323–356.

Schubert, A., Small, D., Miranda, N., Geudtner, D., Meier, E., 2015. Sentinel-1A product geolocation accuracy: commissioning phase results. Remote sensing 7(7), 9431–9449.

See, L., Fritz, S., You, L., Ramankutty, N., Herrero, M., Justice, C., Becker-Reshef, I., Thornton, P., Erb, K., Gong, P., et al., 2015. Improved global cropland data as an essential ingredient for food security. Global Food Security 4, 37–45.

Skriver, H., 2012. Crop classification by multitemporal C- and L-band single- and dual-polarization and fully polarimetric SAR. IEEE Transactions on Geoscience and Remote Sensing 50, 2138.

Skriver, H., Svendsen, M., Thomsen, A., 1999. Multitemporal C- and L-band polarimetric signatures of crops. IEEE Transactions on Geoscience and Remote Sensing 37, 2413.

Solberg, A. H. S., Jain, A. K., Taxt, T., 1994. Multisource classification of remotely sensed data: fusion of Landsat TM and SAR images. Geoscience and Remote Sensing, IEEE Transactions on 32(4), 768–778.

Song, K., Wang, Z., Du, J., Liu, L., Zeng, L., Ren, C., 2014. Wetland degradation: its driving forces and environmental impacts in the Sanjiang Plain, China. Environmental management 54(2), 255–271.

Spielmann, H., 1989. Agrargeographie in Stichworten. Hirt, Kiel, Germany.

Staiger, B., Schütte, H.-W., Emmerich, R., 2003. Das grosse China-Lexikon: Geschichte, Geographie, Gesellschaft, Politik, Wirtschaft, Bildung, Wissenschaft, Kultur: eine Veröffentlichung des Instituts für Asienkunde Hamburg. Primus, Darmstadt, Germany.

Sun, Z., Wang, D., Zhong, G., 2018. A Review of Crop Classification Using Satellite-Based Polarimetric SAR Imagery. 2018 7th International Conference on Agro-geoinformatics (Agro-geoinformatics), IEEE, 1–5.

Thenkabail, P. S., Smith, R. B., De Pauw, E., 2000. Hyperspectral vegetation indices and their relationships with agricultural crop characteristics. Remote sensing of Environment 71(2), 158–182.

Thompson, A. A., 2015. Overview of the RADARSAT constellation mission. Canadian Journal of Remote Sensing 41(5), 401–407.

Tilly, N., Hoffmeister, D., Schiedung, H., Hütt, C., Brands, J., Bareth, G., 2014. Terrestrial laser scanning for plant height measurement and biomass estimation of maize. The International Archives of Photogrammetry, Remote Sensing and Spatial Information Sciences 40(7), 181–187.

Tilly, N., Aasen, H., Bareth, G., 2015. Fusion of plant height and vegetation indices for the estimation of barley biomass. Remote Sensing 7(9), 11449–11480.

Tilly, N., Hoffmeister, D., Cao, Q., Huang, S., Lenz-Wiedemann, V., Miao, Y., Bareth, G., 2014. Multitemporal crop surface models: accurate plant height measurement and biomass estimation with terrestrial laser scanning in paddy rice. Journal of Applied Remote Sensing 8(1), 083671.

Tilman, D., Cassman, K. G., Matson, P. A., Naylor, R., Polasky, S., 2002. Agricultural sustainability and intensive production practices. Nature 418(6898), 671.

Torres, R., Snoeij, P., Geudtner, D., Bibby, D., Davidson, M., Attema, E., Potin, P., Rommen, B., Floury, N., Brown, M., et al., 2012. GMES Sentinel-1 mission. Remote Sensing of Environment 120, 9–24.

Turner, B. L., Lambin, E. F., Reenberg, A., 2007. The emergence of land change science for global environmental change and sustainability. Proceedings of the National Academy of Sciences 104(52), 20666–20671.

Ulaby, F. T., Dubois, P. C., Van Zyl, J., 1996. Radar mapping of surface soil moisture. Journal of hydrology 184(1-2), 57–84.

Ulaby, F. T., Long, D. G., 2014. Microwave Radar and Radiometric Sensing. The University of Michigan Press, Ann Arbor, USA.

Updike, T., Comp, C., 2010. Radiometric use of WorldView-2 imagery. Technical Note, 1–17.

Van Niel, T. G., McVicar, T. R., 2004b. Determining temporal windows for crop discrimination with remote sensing: a case study in south-eastern Australia. Computers and Electronics in Agriculture 45(1-3), 91–108.

Verhoef, W., 1998. Theory of radiative transfer models applied in optical remote sensing of vegetation canopies.

Vinciková, H., Hais, M., Brom, J., Procházka, J., Pecharová, E., 2010. Landscape studies use of remote sensing methods in studying agricultural landscapes – A review. Journal of Landscape Studies 3, 53.

Vitousek, P. M., Aber, J. D., Howarth, R. W., Likens, G. E., Matson, P. A., Schindler, D. W., Schlesinger, W. H., Tilman, D. G., 1997. Human alteration of the global nitrogen cycle: sources and consequences. Ecological applications 7(3), 737–750.

Von Thünen, J. H., 1875. Der isolierte Staat in Beziehung auf Landwirtschaft und Nationalökonomie. Wiegant, Hempel & Parey, Rostock, Germany.

Waldhoff, G., Curdt, C., Hoffmeister, D., Bareth, G., 2012. Analysis of multitemporal and multisensor remote sensing data for crop rotation mapping. ISPRS International Archives of the Photogrammetry, Remote Sensing and Spatial Information Sciences, I-7, 177–182.

Waldhoff, G., Eichfuss, S., Bareth, G., 2015. Integration of remote sensing data and basic geodata at different scale levels for improved land use analyses. The International Archives of Photogrammetry, Remote Sensing and Spatial Information Sciences 40(3), 85.

Waldhoff, G., Lussem, U., Bareth, G., 2017. Multi-Data Approach for remote sensing-based regional crop rotation mapping: A case study for the Rur catchment, Germany. International Journal of Applied Earth Observation and Geoinformation 61, 55–69.

Wang, Z., Zhang, B., Zhang, S., Li, X., Liu, D., Song, K., Li, J., Li, F., Duan, H., 2006. Changes of land use and of ecosystem service values in Sanjiang Plain, Northeast China. Environmental Monitoring and Assessment 112(1-3), 69–91.

Whelan, B., Taylor, J., 2013. Precision agriculture for grain production systems. Csiro publishing, Collingwood, Australia.

Whitcraft, A., Vermote, E., Becker-Reshef, I., Justice, C., 2015. Cloud cover throughout the agricultural growing season: Impacts on passive optical earth observations. Remote Sensing of Environment 156, 438–447.

Wiebe, K., Lotze-Campen, H., Sands, R., Tabeau, A., Mensbrugghe, D. van der, Biewald, A., Bodirsky, B., Islam, S., Kavallari, A., Mason-D'Croz, D., et al., 2015. Climate change impacts on agriculture in 2050 under a range of plausible socioeconomic and emissions scenarios. Environmental Research Letters 10(8), 085010.

Woodhouse, I., 2015. Introduction to Microwave Remote Sensing. Speckled Press, Linlithgow, United Kingdom.

Wu, B., Meng, J., Li, Q., Yan, N., Du, X., Zhang, M., 2014. Remote sensing-based global crop monitoring: experiences with China's CropWatch system. International Journal of Digital Earth 7(2), 113–137.

Xaypraseuth, P., Satish, R., Chatterjee, A., 2015. NISAR spacecraft concept overview: Design challenges for a proposed flagship dual-frequency SAR mission. 2015 IEEE Aerospace Conference, IEEE, 1–11.

Xie, Y., Sha, Z., Yu, M., 2008. Remote sensing imagery in vegetation mapping: a review. Journal of plant ecology 1(1), 9–23.

Xiong, J., Thenkabail, P. S., Gumma, M. K., Teluguntla, P., Poehnelt, J., Congalton, R. G., Yadav, K., Thau, D., 2017. Automated cropland mapping of continental Africa using Google Earth Engine cloud computing. ISPRS Journal of Photogrammetry and Remote Sensing 126, 225–244.

Xiubin, L., 1996. A review of the international researches on land use/land cover change [J]. Acta Geographica Sinica 6.

Yang, H., Yang, G., Gaulton, R., Zhao, C., Li, Z., Taylor, J., Wicks, D., Minchella, A., Chen, E., Yang, X., 2018. In-season biomass estimation of oilseed rape (Brassica napus L.) using fully polarimetric SAR imagery. Precision Agriculture, 1–19.

Younis, M., Fischer, C., Wiesbeck, W., 2003. Digital beamforming in SAR systems. IEEE Transactions on Geoscience and Remote Sensing 41(7), 1735–1739.

Zecha, C., Link, J., Claupein, W., 2013. Mobile sensor platforms: Categorisation and research applications in precision farming. J. Sens. Sens. Syst 2, 51–72.

Zhang, H., Malczewski, J., 2017. Quality Evaluation of Volunteered Geographic Information: The Case of OpenStreetMap. In: Volunteered Geographic Information and the Future of Geospatial Data. IGI Global, Hershey, PA, USA, 19–46.

Zhang, J., 2010. Multi-source remote sensing data fusion: status and trends. International Journal of Image and Data Fusion 1(1), 5–24.

Zhang, N., Wang, M., Wang, N., 2002. Precision agriculture—a worldwide overview. Computers and electronics in agriculture 36(2-3), 113–132.

Zhao, S., 1986. Physical Geography of China. John Wiley & Sons, Science Press, Beijing, China and New York, USA.

Zimmerman, R., Doan, D., Leung, L., Mason, J., Parsons, N., Shahid, K., 2017. Commissioning the world's largest satellite constellation. Conference on Small Satellites.

Zink, M., Bachmann, M., Brautigam, B., Fritz, T., Hajnsek, I., Moreira, A., Wessel, B., Krieger, G., 2014. TanDEM-X: the new global DEM takes shape. IEEE Geoscience and Remote Sensing Magazine 2(2), 8–23.

A Appendix

Anhang A.1 Eigenanteile

In diesem Kapitel wird der Eigenanteil an den in dieser Arbeit enthaltenen Publikationen dargelegt.

A.1.1 Eigenanteil Kapitel 3

Titel	**Best Accuracy Land Use/Land Cover (lulc) Classification to Derive Crop Types Using Multitemporal, Multisensor, and Multi-Polarization SAR Satellite Images**
Autoren	Hütt, Christoph; Koppe, Wolfgang, Miao, Yuxin; Bareth, Georg
Status	Veröffentlicht
Journal	Remote Sensing
Verlag	Multidisciplinary Digital Publishing Institute (MDPI)
Publikationsjahr	2016
Ausgabe	Band 8
Artikelnummer	684
DOI	http://dx.doi.org/10.3390/rs8080684
Eigenanteil	Aufnahme der Felddaten in China (April-Oktober 2009) Beschaffung der Fernerkundungsdaten aus unterschiedlichen Quellen Analyse der Daten Verfassen des Manuscripts Management des Peer Review Prozesses

A.1.2 Eigenanteil Kapitel 4

Titel	**Georeferencing Multi-source Geospatial Data Using Multi-temporal TerraSAR-X Imagery: a Case Study in Qixing Farm, Northeast China**
Autoren	Zhao, Quanying; Hütt, Christoph; Lenz-Wiedemann, Victoria I. S.; Miao, Yuxin; Yuan, Fei; Zhang, Fusuo; Bareth, Georg
Status	Veröffentlicht
Journal	Journal for Photogrammetry, Remote Sensing and Geoinformation Science. (PFG)
Verlag	Schweizbart Science Publishers
Publikationsjahr	2015
Ausgabe	Heft 2
Seiten	173–185
DOI	http://dx.doi.org/10.3390/rs8080684
Eigenanteil	Entwicklung der Konzeptidee: Nutzung der Lagegenauigkeit von TerraSAR-X als geographische Referenz Akquirierung und Prozessierung der TerraSAR-X Daten Beschreibung der Methodik der Prozessierung der TerraSAR-X Daten Korrekturlesen und Review des Manuskripts

Diese Publikation stellt maßgeblich die wissenschaftliche Arbeit von Frau Quanying Zhao dar. Der Eigenanteil an dieser Publikation ist oben im Detail aufgeführt.

A.1.3 Eigenanteil Kapitel 5

Titel	**Multi-data Approach for Crop Classification Using Multitemporal, Dual-Polarimetric TerraSAR-X Data, and Official Geodata**
Autoren	Hütt, Christoph; Waldhoff, Guido
Status	Veröffentlicht
Journal	European Journal of Remote Sensing
Verlag	Taylor & Francis
Publikations-jahr	2018
Ausgabe	Band 51, Heft 1
Seiten	62 – 74
DOI	https://doi.org/10.1080/22797254.2017.1401909
Eigenanteil	Beschaffung der Fernerkundungsdaten
	Analysen der Daten
	Verfassen des Manuscripts
	Management des Peer Review Prozesses

A.1.4 Eigenanteil Kapitel 6

Titel	**An Open Data and Open Source Approach for Crop Type Mapping with Sentinel-1 SAR Satellite Images, Geodata from Open.NRW, and FOSS**
Autoren	Hütt, Christoph; Waldhoff, Guido; Bareth, Georg
Status	Manuskript so wie eingereicht
Journal	Journal for Photogrammetry, Remote Sensing and Geoinformation Science. (PFG)
Verlag	Springer
Publikations-jahr	Im Review
Eigenanteil	Beschaffung der Fernerkundungsdaten Analysen der Daten Verfassen des Manuscripts

A.1.5 Eigenanteil Kapitel 7

Titel	**Fusion of High Resolution Remote Sensing Images and Terrestrial Laser Scanning for Improved Biomass Estimation of Maize**
Autoren	Hütt, Christoph; Tilly, Nora; Schiedung, Henning; Bareth, Georg
Status	Veröffentlicht
Journal	The International Archives of the Photogrammetry, Remote Sensing and Spatial Information Sciences (ISPRS Archives)
Verlag	International Society of Photogrammetry and Remote Sensing (ISPRS)
Publikations-jahr	2014
Ausgabe	Band XL-7
Seiten	101–108
DOI	https://doi.org/10.5194/isprsarchives-XL-7-101-2014
Eigenanteil	Aufnahme der Daten Analysen der Daten Verfassen des Manuscripts

A.1.6 Eigenanteil Kapitel 8

Titel	**Potential of Multitemporal TanDEM-X Derived Crop Surface Models for Maize Growth Monitoring**
Autoren	Hütt, Christoph; Tilly, Nora; Schiedung, Henning; Bareth, Georg
Status	Veröffentlicht
Journal	The International Archives of the Photogrammetry, Remote Sensing and Spatial Information Sciences (ISPRS Archives)
Verlag	International Society of Photogrammetry and Remote Sensing (ISPRS)
Publikations-jahr	2016
Ausgabe	Band XLI-B7
Seiten	803–808
DOI	https://doi.org/10.5194/isprs-archives-XLI-B7-803-2016
Eigenanteil	Aufnahme der Daten Analysen der Daten Verfassen des Manuscripts

Anhang 2 Erklärung

Ich versichere, dass ich die von mir vorgelegte Dissertation selbständig angefertigt, die benutzten Quellen und Hilfsmittel vollständig angegeben und die Stellen der Arbeit – einschließlich Tabellen, Karten, und Abbildungen –, die anderen Werken im Wortlaut oder dem Sinn nach entnommen sind, in jedem Einzelfall als Entlehnung kenntlich gemacht habe; dass diese Dissertation noch keiner anderen Fakultät oder Universität zur Prüfung vorgelegen hat; dass sie – abgesehen von unten angegebenen Teilpublikationen – noch nicht veröffentlicht worden ist sowie, dass ich eine solche Veröffentlichung vor Abschluss des Promotionsverfahrens nicht vornehmen werde. Die Bestimmungen der Promotionsordnung sind mir bekannt. Die von mir vorgelegte Dissertation ist von Prof. Dr. Georg Bareth betreut worden.

Köln, den 13.06.2019

Christoph Hütt